RICE UNIVERSITY

Improving Small Scale Cooling of Mini-Channels using Added Surface Defects

by

Jami Frances Tullius

A THESIS SUBMITTED
IN PARTIAL FULFILLMENT OF THE
REQUIREMENTS FOR THE DEGREE

Doctor of Philosophy

APPROVED, THESIS COMMITTEE

Dr. Yildiz Bayazitoglu, Chair
Harry S. Cameron Chair Professor in
Mechanical Engineering

Dr. Enrique V. Barrera
Professor of Mechanical Engineering and
Materials Science

Dr. Richard A. Tapia
University Professor, Maxfield-Oshman Chair
in Engineering

HOUSTON, TEXAS
April 2013

ABSTRACT

Improving Small Scale Cooling of Mini-Channels using Added Surface Defects

by

Jami Frances Tullius

Advancements in electronic performance lead to a decrease in device size and an increase in power density. Because of these changes, current cooling mechanisms for electronic devices are beginning to be ineffective. Microchannels, with their large heat transfer surface area to volume ratio, cooled with either gas or liquid coolant, have shown some potential in adequately maintaining a safe surface temperature. By modifying the walls of the microchannel with fins, the cooling performance can be improved.

Using computational fluid dynamics software, microfins placed in a staggered array on the bottom surface of a rectangular minichannel are modeled in order to optimize microstructure geometry and maximize heat transfer dissipation through convection from a heated surface. Fin geometry, dimensions, spacing, height, and material are analyzed. Correlations describing the Nusselt number and the Darcy friction factor are obtained and compared to recent studies. These correlations only apply to short fins in the laminar regime. Triangular fins with larger fin height, smaller fin width, and spacing double the fin width maximizes the number of fins in each row and yields better thermal performance.

Once the effects of microfins were found, an experiment with multi-walled carbon nanotubes (MWNTs) grown on the surface were tested using both water and Al_2O_3/H_2O nanofluid as the working medium. Minichannel devices containing two different MWNT structures – one fully coated surface of MWNTs and the other with a circular staggered fin array of MWNTs - were tested and compared to a minichannel device with no MWNTs. It was observed that the sedimentation of Al_2O_3 nanoparticles on a channel surface with no MWNTs increases the surface roughness and the thermal performance.

Finally, using the lattice Boltzmann method, a two dimensional channel with suspended particles is modeled in order to get an accurate characterization of the fluid/particle motion in nanofluid. Using the analysis based on an ideal fin, approximate results for nanofluids with increase surface roughness was obtained.

Microchannels have proven to be effective cooling systems and understanding how to achieve the maximum performance is vital for the innovation of electronics. Implementation of these modified channel devices can allow for longer lasting electronic systems.

Acknowledgments

Foremost, I would like to express my sincere gratitude to my committee advisors Dr. Yildiz Bayazitoglu, Dr. Rick Barrera, and Dr. Richard Tapia for their guidance and support throughout my career at Rice University.

Further I would like to thank my advisor Dr. Yildiz Bayazitoglu for her guidance and support. I feel you have prepared me for whatever obstacles my future may hold. I am grateful for you bringing me into your group back in 2008. You have given me many opportunities including the wonderful trip and conference to Turkey. Thank you!

A special thanks to the Alliances for Graduate Education and the Professoriate (AGEP), my office mates, NASA and the Harriet G. Jenkins Pre-Doctoral Fellowship Program, the National GEM Consortium, and NSF for their continuous support throughout my graduate school career.

I want to thank my family, especially my loving sister Toni, for their unending encouragement and love. I could not have done this work without any of you.

Contents

List of Figures

List of Tables

Nomenclature

2DQ9	2 dimensional, 9 velocity
2H	Height of channel
a	Acceleration (Chapter 4)
a_f	Surface area of fin
a_o	Surface area of base
A	Area of particle
A_b	Surface area of the heated base region
A_c	Flow area of channel
A_f	Cross-sectional area of fin
a,b,c,e,r,s	Fin geometrical dimensions (Chapter 2)
C_{nu},C_f,S,U,V,W,X,Y,Z	Constants
c	Lattice velocity
C_B	Coefficient [-1,0,1]
C_D	Drag coefficient
CFD	Computational fluid dynamics
CHF	Critical heat flux
CNT	Carbon nanotubes
CVD	Chemical vapor deposition
c_p	Specific heat of constant pressure
$c_{p,Al2O3}$	Specific heat of constant pressure of nanofluid
$c_{p,H2O}$	Specific heat of constant pressure of nanofluid
$c_{p,nf}$	Specific heat of constant pressure of nanofluid
c_s	Lattice speed of sound

d_c	Depth of channel
dh	Clearance of channel $(h_c - h_f)$
d_h	Depth of heated surface
D	Dimension
D_c	Hydraulic diameter of channel $\left(4A_c/P_c\right)$
D_f	Hydraulic diameter of fin $\left(4A_f/P_f\right)$
DAQ	Data acquisition unit
DSMC	Direct simulation Monte Carlo
e	Direction lattice velocity
f	Darcy fiction factor (Chapter 2)
f	Density particle distribution function (Chapter 4)
f_{opp}	Opposite incident function for boundary condition
f^{eq}	Density equilibrium distribution function
F_B	Buoyancy force
F_{body}	Pressure driven body force
F_{Brown}	Brownian motion force
F_D	Drag force
F_g	Force of gravity
F_{Total}	Total force
g	Energy particle distribution function
g^{eq}	Energy equilibrium distribution function
grav	Gravity
h	Average heat transfer coefficient (Chapter 2)
h	Local heat transfer coefficient (Chapter 4)

$\overline{h}$	Average heat transfer coefficient
h_b	Average heat transfer coefficient of base
h_c	Height of channel
h_{fin}	Average heat transfer coefficient of fin
h_f	Height of fins
k	Thermal conductivity
k_B	Boltzmann constant
k_{Al2O3}	Thermal conductivity of alumina nanoparticles
k_{H2O}	Thermal conductivity of water
k_{nf}	Thermal conductivity of nanofluid
Kn	Knudsen number
lm	Lattice mass
ls	Lattice second
lu	Lattice unit
L	Length
LBM	Lattice Boltzmann method
m	Mass
M	Number of velocities using; M=5
Ma	Mach number
MAE	Mean absolute error
MD	Molecular dynamics
MWNT	Multi-walled carbon nanotube
N	Total number of fins
N_x	Number of fins along the x-axis
N_y	Number of fins along the y-axis (Chapter 2)

N_y	Number of nodes in the y-direction (Chapter 4)
NS	Navier-Stokes
Nu	Nusselt number
Nu_f	Nusselt number across the fins
P_c	Wetted perimeter of channel
P_f	Wetted perimeter of fin
p	Pressure
Δp	Pressure drop
Δp_c	Pressure drop due to contraction
Δp_{ch}	Pressure drop across the channel
Δp_e	Pressure drop due to expansion
Δp_m	Pressure drop across the manifolds
Δp_n	Pressure drop in norprene tubing
Pr	Prandtl number of fluid
Pr_s	Prandtl number of surface
Q	Applied heat
Q_{fin}	Heat transfer through fin
Q_{ideal}	Heat transfer through ideal fin
Q_{nofin}	Heat transfer when no fins
q	Applied heat flux
r	Radius
R	Ideal gas constant
Re	Reynolds number
Re_f	Reynolds number of the fin
Re_x	Reynolds number along the length of channel

S_f	Spacing of fins (Chapter 4)
S_L	Longitudal pitch (center to center)
S_t	Transverse pitch (center to center)
SWNT	Single-walled carbon nanotube
t	Time
Δt	Time step
Δt_{phys}	Time step in physical units
T	Temperature
T_C	Cold temperature
T_H	Hot temperature
T_{in}	Inlet temperature
T_{lu}	Temperature in lattice units
T_{nw}	Near wall temperature
T_{out}	Outlet temperature
T_w	Wall temperature
T_∞	Bulk temperature
ΔT	Temperature difference
u	Axial velocity (Chapter 1/2/3)
u	Macroscopic velocity (Chapter 4)
u_{lu}	Velocity in lattice units
u_{phys}	Velocity in physical units
u_{max}	Maximum axial velocity
u_x	Velocity in x-direction
u_y	Velocity in y-direction
Δu	Velocity difference between fluid and particle

V	Volume
$\dot{V}$	Volumetric flow rate
w	Weighing factor
w_c	Width of channel
w_f	Width of fins
Δx	Distance between thermocouples (Chapter 3)
Δx	Lattice distance in x-direction (Chapter 4)
Δx_{lu}	Lattice distance in x-direction in lattice units
Δx_{phys}	Lattice distance in x-direction in physical units
y	Point along the y-axis
y_{bottom}	Bottom most point along the y-axis
y_{top}	Top most point along the y-axis
Δy	Lattice distance in y-direction

Greek

ρ	Density
$\rho_{Al_2O_3}$	Density of alumina nanoparticles
ρ_{H_2O}	Density of water
ρ_{nf}	Density of nanofluid
ρ_f	Density of fluid
ρ_p	Density of particle
ρ_{ref}	Reference density
ρ_{lu}	Density in lattice units

ρ_{phys}	Density in physical units
σ_{lu}	Thermal diffusion in lattice units
μ	Dynamic viscosity
ν	Kinematic viscosity
ν_{lu}	Kinematic viscosity in lattice units
ν_{phys}	Kinematic viscosity in physical units
ε	Relative roughness
ε_f	Fin effectiveness
θ	Non-dimensional distribution
θ_o	Temperature distribution $\left(T_w - T_\infty\right)$
η	Fin efficiency
ϕ	Volume concentration
τ	Density relaxation time
τ_T	Energy relaxation time
δ_t	Thermal boundary layer thickness

Chapter 1

A Review of Cooling in Microchannels

With electronics innovating quickly into smaller more reliable devices, there is a need for improved heat removal at small scales. Electronics must sustain a low constant surface temperature in order to avoid overheating. The advancements in the electrical devices are limited by the absence of efficient methods to remove the heat that is generated. A method of appropriate cooling is necessary to allow for more advancement in the years to come while maintaining proper functioning. This work reviews the effective cooling methods of small scale channels.

Many techniques have been studied such as the use of thermal interface materials, heat spreaders and heat sinks, or micro- and minichannels. Mini- and microchannels have proven to be effective in cooling small surfaces of electrical components such as microchips. These channels act as heat exchangers or heat sinks. The high temperatures can be dissipated through the modified surfaces of the microchannel with natural or forced convection of the fluid within the channel [1–

5]. These channels contain a much higher heat transfer surface area to fluid volume ratio, which allows the convection to be enhanced when compared to macro-scale systems. As the hydraulic diameter decreases in a microchannel, the heat transfer coefficient increases, providing an excellent cooling mechanism; however, these small channels experience a very high pressure drop. A basic microchannel with a smooth wall surface has demonstrated to cool a heat flux of approximately 790 W/cm^2 at a temperature of 71°C while the pressure drop was roughly 214 kPa [6,7].

Because of the rapidly developing electronic technologies, improvements to this cooling apparatuses are necessary. Optimal surface impairments and fluids are necessary to achieve maximum cooling from microchannels. My work focuses on understanding how different surface impairments can influence the microchannel in order to obtain maximum thermal performance and maintain a relatively low pressure drop.

This chapter will review the effects of a microchannel with various surface impairments including increased surface roughness, grooves, and micro pin fins, and the use of different fluids flowing through the channel in the single phase laminar flow. Also the mathematical methods needed to calculate micro- and nano-scale flow characteristics through a microchannel are reviewed.

1.1. Single Phase Fluid

Microchannel cooling can be influenced by many factors, including the surface roughness of the channel walls, the cavities machined on the channel

surface, and the addition of micro pin fins. This section will review the work of others that have applied surface structures to their microchannel walls. Understanding the effects of these surface impairments can help achieve an optimal microchannel for maximum cooling.

1.1.1. Increased Surface Roughness

Surface roughness is a major factor in optimizing the thermal performance. Microchannels can have smooth surface walls or can contain small structures meant to disturb the fluid as it flows. Shokouhmand [8] studied the surface roughness effects of a fully developed, laminar, rough rectangular microchannel analytically using the Gaussian technique. The aspect ratio was varied from 0 to 1 and the relative roughness from 0 to 0.15. For roughness values less than 0.01, there was little effect on the friction factor; however, for roughness values between 0.01 and 1 with an aspect ratio of 1, there was an increase of 11.3%, with an aspect ratio 0.5 there was a 5.5% increase of the friction factor and for an aspect ratio of 0.1 there was a 1.7% increase. For the convective heat transfer coefficient, there is a parabolic profile with the values of the lower aspect ratio close to 0 and the higher aspect ratio near 1 being high and the values with the aspect ratio of 0.5 reaching a minimum. Decreasing the relative roughness of the channel also decreases the heat transfer coefficient slightly. For a relative roughness of 0.01, the aspect ratio has little effect. As the relative roughness value increases, so does the friction factor, while the Nu is not dependent on the roughness scale. With an increase in surface roughness the convection heat transfer coefficient will increase slightly [8].

Increased surface roughness can lead to increased wettability of the surface, which can play a critical role in improving the heat transfer performance. The wettability of the surface is determined by the contact angle that the fluid makes with the surface. A contact angle less than 90° indicates the fluid will spread over a large area of the surface translating to removing large amounts of heat. This is known as a hydrophilic surface. A contact angle greater than 90° lessens the contact of the fluid to the surface, also known as a hydrophobic surface. Minimum wettability contact angle will maximize cooling. To achieve a high heat transfer coefficient, the optimal surface is one with low wettability contact angle containing many nucleation sites [9]. Increased surface deficiencies can lead to and increased wettability.

1.1.2. Grooved Surfaces

A method used to impact the cooling performance is applying small grooves to the surface. Lee [7], Solovitz [10], and Baghernezhad [11] all adjusted the wall surface of a microchannel with grooves. These openings can induce more disturbances in the flow providing a more effective cooling mechanism. When dimples were applied to the surface, the pressure drop was maintained- that is, it did not increase from a smooth microchannel- and the heat transfer performance was increased by roughly 12%. The spacing and the size of the grooves are still being tested to obtain the maximum efficiency of the channel [7]. Solovitz [10] modeled a 2D simulation with a small dimple-like groove imbedded in the channel surface. When varying the dimensions of the cavity and the Reynolds number (Re),

there was a 70% increase in the heat transfer performance with only a 30% increase in pressure drop when compared to a smooth base model using a depth/diameter ratio of 0.4 and a Re of 1000. The depth of the cavity was proportional to the cooling performance of the channel. Baghernezhad [11] compared the shapes of the grooves used to disrupt the flow. A rectangular and an arc shape groove were compared and they found that both shapes can improve the cooling performance but that the arc shaped is more effective. This is probably due to the aerodynamics of the flow past the gap. From these studies, grooves can increase performance while maintaining pressure drop. Grooved surfaces in minichannels provide adequate cooling devices; however, the integrity of the channel is threatened. Therefore, the addition of surface extrusions will be introduced.

1.1.3. Micro Pin Fins

Micro pin fins, micro-studs, pillars, and square pin fins are all synthetically engineered structures, usually made of silicon but which can be made of other thermally conducting material, which have shown significant improvements in removing heat. These structures protrude out of the surface, increase the wall surface area, and interrupt the steady flow of the fluid. They can take different shapes and sizes and be placed in different patterns to improve the thermal heat transfer performance. Vanapalli [12] investigated the pillar “fin” shape which contains the lowest friction factor with nitrogen gas flowing through the microchannel. These pillars are used to increase the contact between the surface

and the fluid with minimal thermal resistance. The geometries tested were circles, squares, rhombus, elliptical, eye shaped, and sine shape cross-sections in staggered arrangements across the surface. Pillars with the sine shape cross-sections, when compared to all of the other geometries, have the lowest friction factor. A 3D representation of shapes Vanapalli [12] used is shown in Figure 1.1. Shape of the fins can affect the motion of flow. When the pillars are aerodynamic in shape, there is less separation of the fluid from the solid body creating less thermal resistance at the interface.

Lee [13] implemented oblique fins into a microchannel to understand the effects of the local and overall heat transfer performance and pressure drop. By introducing the oblique silicon fins to replace the conventional microchannel heat sink with continuous fins, the thermal boundary layer development along the channel surface is disrupted and a secondary flow of the fluid is created. The opening between the fins disrupts the momentum and the trailing edge of the thermal boundary layer of each oblique fin. This causes the leading edge to re-develop allowing the flow to remain in the developing state. This in turn enhances the heat transfer performance. Also, the secondary flow can produce mixing of the flow as the fluid flows through the fin opening improving the performance. The heat transfer coefficient of the channel with the oblique fins was enhanced by 80% when compared to the conventional channel. Within this investigation, Lee [13] studied the pressure drop effects of the oblique finned channel and a conventional channel. Minimal differences were obtained. With the oblique fins, and the above working conditions, there was a significant heat transfer performance enhancement with

little effects on pressure drop. Micro pin fins have proven to be effective in microchannels and is further analyzed in the following chapters.

A key factor that can influence the performance of heat transfer is the thermal conductivity of the fins, pins, and micro pin-fins used on the surface of the microchannel. With a material that has a higher thermal conductivity, the thermal resistance is decreased, and the temperature decreases. Zhong [4] investigated the effects of varying the properties of an array of microstructures placed along the bottom surface of the channel. When the thermal conductivity of the microstructures was varied, the temperature decreased and the pressure drop remained fairly constant. Having a material with a higher thermal conductivity for micro pin fins, the resistance at the interface decreases and the convection heat transfer performance is increased.

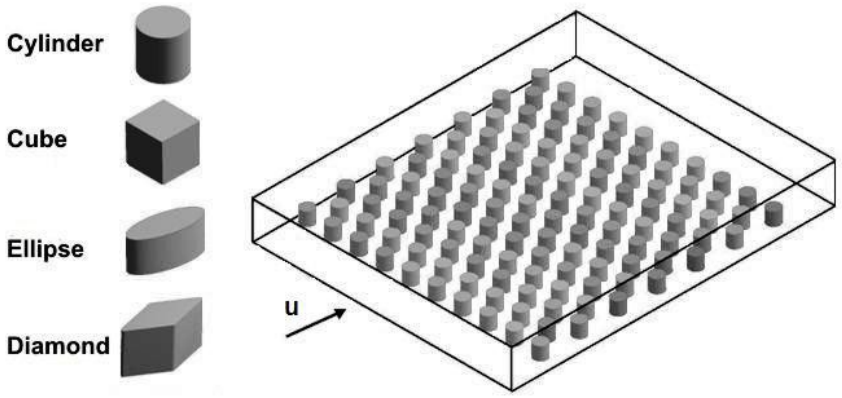

Figure 1.1: Different shapes that can be used for fins on the surface microchannels

One such material with high thermal and mechanical properties is carbon nanotubes (CNTs). CNTs are a novel material which can considerably improve microchannel cooling performance. CNTs are single sheets of graphite, named graphene, made up of a honeycomb shaped lattice representing an atomic layer of

the crystalline material, rolled up to make tubes with diameters of 0.45 to about 100 nm. The unique molecular structures of CNTs result in excellent physical and mechanical properties such as great mechanical strength, flexibility, and light weight. Their mechanical and chemical stability provides resistance against damage from external physical and chemical factors applied by their environment [3,14–16]. The main sp^2 hybridized bonds of CNTs, similar to the in-plane ones in graphite, place them among the strongest materials known today. CNTs have a Young's modulus as high as 1000 GPa, which is approximately 5 times higher than steel, and a tensile strength of about 63 GPa, which is almost 50 times higher than steel [3,17–19]. These cylindrical tubes remain stable up to very high temperatures similar to graphite with values approximately 4000 K [20].

There are two common types of CNTs: Single Walled Carbon Nanotubes (SWNTs) and Multiwalled Carbon Nanotubes (MWNTs). A SWNT is a cylindrical graphene shell with diameters ranging from 0.45 to 2.5 nm; it can be considered as a giant molecule. A MWNT consists of several concentric cylindrical shells with the outer diameters ranging from 2.5 to 60 nm and inner diameters between 1.5 to 40 nm. MWNTs can be considered a material similar to graphite. The distance between the concentric shells of a MWNT is approximately 3.4 Å [18].

For an ideal individual SWNT, the thermal conductivity has been reported to be higher than diamond, roughly 6000 W/mK. As a comparison, graphite has a thermal conductivity of about 2000 W/mK and diamond between 2000-2500 W/mK [18]. However, measurements on larger number of nanotubes resulted in thermal conductivity values as low as about 250 W/mK for SWNT samples and 20 W/mK for

MWNT samples [15,21,22]. The length and the thermal conductivity of a SWNTs are proportional to each other while the thermal conductivity does not depend linearly on the diameter [23–26].

CNTs can be grown directly onto minichannel surfaces by chemical vapor deposition (CVD). CVD is a low cost process and can produce CNTs in many fashions, either in bulk quantities or predefined micropatterns. The effects of CNTs clustered to form microstructures are still under investigation. CNTs are an excellent conducting material that has been tested in the use of increasing the performance of the microchannel heat sink. They are simple to fabricate, and because of their excellent cooling properties, CNTs are a favorable material to be used as micro pin fins.

Countless modifications to the surfaces of microchannels have been extensively studied and tested to improve the performance of the cooling devices. Surface roughness, grooves, and microfins are among the few alterations made to the microchannels in order to remove temperature from the surface using a single phase laminar flow. A further investigation on the optimal shape, size, and material effects of micro pin fins on the surface using water as the working fluid is discussed in Chapter 2. The next section will discuss the different fluids used to remove heat through a microchannel.

1.2. Fluids

Single phase fluids such as air and a liquid, before the fluid reaches its saturation temperature; have been used in microchannels to effectively enhance performance. Fluids flowing through the channel can transfer heat through convection from the heated surface and different fluid properties can influence the amount of heat that can be taken away due to their heat transfer coefficients. The most commonly used fluids in microchannels are air, water, and refrigerants, but there are limitations to their heat transferring capabilities due to their transport properties. Air has been a preferred fluid used in microchannels to cool electronic components because it is not harmful to the device; however, with heat fluxes going beyond 100 W/cm^2, air cooling methods have become inadequate for most applications. Liquids have a much higher convection heat transfer coefficient providing a better performance in cooling [6,11]. Fluids with higher convection heat transfer coefficients and higher specific heats are more effective in reducing heat from the heated surface [27]. Figure 1.2, a qualitative comparison of different heat transfer coefficients for commonly used fluids is presented along with their effectiveness in removing heat through forced and natural convection and in single and two phase flows. In the figure, the two phase flows display superiority in cooling due to the latent heat during the phase change process [28]; however, my work focuses on fluids at the single phase.

A fluid gaining popularity to flow through these channels is nanofluid. Nanofluid consists of nanosized particles usually no bigger than 100 nm in size

suspended in a base fluid such as water, ethylene glycol, engine oil or refrigerant [29–34]. In recent studies, nanofluids have emerged as having unique properties that consist of a very high thermal conductivity and stability. Metallic materials that have been used for these nanoparticles are oxide ceramics (Al_2O_3, CuO), nitride ceramics (AlN, SiN), carbide ceramics (SiC, TiC), metals (Cu, Au, Ag), semiconductors (SiC, TiC_2), carbon nanotubes and some composite materials ($Al_{70}Cu_{30}$). The most common materials used are the oxide ceramics. These nanoparticles have higher thermal conductivity than the base fluid and will in turn have increased effective thermal properties allowing for improved heat transfer performance. Although adding nanoparticles to a base fluid can influence the cooling process positively, there are challenges. These fluids leave sedimentation of particles, are subject to fouling and erosion, and may even clog the channel over time [35–40].

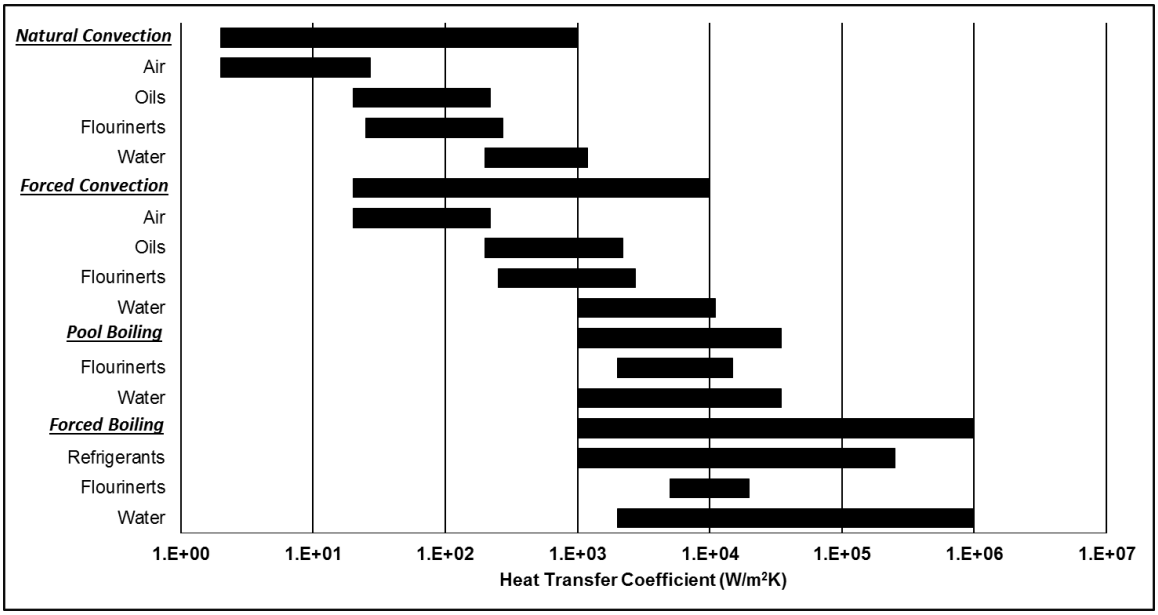

Figure 1.2: Thermal properties of different fluids of convection flow. Adapted from [41–43]

Pasupuleti [28] has applied many of these factors: fluid properties, material properties, fin shape, to his investigation in which he studied the effects of refrigerant R-123 as the working fluid in a single chip module setup. A single chip module is essentially a heat sink on a silicon microchip. The silicon wall is coated with mini ellipse-shaped fins to increase the surface area. In contrast to water, this refrigerant is considered a safe working fluid for electronic devices that do not require corrosion inhibiters or biocide. The results of refrigerant R-123 compared to that of water had similar results [28].

Many fluids have been used as a working media to flow through microchannels. Fluids with higher thermal conductivies cool more effectively. To further enhance the thermal performance, nanofluids with an optimal amount of volume concentration of particles can be used. The next section will review the different numerical techniques in closely approximating the flow and heat characteristics of a channel.

1.3. Computational Analysis of Microchannels

Experimentation of microchannels can be very costly in both time and money. The experimental setup has to be nearly perfect to get the desired effect and satisfy boundary conditions. In testing more than one experiment with varying parameters, the setup alone can take weeks. Computational analysis can cut costs and time while investigating the thermal performance. The analysis can help predict reasonable testing parameters for the experimentation of microchannels. The lattice Boltzmann method (LBM) can numerically calculate the interaction of small

particles and fluid flow. To simulate particles at the atomic level, computer software such as molecular dynamics (MD) is used. Computational fluid dynamics (CFD) is computer software that simulates the fluid as a continuum using the Navier-Stokes equations (NS). These numerical and computational methods can shorten the design cycle and lessen experimental costs.

In microchannels, the heat and fluid flow are very different from those in macrochannels. Because of the high surface volume ratio, the small surface defects affect the domain in these channels. The macroscopic no slip boundary conditions are not valid at this micro- and nano-scale under some circumstances [44]. The classification of the fluid regime is measured by the Knudsen number (Kn), which is defined by $Kn = \lambda/H$, where λ is the mean-free path and H is the characteristic length of the channel in which the fluid flows. The Kn characterizes the different flow regimes for which certain numerical equations can be used when calculating the flow patterns. This is shown in Figure 1.3.

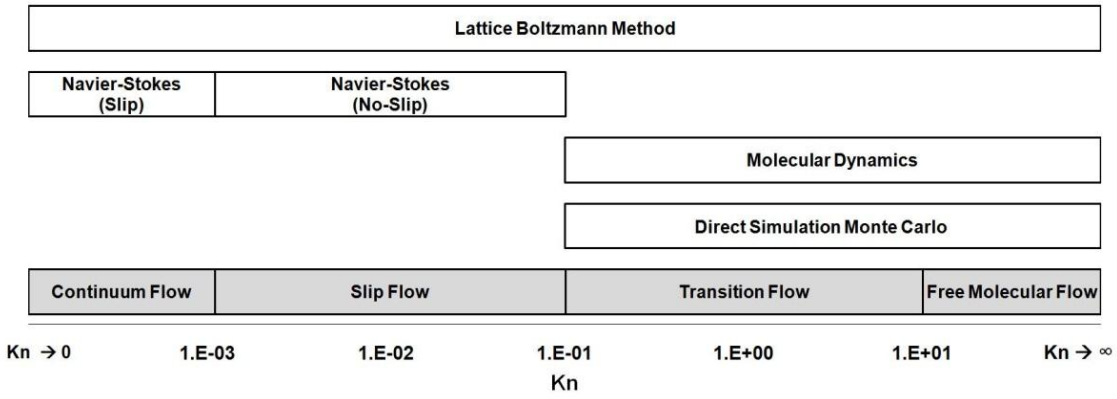

Figure 1.3: Flow characteristics based on the Knudsen number, Kn

If the Kn ≤ 10^{-3} the flow is assumed to be a continuum and the NS with the no slip boundary conditions can be utilized. For the flow regime where Kn > 10, the flow is known as a free molecular flow. Free molecular flow occurs where the molecules are larger than the size of the chamber or the object being tested, also known as a vacuum. A rarefied gas is neither a continuum nor a free molecular flow but the Kn is between the ranges. Between the continuum flow and the free molecular flow regimes, there is slip flow and transition flow characteristics. When the flow regime is 10^{-3} < Kn ≤ 10^{-1}, the NS with the slip boundary conditions can be used to assure accuracy. When the rarefaction factor becomes greater than 10^{-1}, the macro-scopic method based on the NS is no longer suffice and a more accurate method must be used. When the rarefaction factor is between 10^{-1} < Kn ≤ 10, particle based methods should be used. LBM, MD, and Direct simulation monte carlo (DSMC) are such methods that can sufficiently calculate the fluid flow regimes as the scales are reduced [45–48]. Therefore with the flow regime characteristics, microchannels with characteristic dimensions between 1 μm and 1 mm can be modeled using the NS equation because as the fluid will follow macro-scopic behavior. Channels with dimensions less than 1 μm will follow micro-scopic flow and NS can no longer be used [12,46,49–52]. Harley et al. [53], Araki et al. [54] and Arkilic et al. [55] all investigated the flow continuum in microchannels and concluded that the conventional equations were no longer adequate in predicting the flow patterns. Harley et al. [53] investigated gas flow through a channel with varying depths of 0.5-20 μm and a width of 100 μm using nitrogen, helium, and argon gas. The results were compared to the macroscopic calculations and they did

not correlate. Araki et al. [54] studied the frictional characteristics of nitrogen and helium and found that the frictional resistance of the gaseous flow is smaller in microchannels than that of a traditional channel. Arkilic et al. [55] investigated the deviation of the transport of gas in microchannels versus the continuum.

LBM can accurately simulate fluid flowing through a microchannel [52,56–60]. This simplified method of the kinetic equations is derived from the Boltzmann equations. Unlike other mathematical methods such as MD, and DSMC, LBM does not depend on distribution of the number of molecules, but concentrates on the distribution function dependent of the velocity coordinates. This method focuses on the local velocity averages at distinct locations [47,50,52,58,61]. As shown in Figure 1.3, these equations are suitable for all flow regimes. LBM is considered to be computationally stable, accurate, efficient, and easy to use. This method is capable of solving complex geometries, effortlessly implementing the boundary conditions, and is less difficult to compute, while avoiding the need to follow every particle in the system like MD, and DSMC [52,58,61]. Darbandi [47] uses the LBM to investigate a fluid flowing passed a confined cylinder in a microchannel with slip flow regime. A result justification through a comparison and an examination of the continuum and non-continuum flow past a confined cylinder in a microchannel was conducted [47]. The results suggested that the Kn increases when the cylinder was placed in the flow path, decreasing the hydraulic diameter. This method was chosen to describe a flow through a microchannel so I can capture the flow characteristics in all flow regimes and is further discussed in Chapter 4.

MD is a particle-based computer simulation program that can compute the thermal transport of properties in nanostructures at the atomic scale using classical and quantum physics. This method makes it possible to obtain the thermal resistances between a solid/solid, solid/liquid and liquid/liquid interface. MD is made up of two processes: equilibrium and non-equilibrium MD. The equilibrium MD is calculated based on the Green-Kubo relations; non-equilibrium MD is calculated using the Fourier laws [12]. Shibahara [62] examined the thermal resistance effects of a liquid/solid interface using MD simulations. The resistance was calculated by the heat flux and the temperature jump at the interface and was found that by increasing the density of the fluid, the thermal resistance decreases between the thermal transport of the solid and liquid. Kharazmi [63] investigated the effects of surface roughness or deviations along the surface of a fluid in a nanochannel using MD simulations. The wall-fluid interaction and the surface irregularity are important factors to the disturbance of the flow. The cavitation's and wall microstructures can vary the local density pattern yet still maintain an overall average [63]. MD can simulate the interaction at the solid fluid interface accurately in the molecular scale and while save time and money.

The CFD method, calculated through a commercial software package, is used to approximate the fluid mechanics and heat transfer characteristics of microchannels. CFD can be used in parallel to experimental setups in an effort to predict the flow and heat effects of the given surface modifications and the specified parameters and boundary conditions of a microchannel. CFD is based on the NS equations derived from Newton's second law of motion. NS is a set of equations that

describe the fluid flow behavior in a continuum. CFD simulations have been used to study the many different aspects of microchannels. Zhong [4] modeled a 2D simulation of a microchannel with arrays of microstructures on the bottom surface. A study of the effects of varying the geometry of the microstructures was completed, varying the fluid speed and changing the thermal conductivity of the fin material as they influence the thermal performance. When the results were compared to the mathematical calculations of the conservation of energy equations, they were almost identical to the CFD simulation results [4]. Srivastava [64] used the CFD software package, Fluent, to understand the effect of roughness on fluid flow characteristics. Three rectangular channels were simulated: two with different geometries of roughness and compared them to a smooth microchannel [64]. I used this method to model a minichannel with different micropin fin geometry and spacing and it is discussed in Chapter 2.

Reducing the size of a cooling system can increase the complexity of the model because the basic continuity equations are no longer valid. Depending on the numerical scheme and the size of the model can increase the cost and time of the system exponentially. Both Chapters 2 and 4 numerically model a microchannel using 2 different numerical schemes, CFD and LBM, respectively.

1.4. In Summary

This chapter has reviewed different techniques used in efforts to modify microchannels with single-phase, laminar flow. Some surface modifications discussed include adding micro-fins, grooves, and increasing surface roughness.

Many of these modifications have been successful in increasing the thermal performance; however, with advancements in technology, heat transfer in microchannels still needs to be further enhanced. CNT built onto the surface of microchannels can improve thermal performance because of impressive material and mechanical properties. Different configurations and geometries of CNT microstructures in mini/microchannels need to be further numerically and experimentally evaluated to maximize cooling of the electronic components. Chapter 2 discusses a design of a rectangular minichannel using different mirco pin fin geometries and spacing. An empirical formula was formulated to be able to predict the heat transfer and fluid flow characteristics of flow through a minichannel with pin fins on the heated surface. In Chapter 3, an experimental investigation of a microchannel using both water and Al_2O_3/H_2O nanofluid with MWNTs as the protruding surface structures is discussed. Mathematical analysis of microchannels can be done through LBM at both the micro- and nano-scale, whereas at the atomic scale one can use MD and CFD for the continuum regime. Each of the mathematical processes can accurately approximate the thermal performance of the channel for their specified Kn. Chapter 4 discusses the use of the LBM to portray a rectangular channel with nanoparticles suspended in the base fluid. An approximation of the results for increased surface roughness when using both water and nanoparticles was found using equations for ideal fins. A cooling mechanism needs to be designed or modified to efficiently cool electronic components and keep them from malfunctioning in order for electronic innovation to continue.

Chapter 2

Design of Short Micro Pin Fins in Minichannels

As stated in Chapter 1, small channels have been effective in removing heat through convection from the surface of a microchip. Forced and natural convection from fluids flowing through these channels can dissipate high surface temperatures. Although it has excellent cooling capabilities, these channels experience a high pressure drop as fluid flows. This can cause problems when trying to re-circulate the fluid with a pump [1]. Because of the innovations in electrical devices, optimizing these channels has been an important part of the research industry.

Modifications to mini/microchannels to enhance thermal performance are being examined by many researchers. Data shows that increasing surface roughness [8,65] and/or applying small cavities [7,10,11,66,67] on the channel walls will improve the heat transfer. The addition of fins or small cavities on the surfaces of

the channel creates small disturbances within the fluid which allow fluid to mix and enhancing heat transfer.

Fins made up of different shapes, sizes, and materials can be placed in different arrangements to increase the channel surface area and affect the heat transfer performance and pressure drop characteristics [68]. Many modifications to the microchannel's surface have been investigated in enhancing the thermal performance. A small review of some of the work in single phase heat transfer enhancement techniques in mini/micochannels and microdevices are discussed in [69,70]. Zhong et al. [4] examined the effects of varying the thermal conductivity of the fins structures on the surface of a microchannel. With increasing thermal conductivity, temperature decreases with little effect on pressure drop. Lee et al. [71] investigated a microchannel with silicon based oblique fins and compared it with an unfinned channel and obtained slight increase in heat transfer performance with little or no increase in pressure drop. John et al. [72,73] computationally investigated the effects of fin shape and found that the optimal shape of the fin was dependent on the flow rate used.

Peles et al. [74] analytically completed a heat transfer analysis over a bank of cylindrical micro pin fins. It was concluded that at high Reynolds number (Re) a denser pin fin configuration was more efficient, and at low, Re, a more sparse arrangement was recommended. Selvarasu et al. [75] and Shafeie et al. [76] also examined the density of cylindrical fins minichannel. When measuring heat capacity and pressure drop, channels with fins of lower density provided the best performance in the laminar flow however the effects of the increase pressure drop

greatly outweighed the increase of heat removed. Koz et al. [77,78] also computationally completed a parametric study using cylindrical micro pin fins to evaluate the effects of fin height vs. fin diameter and the longitudinal and transverse distances to diameter ratios.

Reyes et al. [79] investigated the effects of fin clearance of microchannels and found that there was a decrease in thermal performance; however, less power to pump the fluid into the system was needed. Min et al. [80] found that with fins about 60% of the channel height yields less resistance and improves cooling performance.

Heat transfer and pressure drop characteristics for liquid single phase flow over an array of micro pin fins in a minichannel are investigated in [81–85]. Empirical correlations of Nusselt number (Nu) and Darcy friction factor (f) were obtained and compared to previous work. Kosar et al. [86] obtained a friction factor correlation across a bank of low aspect ratio pin fins. Vanapalli et al. [12] investigated the pillar 'fin' shape which contains the lowest friction factor using nitrogen gas flowing through the microchannel. Various geometries were tested in staggered arrangements and found that pillars with the sine shape cross-sections provide the lowest friction factor. Kosar et al. [87] further investigated the effects of pin fin aspect ratio, fin configuration, fin spacing, and fin shape for pressure drop. It was concluded that the existing conventional correlations cannot accurately capture the micro scale interaction of the fluid and the fins.

All of these studies have demonstrated some progress in the development of enhancing cooling for electrical devices but the design fin material, size, and geometry still need to be determined.

With the increasing desire to improve the cooling techniques for small electrical components, advanced materials with high thermal properties need to be exploited. Fins made up of silicon or carbon nanotubes (CNTs), both containing high thermal properties, have been the choice of materials to improve thermal performance. CNTs have a unique molecular structure that contains excellent physical and mechanical properties including great strength, chemical stability, and high thermal conductivity. Thermal conductivities of CNTs have been calculated to be as high as 6000 W/mK- higher than diamond at 2000-2500 W/mK and graphite at 2000 W/mK [18,88]. There are ongoing investigations in finding an effective thermal conductivity when clumping CNTs together to form a fin. Assembling the fins together decreases the thermal conductivity and it is unknown what the relation is to calculate that value. Some say it is as high as 400 W/mK [15,21,22]. CNTs can be grown directly on the channel surface in mass quantities using chemical vapor deposition. There are a few of ways to get the desired shapes of fins. One is a metal catalyst is placed on the surface in the desired shapes of the fins and grown directly on the surface. Another way to form the shaped fins is to coat the surface for a given area with CNTs and laser cut fins to obtain the desired geometry. Both processes for growing fins on the surface of a micro or mini channel are further described in [21,89,90].

Microstructures can be placed in a staggered or inline formation along the surfaces of the walls. These fins can be different shapes and sizes and can be placed in various patterns in order to improve the thermal performance. Shape of the fins affect the motion of flow by producing a mixing in the flow as the fluid passes through the channel, improving the performance. Optimizing the fins shapes, topology, and dimensions to achieve the maximum thermal performance has not been thoroughly executed with corresponding heat transfer and friction factor correlations. The chapter presents the work conducted by Tullius et al. [91,92], which discusses the effects of CNT micro fins on the surface of a minichannel in a staggered formation. In order to completely design the fins used, a few comparisons are conducted. Different pin fin geometries are modeled and compared for various flow rates ranging from 0.0625-1 m/s and inputted heat fluxes ranging from 10-150 W/cm^2 in the single phase regime. Optimum fin height, width, and spacing of the square shaped pin fin are then modeled. Also, fin material properties are varied to observe the affects. All these simulations are compared to the base unfinned channel to observe the enhancement obtained with the microstructures. Results are provided in terms of average Nu versus Re and pressure drop versus axial velocity. Nu and friction factor correlations then are obtained and compared to previous studies.

2.1. Computational Modeling

For these simulations the flow regime is considered to be a continuum flow. The flow through this model can be solved using macroscopic relations or the

Navier-Stokes (NS) equations. The basic governing equations for a steady-state, incompressible flow are:

Continuity equations

$$\left(\nabla \cdot \rho u\right) = 0 \tag{2.1}$$

Conservation of momentum

$$\rho\left(u \cdot \nabla u\right) = -\nabla p + \mu \nabla^2 u \tag{2.2}$$

Conservation of energy

$$\rho c_p \left(u \cdot \nabla T\right) = k \nabla^2 T \tag{2.3}$$

The geometry is meshed based on the finite volume method. In this technique, the region is divided into small sub-regions known as control volumes. Approximations of the values solved by the NS equations are obtained for each control volume. Combining the control volumes, the values display the behavior of the whole region as an entity profiling the fluid flowing through this rectangular channel. ANSYS CFX, based on the NS fluid flow equations, is used to model the flow past the pin fins in a staggered array in the minichannel and solves the governing equations iteratively for each control volume. The accuracy of the solution is proportional to the size and shape of the control volume and the size of the final residuals. The convergence criterion for the solution is residuals of less than 10^{-6} for both continuity and momentum. Each model contained a fine mesh surrounding the finned section with a less dense mesh as the channel extends to the inlet and outlet.

Four different comparisons of finned minichannels to the no finned channel are completed in this paper in order to optimize the mirco pin fins using multiple flow rates and heat fluxes: 1) six different pin finned shapes, 2) varying height spacing of fins square pin fins, 3) fin width and spacing, and 4) applying multiple material properties to the square pin finned geometry. A rectangular minichannel is modeled with dimensions, 15 x 1 x 45 mm^3 (w_c x h_c x d_c). Micron sized structures, acting as pin fins to increase the surface area, are placed along a 15 x 25 mm^2 (w_c x d_h) area on the bottom surface of the channel in a staggered array with a height, h_f , and a width, w_f . A constant heat flux is applied to the bottom of the channel. This is shown in Figure 2.1. The dimensions and shape of the channel were chosen for simplicity of the model as well as ensuring the flow is hydrodynamically developed before the fluid reaches the heated region.

Six geometrical shapes are investigated for the fins: circle, square, triangle, ellipse, diamond and hexagon. They were chosen to get the effects of a variety of shapes that may or may not be the most aerodynamic in nature. The dimensions and shapes modeled in this study are shown in Figure 2.1b. The transverse and longitudinal spacing of the fins, S_t and S_t , for this study is equal to double the width of the fin, $2w_f$. Fin height, h_f , is half the length of the channel height, h_c , or 0.5 mm. A staggered formation is proven to provide an enhanced heat transfer compared to an inline array due to more mixing within the fluid. Therefore, to obtain a staggered formation, the rows are offset by w_f . For all geometries, the fin material property used is that of CNTs; however, because the thermal conductivity is unknown when

nanotubes are clustered together to form fins, an effective thermal conductivity of 400 W/mK is used [4]. This study was simulated using multiple heat flux and flow rate inputs.

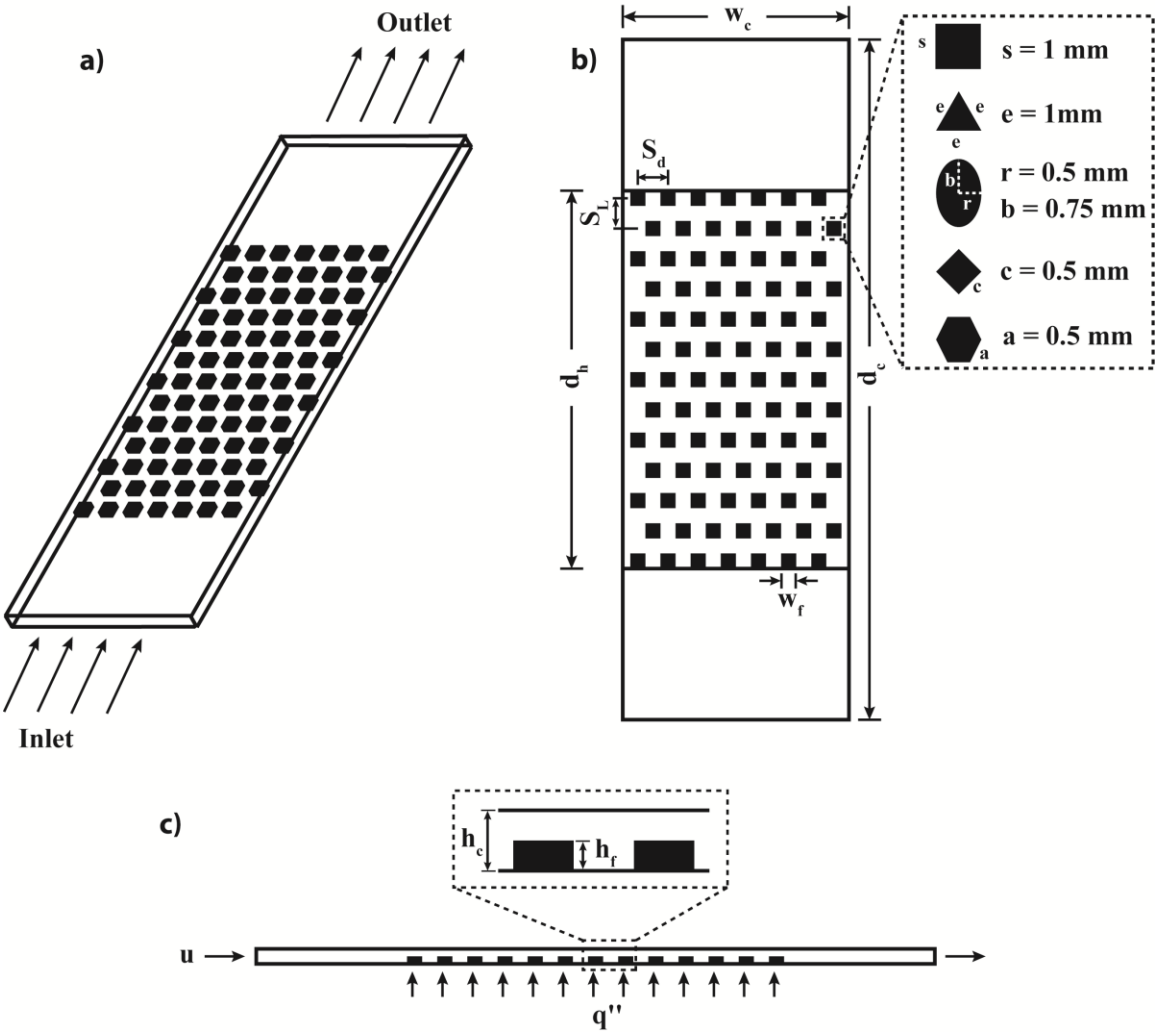

Figure 2.1: Minichannel model with dimensions: a) Isometric view of minichannel; b) Fins geometry of six different shapes; c) Side view of the channel with magnified view of fins relative to the channel height

The next comparison uses the square geometry for the fins. Using the square geometry and CNT material properties as the first study, channel clearance is varied using fin to channel height ratios, h_f/h_c, between 0.25-0.75. Channel clearance can

be defined as the subtraction of the fin height from the height of the channel. A side profile of the fins relative to the channel is shown in Figure 2.1c. This study is designed to understand the optimum fin height with respect to the channel and is compared to the channel with no fins.

The third investigation was conducted in efforts to optimize the fin dimensions and spacing using the square pin fin geometry. Because the fin width, w_f, fin spacing, S_t, S_L, and number of fins, N, are all dependent on one another, the ratio of fin width times the number of fins in the row, N_x, to the channel width, $N_x w_f / w_c$, is kept constant at a value of 0.5. The spacing S_t and S_L are kept equal to double the fin width. The height of the fins to the channel height is kept at half the channel clearance and the number of fins along each row varies based on the width and the spacing of the fins. Fin width is varied from 0.5-2.5 mm resulting in 15-3 fins per row, respectively. Once the optimum size of fins is determined, the spacing is varied using the fin's width of 1.25 mm. Unlike the previous spacing that is the same as the fin width, the spacing is reduced to 2 mm and 2.25 mm while maintaining the same number of fins in the row. These were all compared to the smooth, unfinned channel.

The fourth investigation is performed to understand how fin material properties enhance heat transfer of minichannels. The same square pin fin geometry is used similar to the first study with the fin width at 1 mm, spacing at 2 mm, and the fin height half of the channel height. Because the effective thermal conductivity of CNTs grouped together to form fins is unknown, the thermal conductivity is differed

with values ranging from 200-800 W/mK. In addition to varying the thermal conductivity of CNTs, silicon, copper, and aluminum are also used as the fin material. Table 2.1 has a list of properties pertaining to the different fin materials. Table 2.2 summarizes the modeled simulations for each study giving the shapes and dimensions used for each simulation.

Fin Material	k (W/mK)	c_p (J/kgK)	ρ (kg/m^3)
Aluminum	237	903	2702
CNT	200-800	450	1300
Copper	401	385	8933
Silicon	148	712	2330

Table 2.1: Material Properties for Fin Material Comparison

Initial inlet temperature and outlet static pressure values applied to the model are assumed for all simulations to be 25°C and 0 Pa, respectively. To monitor the heat transfer coefficient and the heat transfer rate, the outer walls of the channel are set to be adiabatic. No-slip boundary conditions and no interfacial resistance are assumed at the wall/fluid interface. Water is used as the working fluid flowing through this heat exchanger with velocities ranging from 0.0625-1 m/s through the inlet of the channel. These simulations are in the single phase regime and fluid properties are kept constant throughout the simulations. Water flows past the pin fins carrying heat subjected by the bottom surface. A constant heat flux ranging from 10-150 W/m^2 is applied to a 15 x 25 mm^2 area at the bottom of the channel. With the constant heat flux, the different geometry of the nanotube bundles, and the forced convection, the temperature across the surface of the microchip and the bulk temperature of the fluid vary. To accurately obtain the heat transfer coefficient, h, across the microchip region for the simulations, an average h was obtained.

Study	Shape	Fin Material	w_f (mm)	N_x	N	$\frac{N_x \times w_f}{w_c}$	h_f (mm)	$\frac{h_f}{h_c}$	S_t (mm)	S_L (mm)
1	Circle	CNT	1	7	91	7/15	0.5	0.5	2	2
	Square	CNT	1	7	91	7/15	0.5	0.5	2	2
	Triangle	CNT	1	7	91	7/15	0.5	0.5	2	2
	Ellipse	CNT	1	7	91	7/15	0.5	0.5	2	2
	Diamond	CNT	1	7	91	7/15	0.5	0.5	2	2
	Hexagon	CNT	1	7	91	7/15	0.5	0.5	2	2
2	Square	CNT	1	7	91	7/15	0.25	0.25	2	2
	Square	CNT	1	7	91	7/15	0.33	0.33	2	2
	Square	CNT	1	7	91	7/15	0.5	0.5	2	2
	Square	CNT	1	7	91	7/15	0.66	0.66	2	2
	Square	CNT	1	7	91	7/15	0.75	0.75	2	2
3	Square	CNT	0.5	15	375	1/2	0.5	0.5	1	1
	Square	CNT	0.75	10	170	1/2	0.5	0.5	1.5	1.5
	Square	CNT	1.25	6	72	1/2	0.5	0.5	2	2
	Square	CNT	1.25	6	72	1/2	0.5	0.5	2.25	2.25
	Square	CNT	1.25	6	66	1/2	0.5	0.5	2.5	2.5
	Square	CNT	1.5	5	40	1/2	0.5	0.5	3	3
	Square	CNT	2.5	3	15	1/2	0.5	0.5	5	5
4	Square	CNT	1	7	91	7/15	0.5	0.5	2	2
	Square	Silicon	1	7	91	7/15	0.5	0.5	2	2
	Square	Copper	1	7	91	7/15	0.5	0.5	2	2
	Square	Aluminum	1	7	91	7/15	0.5	0.5	2	2

Table 2.2: Summary of Simulations Performed

There were some uncertainties within the model that can increase the error in the approximation. No slip boundary conditions are used to define these simulations at the fluid solid interfaces. As the scales start moving toward the micro or nano regime, the conventional continuum calculations can no longer be used. Also, the resistance created at the interface of the CNTs and the working fluid, water, is still a major issue. In this model, no interfacial resistance is applied. The CNT fins are modeled as a solid emerging out from the surface rather than bundles of nanotubes. CNT micro pin fins are made up of many nanotubes where the fluid penetrates through the small gaps, or nanochannels, allowing for an increased in convection within the system. As shown in Shenoy et al. [90], CNTs absorb the fluid

at high temperatures creating a porous like material and increases heat transfer due to a hastened nucleate boiling onset initiating phase change. This assumption in the model may underestimate the thermal performance of CNT fins. Also, there are ongoing investigations of the effective thermal conductivities of CNT bundles; therefore, an estimation of an effective thermal conductivity is used. There are many assumptions made within this program that increases the error of the approximation, however, the general trend should be similar.

2.2. Results and Discussion

This work was conducted to understand how the shape, topology, and the material properties of micro pin fins on the surface of a minichannel can affect thermal performance. Four different studies were conducted to optimize the minichannel in order to obtain the maximum amount of heat transferred. The results are presented by both comparing two non-dimensional units, average Re and Nu, and by relating change in pressure, Δp, and axial velocity, u. Average Re and Nu are collected for the different inputted heat fluxes and flow rates. The Re is defined as the multiplication of the density, ρ, average axial velocity, u, and the hydraulic diameter of the channel, D_c, over the dynamic viscosity, μ. Average axial velocity was obtained as the fluid flowed across the fin bank.

$$\mathrm{Re} = \frac{\rho u D_c}{\mu} \tag{2.4}$$

Nu is proportional to the average heat transfer coefficient, h, and the hydraulic diameter of the channel, and non-proportional to the thermal conductivity, k.

$$Nu = \frac{hD_c}{k} \tag{2.5}$$

The average heat transfer coefficient is obtained by the amount of surface area of the fins and the base that the fluid interacts with. The expression is given below.

$$h = \frac{\left(h_{fin}A_{fin} + h_b A_b\right)}{\left(A_{fin} + A_b\right)} \tag{2.6}$$

h_{fin} and h_b are the heat transfer coefficients of the fin and the base of the heated region only; A_{fin} and A_b are the surface areas in which the fluid touches the fin and the heated base region, respectively. The heat transfer coefficient of the fin and the base at the fluid interface is obtained by

$$h = \frac{q}{T_w - T_{nw}} \tag{2.7}$$

where q is the wall heat flux, T_w is the temperature of the wall and T_{nw} is the near wall temperature. Pressure drop is determined across the pin fins only to avoid any entrance and exit effects of the fluid flow using a maximum axial velocity. The results for all of the studies are given below.

2.2.1. Different Shaped Micro Fins

For the first investigation, results of different finned shaped microstructures on surfaces of minichannels are compared to the smooth, unfinned channel. With increasing Re, Nu values increase for all minichannel simulations. The Nu for the triangle, diamond, square and hexagon shaped fins have similar values with a

maximum average Nu difference of ≈ 12% for higher Re. For this data, triangular shaped fins showed better thermal performance. The circle and ellipse shaped portrayed a thermal performance is less effective than the triangle shaped fins by about 22% and 37%, respectively, however, still more efficient than the unfinned channel. For lower Re, the Nu increase is very high compared to the unfinned channel and at higher Re the gap decreases to have a 60% and 45% performance enhancement for the circular and ellipse shaped fins respectfully. Figure 2.2a and 2.2b reflect the results of this study.

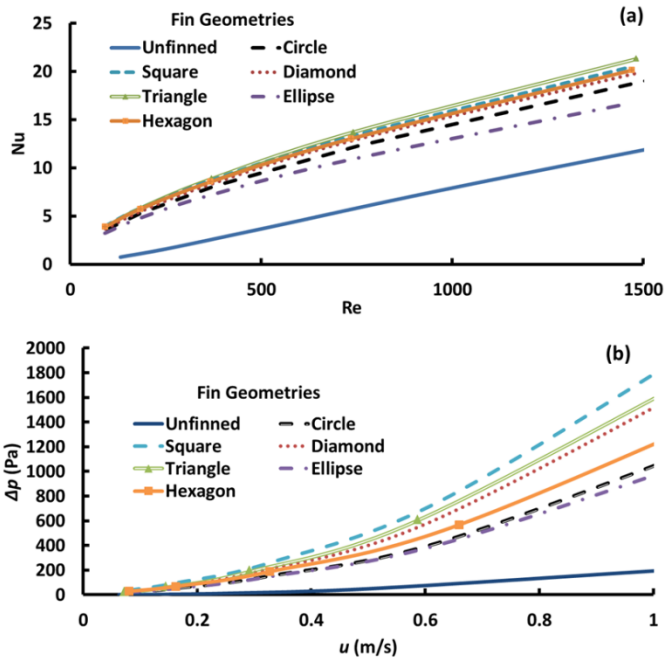

Figure 2.2: Results for different fin geometry: a) Nusselt number, Nu, versus Reynolds number, Re; b) Pressure drop, Δp, across the micro pin fins versus maximum axial velocity, u_{max}

With the addition of fins, there is an increase of pressure drop. A value too high can create problems for the pumps to flow fluid through the minichannel. As the velocity increases, the pressure drop increases for all models. The square pin fin

curve has the highest pressure drop with up to about 2.5 kPa followed by the next cluster of shapes: triangle and diamond. This increase is much higher than the unfinned channel which yields a max pressure drop of 0.2 kPa for the same Re. Circular shaped fin gives a max pressure drop of about 1.6 kPa for the highest flow rate. The ellipse shape shows a smallest pressure drop just under the circle shaped fin with a max pressure drop of 1.4 kPa. The shapes that are more aerodynamic reveal a lower pressure drop because there is less separation of the fluid from the solid body. The opening between the fins disrupts the momentum and the trailing edge of the thermal boundary layer of each oblique fin. This causes the leading edge to re-develop allowing the flow to remain in the developing state. The additions of fins show a big impact in the performance of the heat exchanger.

2.2.2. Different Micro Fin Height

Figure 2.3a and 2.3b display the results for different channel clearances. The fin heights are varied from 25% to 75% the length of the channel height. With increasing fin height, the thermal performance increases with increasing Re. From the lowest fin height at 0.25 mm, compared to the unfinned channel, the Nu increase is very high at low Re and the gap decreases to ≈ 58% for high Re. From the largest channel clearance, $h_f = 0.75\,\text{mm}$, to the smallest, $h_f = 0.25\,\text{mm}$, there is a Nu increase of ≈ 44%. As the fins height is increased, the pressure drop drastically increases. Pressure drop from the largest channel clearance is 0.98 kPa and the smallest channel clearance increases to 7.4 kPa. Because there is a large pressure drop difference for the increasing height and the small Nu relative increase, the

suggested fin height is dependent on the available pump parameters used within the cooling apparatus.

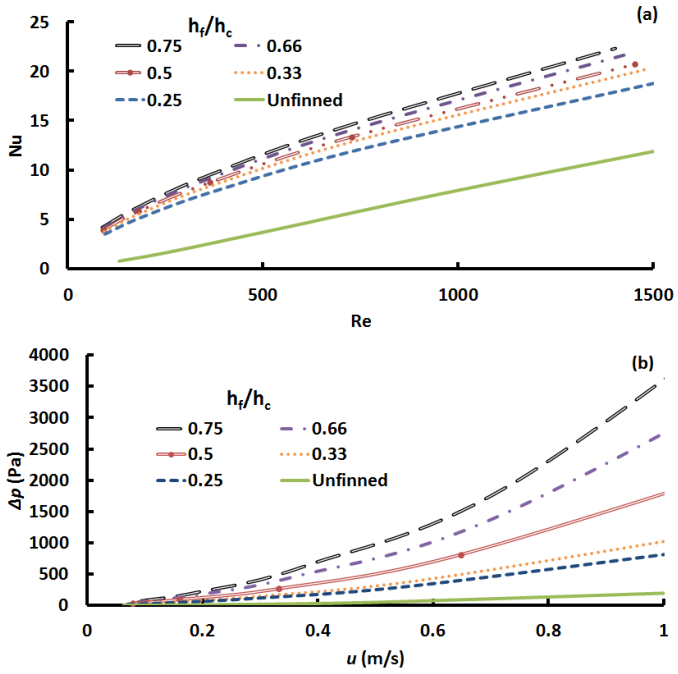

Figure 2.3: Results for different ratios of fin height, h_f, to height of channel, h_c: a) Nusselt number, Nu, versus Reynolds number, Re; b) Pressure drop, Δp, across the micro pin fins versus maximum axial velocity, u_{max}

2.2.3. Different Micro Fin Width and Spacing

For the third investigation, the fins spacing, width, and number of fins was varied in the channel. Like stated before these parameters are all dependent of each other which made it difficult to isolate. Therefore to perform this study, a ratio of the total fin width in the x direction of one row to the channel width was held constant. The total length of the square fins occupied in a given row was equal to the total length the fluid flowed through the channel. Initially the spacing between the fins and each row was kept to two times the fin width, $S_t = S_L = 2w_f$, similar to the

previous studies. It was discovered that with smaller fin width and spacing, i.e. number of fins was higher, the Nu value was greater than other fins. Fins with width of 0.5 mm projected an 88% higher Nu values than the unfinned channel and 38% higher Nu values than the lowest curve of fins width and spacing at 2.5 mm. Fins with width 2.5 mm still yield a higher Nu value about 50% greater than the unfinned channel with higher Re. This was shown in Figure 2.4a. While the smaller fin width and spacing provides higher performance, pressure drop between across the fins is sacrificed. As the fin dimensions are reduced, the pressure drop increases. Fins with spacing and width of 1 mm and 0.5 mm the pressure drop is about 15% compared to the bigger fin width and spacing of 2.5 mm and 5 mm and about 4% compared to the unfinned channel. The corresponding graph displaying these results is Figure 2.4b. The bigger fins express a smaller pressure drop across the channel. This is probably due to the fewer disturbances the fluid has within the channel. It is interesting to note that for both the pressure drop and the Nu the fins with width of 0.5 mm and 0.75 mm are very similar. The optimum fin width is capped out between these two widths. Similar to the other conclusion, specification of the pump parameters should be taken into account on the number of fins the system can have before the pressure drop is too high.

Once it was determined that smaller fins width and spacing would produce higher thermal performance within the channel, the fin width and number of fins across one row was kept constant at 1.25 mm and 6, respectively, but the spacing between fins varied. As the fin spacing was decreased, to get the most efficient use out of the fins, the columns were centered in the middle of the channel. From the

results shown in Figure 2.4c and 2.4d, as the spacing was closer to equal the fin width, the performance was greater. From the smallest spacing to the largest, i.e. 2 mm to 2.5 mm, there was a 6% enhancement for larger fins spacing. With a decrease in fin spacing, the pressure drop increases. There is about 5% increase in pressure drop from the 2.5 mm spacing to the 2 mm. From the results, it can be concluded that with decrease in width/spacing creates higher thermal performance with a sacrifice in pressure drop. By only changing the spacing, the maximum spacing yields a higher thermal performance providing a minimal pressure drop.

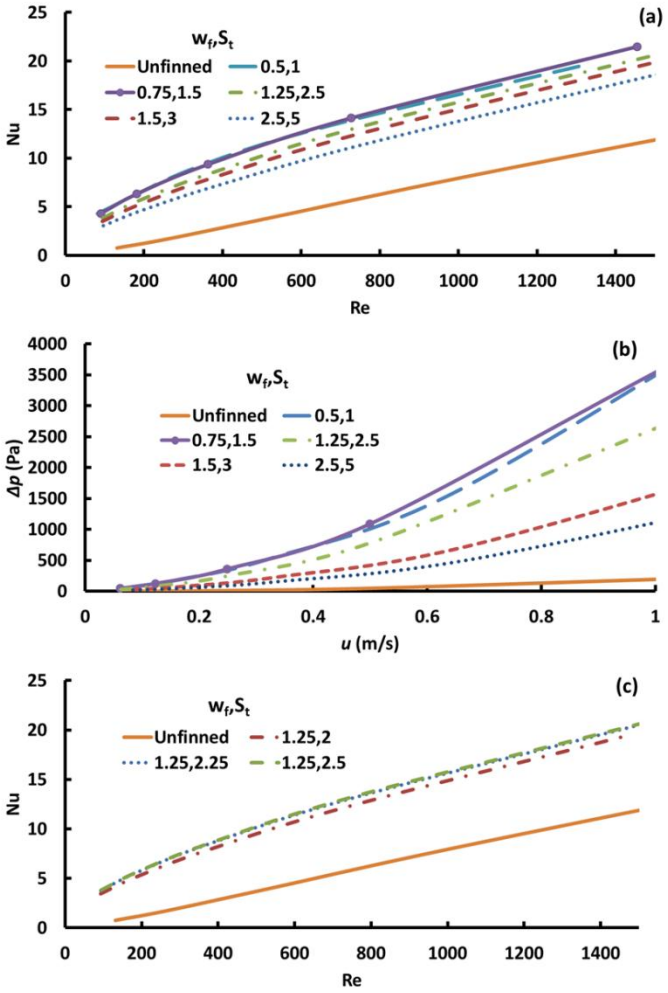

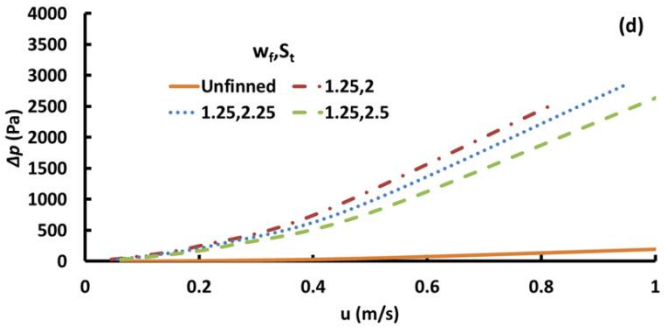

Figure 2.4: Results for varying fin width, w_f, spacing, S_t, and number of fins, N: a) Nusselt number, Nu, versus Reynolds number, Re, for different fin width and spacing when $2w_f = S_t$; b) Pressure drop, Δp, versus maximum axial velocity, u_{max}, for fin spacing and width when $2w_f = S_t$; c) Nusselt number, Nu, versus Reynolds number, Re, for different fin spacing while width is constant, w_f = 1.25 mm; d) Pressure drop, Δp, versus maximum axial velocity, u_{max}, for different fin spacing while width is constant, w_f = 1.25 mm

2.2.4. Different Micro Fin Material Properties

In the final study, CNTs, silicon, copper, and aluminum material properties are used as the fin material. The CNTs effective thermal conductivity is varied from 200-800 W/mK because that value is still unknown. For single phase flows, changing material properties show little variation within the Nu values, yet, they are still larger than unfinned channel. The results portraying this study are shown in Figure 2.5. These findings show that the chosen fin material had little effect on the Nu values. In this study, CNTs are modeled as a solid fin but in reality the fins are more of a porous media that contain small gaps where the fluid can penetrate. The nanotubes can also initiate nucleation sites initiating boiling and therefore enhancing heat transfer. Because of this, the results for the CNT fins are underestimated using this program. More accurate studies need to be conducted in order to verify this assumption made. From this conclusion, the CNTs should yield a

greater thermal performance than the other fins. Pressure drops display no difference between the fin materials because the geometry remained the same for this section of the study.

Pressure drop for these studies have shown critical in optimizing fin geometry and topology. For a single phase, laminar, flow through a minichannel, Nu values for pin fins did show improvement compared to the unfinned channel; however, various shapes, heights, widths, spacing and thermal properties only show slight deviation.

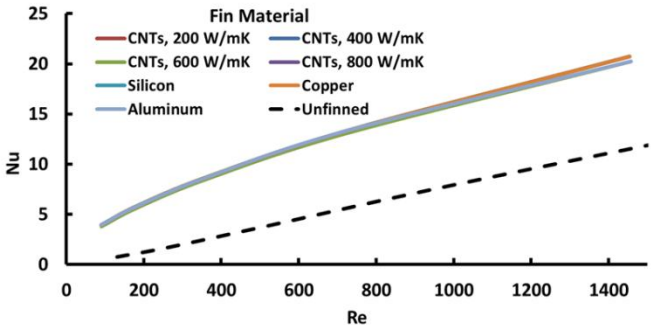

Figure 2.5: Nusselt number, Nu, versus Reynolds number, Re, for selected fin material properties

2.3. Mathematical Correlations

To further understand our numerical data, empirical relationships between 1) Nu_f and Re_f and 2) $u_{\max}$ and Δp were established. This was completed in order to be able to predict the correlations based on their geometrical parameters. Expressions for Nu_f and f were developed for this study. Once they were established, they were compared to other pin fin studies that have developed

expressions for Nu_f and f. These expressions were obtained based on the first two studies: varying geometries and heights. Our correlations were then applied to a specific example and results are presented in terms of Nu_f, and Δp.

2.3.1. Heat Transfer

The conventional correlation for Nu_f for flow through a tube bank is typically in the form

$$\mathrm{Nu}_f = C_{Nu}\,\mathrm{Re}_f^{X}\,\mathrm{Pr}^{1/3} \tag{2.8}$$

developed by Zukauskas [93], where C_{Nu} and X are constants and Pr is the Prandtl number corresponding to the fluid. Because the height and shape of the fins and the clearance of above the fins are a major focus in this paper, the new expression incorporates more terms to further define the geometry of the fins: S_L, S_t, h_f, and the channel clearance, dh. From the data collected, using a best fit curve the unknown parameters were obtained for new Nu_f correlations for each shape. The new expressions are in the form of Equation 2.9.

$$Nu_f = C_{Nu}\left(\frac{S_L}{D_f}\right)^{S}\left(\frac{S_t}{D_f}\right)^{U}\left(\frac{h_f}{D_f}\right)^{V}\left(1+\frac{dh}{D_f}\right)^{W}\mathrm{Re}_f^{X}\,\mathrm{Pr}^{Y}\left(\frac{\mathrm{Pr}}{\mathrm{Pr}_s}\right)^{Z} \tag{2.9}$$

$C_{Nu}, S, U, V, W, X, Y,$ and Z are all constants determined from the numerical data. These correlations were compared to others developed by previous studies [81,82,93–101]. For each shape, the expression differs only with the constant, C_{Nu} .The exponents are all the same. This is shown in Equation 2.10.

$$Nu_f = C_{Nu}\left(\frac{S_L}{D_f}\right)^{0.2}\left(\frac{S_t}{D_f}\right)^{0.2}\left(\frac{h_f}{D_f}\right)^{0.25}\left(1+\frac{dh}{D_f}\right)^{0.4}\mathrm{Re}_f^{0.6}\,\mathrm{Pr}^{0.36}\left(\frac{\mathrm{Pr}}{\mathrm{Pr}_s}\right)^{0.25} \quad 2.10$$

for

Geometry	Circle	Square	Diamond	Triangle	Ellipse	Hexagon
$\boldsymbol{C_{Nu}}$	0.08	0.0937	0.036	0.0454	0.0936	0.0752

Re_f for these correlations are determined based on the hydraulic diameters of the fins, D_f, and the average velocity flowing through the fins. Re_f and D_f are defined in Equations 2.11 and 2.12, respectively.

$$\mathrm{Re}_f = \frac{\rho u D_f}{\mu} \quad 2.11$$

$$D_f = \frac{4A_f}{P_f} \quad 2.12$$

A_f is the cross-sectional area of the fin and P_f is the perimeter. These expressions are effective for Re_f in the laminar regime.

These results are compared to other generated correlations using the mean absolute error, *MAE,* defined in Equation 2.13 [82,84,86,102]. This equation is an average error between the data received from the computational runs and the data predicted from the correlation provided. The values with the smallest *MAE* express the better correlation.

$$MAE = \frac{1}{M}\sum_{i=1}^{M}\frac{\left|data - data_{pred}\right|}{data_{pred}} \times 100\% \quad 2.13$$

The parameter M is the number of velocities used in the study. Table 2.3 shows the Nu_f correlations for the corresponding references and the MAE value with respect to the numerical data obtained. It is separated into the geometrical shapes in which the correlations were developed from. The comparisons can also be further seen in Figure 2.6. From Table 2.3, the MAE for the correlations developed for each shape is under 10. Liu et al. [101], Metzger et al. [97], and Qu and Siu-Ho [82] show decent error values closest to the numerical data with values of 2.1/8.9, 7.62, and 28.76/29.67, respectively. Correlations developed using micro-pin fins versus the conventional macro scales fins in general had smaller MAE values. With the exception of the Metzger et al. [97] correlation, conventional correlations are not adequate to predict the heat transfer across a micro pin fin array in a minichannel. Overall the new Nu_f correlation obtained is a good representation for our data.

Reference	Correlations	Scale	MAE
Circle			
Present Circle Correlation [92]	$Nu_f = 0.08\left(\frac{S_L}{D_f}\right)^{0.2}\left(\frac{S_t}{D_f}\right)^{0.2}\left(\frac{h_f}{D_f}\right)^{0.25}\left(1+\frac{dh}{D_f}\right)^{0.4}\mathrm{Re}_f^{0.6}\,\mathrm{Pr}^{0.36}\left(\frac{\mathrm{Pr}}{\mathrm{Pr}_s}\right)^{0.25}$	Mini	9.57
Hwang and Yao [94]	$Nu_f = 0.83\lambda^{1/3}\,\mathrm{Re}_f^{1/3}\,\mathrm{Pr}^{1/3}\left(\mu_f/\mu_s\right)^{0.14}$ $\lambda = \beta^4 - 1/\left(\left(1+\beta^4\right)\ln\left(\beta^2\right)+\left(1-\beta^4\right)\right)$ $\beta = \left(1/1-\xi\right)^{1/2};\ \xi = S_t S_L - A_f/S_t S_L$	Macro	37.59
Khan et al [95]	$Nu_f = C_1\,\mathrm{Re}_f^{1/2}\,\mathrm{Pr}^{1/3}$ $C_1 = \left(0.61\left(\frac{S_t}{D_f}\right)^{0.591}\left(\frac{S_L}{D_f}\right)^{0.053}\right)\Big/\left(\left(\left(\frac{S_t}{D_f}-1\right)^{0.5}\left(1-2\exp\left(-1.09\frac{S_t}{D_f}\right)\right)\right)\right)$	Mini	82.62

Reference	Correlations	Scale	MAE
Circle			
Kosar and Peles [96]	$Nu_f = 0.0423\,\mathrm{Re}_f^{0.99}\,\mathrm{Pr}^{0.21}\left(\frac{\mathrm{Pr}}{\mathrm{Pr}_s}\right)^{0.25}$	Micro	57.05
Metzger et al. [97]	$Nu_f = 0.135\left(\frac{S_L - D_f}{D_f}\right)^{-0.34}\mathrm{Re}_f^{0.69}$	Macro	7.62
Moores and Joshi [98]	$Nu_f = 0.64\left(\frac{h_f}{D_f}\right)^{0.36}\left(\frac{dh + h_f}{h_f}\right)^{-0.57}\mathrm{Re}_f^{0.64}\,\mathrm{Pr}^{0.36}$	Mini	72.56
Prasher et al. [81]	$Nu_f = 0.281\left(\frac{S_L - D_f}{D_f}\right)^{-0.63}\mathrm{Re}_f^{0.73}$	Micro	61.3
Short et al. [99]	$Nu_f = 0.76\left(\frac{S_L}{D_f}\right)^{0.16}\left(\frac{S_t}{D_f}\right)^{0.2}\left(\frac{h_f}{D_f}\right)^{-0.11}\mathrm{Re}_f^{0.33}\,\mathrm{Pr}^{1/3}$	Macro	45.36
Whitaker [100]	$Nu_f = 2\,\mathrm{Re}_f^{1/3}\,\mathrm{Pr}^{1/3}\left(\frac{\mu}{\mu_s}\right)^{0.14}$	Macro	71.8
Zukauskas [93]	$Nu_f = 0.9\,\mathrm{Re}_f^{0.4}\,\mathrm{Pr}^{0.36}\left(\frac{\mathrm{Pr}}{\mathrm{Pr}_s}\right)^{0.25}$	Macro	59.64
Square			
Present Square Correlation [92]	$Nu_f = 0.0937\left(\frac{S_L}{D_f}\right)^{0.2}\left(\frac{S_t}{D_f}\right)^{0.2}\left(\frac{h_f}{D_f}\right)^{0.25}\left(1+\frac{dh}{D_f}\right)^{0.4}\mathrm{Re}_f^{0.6}\,\mathrm{Pr}^{0.36}\left(\frac{\mathrm{Pr}}{\mathrm{Pr}_s}\right)^{0.25}$	Mini	9.34
Liu et al. [101]	$Nu_f = 0.1245\,\mathrm{Re}_f^{0.6106}\,\mathrm{Pr}^{0.36}\left(\frac{\mathrm{Pr}}{\mathrm{Pr}_s}\right)$	Micro	2.1
Liu et al. [101]	$Nu_f = 0.143\,\mathrm{Re}_f^{0.615}\,\mathrm{Pr}^{1/3}$	Micro	8.9
Qu and Siu-Ho [82]	$Nu_f = 0.0241\,\mathrm{Re}_f^{0.953}\,\mathrm{Pr}^{0.36}\left(\frac{\mathrm{Pr}}{\mathrm{Pr}_s}\right)^{0.25}$	Micro	28.76
Qu and Siu-Ho [82]	$Nu_f = 0.0285\,\mathrm{Re}_f^{0.932}\,\mathrm{Pr}^{1/3}$	Micro	29.67
Diamond			
Present Diamond Correlation [92]	$Nu_f = 0.036\left(\frac{S_L}{D_f}\right)^{0.2}\left(\frac{S_t}{D_f}\right)^{0.2}\left(\frac{h_f}{D_f}\right)^{0.25}\left(1+\frac{dh}{D_f}\right)^{0.4}\mathrm{Re}_f^{0.6}\,\mathrm{Pr}^{0.36}\left(\frac{\mathrm{Pr}}{\mathrm{Pr}_s}\right)^{0.25}$	Mini	8.34
Triangle			
Present Triangle Correlation [92]	$Nu_f = 0.0454\left(\frac{S_L}{D_f}\right)^{0.2}\left(\frac{S_t}{D_f}\right)^{0.2}\left(\frac{h_f}{D_f}\right)^{0.25}\left(1+\frac{dh}{D_f}\right)^{0.4}\mathrm{Re}_f^{0.6}\,\mathrm{Pr}^{0.36}\left(\frac{\mathrm{Pr}}{\mathrm{Pr}_s}\right)^{0.25}$	Mini	9.07
Ellipse			
Present Ellipse Correlation [92]	$Nu_f = 0.0936\left(\frac{S_L}{D_f}\right)^{0.2}\left(\frac{S_t}{D_f}\right)^{0.2}\left(\frac{h_f}{D_f}\right)^{0.25}\left(1+\frac{dh}{D_f}\right)^{0.4}\mathrm{Re}_f^{0.6}\,\mathrm{Pr}^{0.36}\left(\frac{\mathrm{Pr}}{\mathrm{Pr}_s}\right)^{0.25}$	Mini	9.32

Reference	Correlations	Scale	MAE
Circle			
Hexagon			
Present Hexagon Correlation [92]	$Nu_f = 0.0752\left(\frac{S_L}{D_f}\right)^{0.2}\left(\frac{S_t}{D_f}\right)^{0.2}\left(\frac{h_f}{D_f}\right)^{0.25}\left(1+\frac{dh}{D_f}\right)^{0.4}\mathrm{Re}_f^{0.6}\,\mathrm{Pr}^{0.36}\left(\frac{\mathrm{Pr}}{\mathrm{Pr}_s}\right)^{0.25}$	Mini	9.47

Table 2.3: MAE Values for Nu Correlations

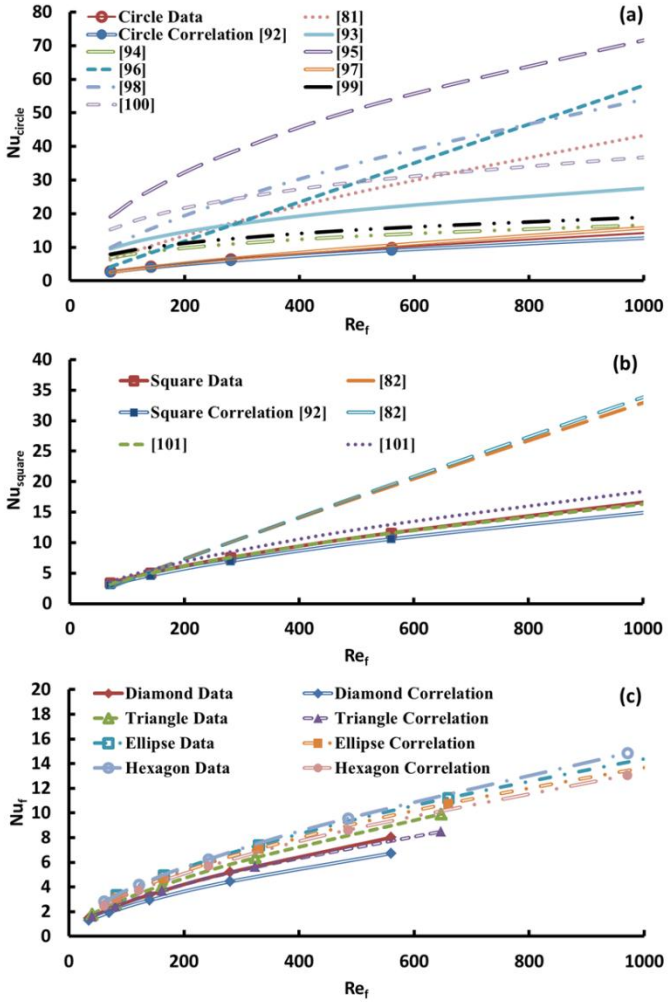

Figure 2.6: Nusselt number, Nu_f, versus Reynolds number, Re_f, for numerical data compared to newly developed and other correlations: a) Using circular shaped pin fin; b) Using square shaped pin fin; c) Using diamond, triangle, ellipse, and hexagonal shaped pin fins

2.3.2. Pressure Drop

Pressure drop across a tube bank can be obtained using the expression in Equation 2.14.

$$\Delta p = N_y f \frac{\rho u_{\max}^2}{2} \qquad 2.14$$

After reviewing many relations from other studies to obtain f, the correlation developed for each shapes are in the form defined by Equation 2.15, used by Short et al. [103]. This expression is defined in terms of many geometrical parameters outlining the staggered formation similar the Nu_f equation in the previous section; therefore, could reflect this data best.

$$f = C_f \left(\frac{S_L}{D_f}\right)^S \left(\frac{S_t}{D_f}\right)^U \left(\frac{h_f}{D_f}\right)^V \left(1+\frac{dh}{D_f}\right)^W \mathrm{Re}_f^X \qquad 2.15$$

$C_f, S, U, V, W,$ and X are all constants determined from the data. This expression incorporates the varying height, the location (S_L and S_t) of the fins within the staggered array and the clearance above the fins for the fluid to flow. The exponents for each shape are constant with only a different C_f and are shown in the next equation.

$$f = C_f \left(\frac{S_L}{D_f}\right)^{0.2} \left(\frac{S_t}{D_f}\right)^{0.2} \left(\frac{h_f}{D_f}\right)^{0.18} \left(1+\frac{dh}{D_f}\right)^{0.2} \mathrm{Re}_f^{-0.435} \qquad 2.16$$

For

Geometry	Circle	Square	Diamond	Triangle	Ellipse	Hexagon
C_f	2.96	5.28	1.81	2.45	3.44	4.53

Re_f is determined based on the hydraulic diameters of the fins and the maximum velocity, $u_{\max}$, flowing through the fins. This expression is effective for Re_f in the laminar regime.

Table 2.4 compares the MAE values for the correlations of *f* developed for each shape with other existing correlations. Each of the correlations developed have a MAE less than 10 for all shapes which displayed better values than the others. The expression developed by Prasher et al. [81] showed the next closest in determining the numerical data with an MAE value of 16.93 and the next Liu et al. [101] and Qu and Siu-Ho [83] with about 40. This is shown in Figure 2.7. It seems as the MAE values closer resemble expressions developed for microchannels vs. conventional scaled channels with fins.

Reference	**Correlations**	**Scale**	**MAE**
Circle			
Present Circle Correlation [92]	$f = 2.963\left(\frac{S_L}{D_f}\right)^{0.2}\left(\frac{S_t}{D_f}\right)^{0.2}\left(\frac{h_f}{D_f}\right)^{0.18}\left(1+\frac{dh}{D_f}\right)^{0.2}\mathrm{Re}_f^{-0.435}$	Mini	7.06
Armstrong & Winstanley [104]	$f = 2.06\left(\frac{S_t}{D_f}\right)^{-1.1}\mathrm{Re}_f^{-0.16}$	Macro	29.35
Chilton & Generaux [105]	$f = \frac{106}{\mathrm{Re}_f}$	Macro	54.47
Gaddis and Gnielski [106]	$f = 280\pi\left(\left(\left(\frac{S_L}{D_f}\right)^{0.5} - 0.6\right)^2 + 0.75\right)\Big/\mathrm{Re}_f\left(4\frac{S_L S_t}{D_f^2} - \pi\right)C^{1.6}$ $C = \frac{S_t}{D_f}$ for $\frac{S_L}{D_f} \geq \frac{1}{2}\sqrt{2\frac{S_t}{D_f}+1}$ $C = \frac{S_D}{D_f}$ for $\frac{S_L}{D_f} < \frac{1}{2}\sqrt{2\frac{S_t}{D_f}+1}$	Macro	279.5

Reference	Correlations	Scale	MAE
Circle			
Gunther & Shaw [107]	$f = \frac{180}{\mathrm{Re}_f}\left(\frac{4S_tS_L}{\pi D_f^2}-1\right)^{0.4}\left(\frac{S_L}{S_t}\right)^{0.6}$	Macro	64.22
Kast [108]	$f = \left(\frac{128}{\mathrm{Re}_f}+\frac{4}{\mathrm{Re}_f^{0.16}}\right)$	Macro	85.87
Kosar et al. [86]	$f = \pi_1+\pi_2$ $\pi_1 = \frac{1739}{\mathrm{Re}_f^{1.7}}\left(\frac{h_f/D_f}{h_f/D_f+1}\right)^{1.1}\left(\frac{S_tS_L}{A_f}\right)^{-0.3}$ $\pi_1 = \frac{345}{\mathrm{Re}^{1}}\left(\frac{1}{h_f/D_f+1}\right)^{2.0}\left(\frac{S_tS_L}{A_f}\right)^{-0.3}$	Micro	60.33
Moores and Joshi [98]	$f = 19.04\left(\frac{h_f}{D_f}\right)^{-0.742}\left(\frac{dh+h_c}{h_c}\right)^{0.505}\mathrm{Re}_f^{-0.502}$	Mini	87.87
Moores et al. [109]	$f = 10.52k_1\left(\frac{h_f}{D_f}\right)^{0.28+(1-k_1)}\mathrm{Re}_f^{-0.39+(1-k_2)}$ $k_1 = \exp^{4.3(dh/h_f)}$ $k_2 = \exp^{0.8(dh/h_f)}$	Mini	70.98
Prasher et al. [81]	$f = 3.5\left(\frac{h_f}{D_f}\right)^{0.724}\left(\frac{S_L-D_f}{D_f}\right)^{-0.442}\left(\frac{S_t-D_f}{D_f}\right)^{-0.245}\mathrm{Re}_f^{-0.58}$	Micro	16.93
Short et al. [103]	$f = 140.4\left(\frac{S_L}{D_f}\right)^{-1.3}\left(\frac{S_t}{D_f}\right)^{-0.78}\left(\frac{h_f}{D_f}\right)^{-0.55}\mathrm{Re}_f^{-0.65}$	Macro	72.43
Square			
Present Square Correlation [92]	$f = 5.28\left(\frac{S_L}{D_f}\right)^{0.2}\left(\frac{S_t}{D_f}\right)^{0.2}\left(\frac{h_f}{D_f}\right)^{0.18}\left(1+\frac{dh}{D_f}\right)^{0.2}\mathrm{Re}_f^{-0.435}$	Mini	6.82
Konishi et al. [110]	$f = 10.485\,\mathrm{Re}_f^{-0.35}$	Micro	63.94
Konishi et al. [111]	$f = \frac{55.631}{\mathrm{Re}_f}+\frac{2.1114}{\mathrm{Re}_f^{0.09597}}$	Micro	62.61
Liu et al. [101]	$f = 1.6361\,\mathrm{Re}_c^{-0.01076}E^{-0.94496}$ $E = \frac{2S_t}{W_c/\sin(45°)}$	Micro	39.12
Qu and Siu-Ho [82]	$f = 20.09\,\mathrm{Re}_f^{-0.547}$	Micro	37.7
Diamond			
Present Diamond Correlation [92]	$f = 1.81\left(\frac{S_L}{D_f}\right)^{0.2}\left(\frac{S_t}{D_f}\right)^{0.2}\left(\frac{h_f}{D_f}\right)^{0.18}\left(1+\frac{dh}{D_f}\right)^{0.2}\mathrm{Re}_f^{-0.435}$	Mini	6.67

Reference	Correlations	Scale	MAE
Circle			
Kosar et al. [86]	$f = \pi_1 + \pi_2$ $\pi_1 = \frac{1126}{\mathrm{Re}_f^{1.1}}\left(\frac{h_f/D_f}{h_f/D_f+1}\right)^{1.5}\left(\frac{S_t S_L}{A_f}\right)^{-0.4}$ $\pi_1 = \frac{6.6}{\mathrm{Re}^{1}}\left(\frac{1}{h_f/D_f+1}\right)^{1.7}\left(\frac{S_t S_L}{A_f}\right)^{-1}$	Micro	64.78
Triangle			
Present Triangle Correlation [92]	$f = 2.45\left(\frac{S_L}{D_f}\right)^{0.2}\left(\frac{S_t}{D_f}\right)^{0.2}\left(\frac{h_f}{D_f}\right)^{0.18}\left(1+\frac{dh}{D_f}\right)^{0.2}\mathrm{Re}_f^{-0.435}$	Mini	5.98
Ellipse			
Present Ellipse Correlation [92]	$f = 3.44\left(\frac{S_L}{D_f}\right)^{0.2}\left(\frac{S_t}{D_f}\right)^{0.2}\left(\frac{h_f}{D_f}\right)^{0.18}\left(1+\frac{dh}{D_f}\right)^{0.2}\mathrm{Re}_f^{-0.435}$	Mini	6.62
Hexagon			
Present Hexagon Correlation [92]	$f = 4.53\left(\frac{S_L}{D_f}\right)^{0.2}\left(\frac{S_t}{D_f}\right)^{0.2}\left(\frac{h_f}{D_f}\right)^{0.18}\left(1+\frac{dh}{D_f}\right)^{0.2}\mathrm{Re}_f^{-0.435}$	Mini	9.39

Table 2.4: MAE Values for f Correlations

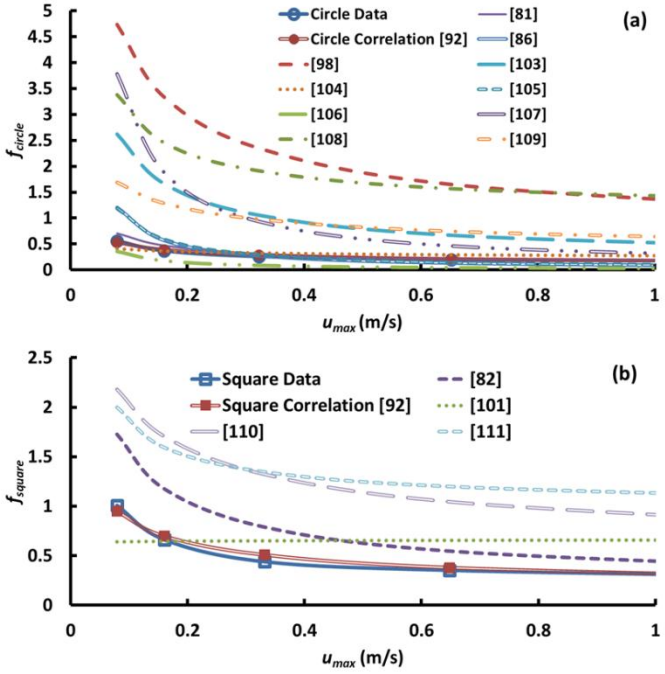

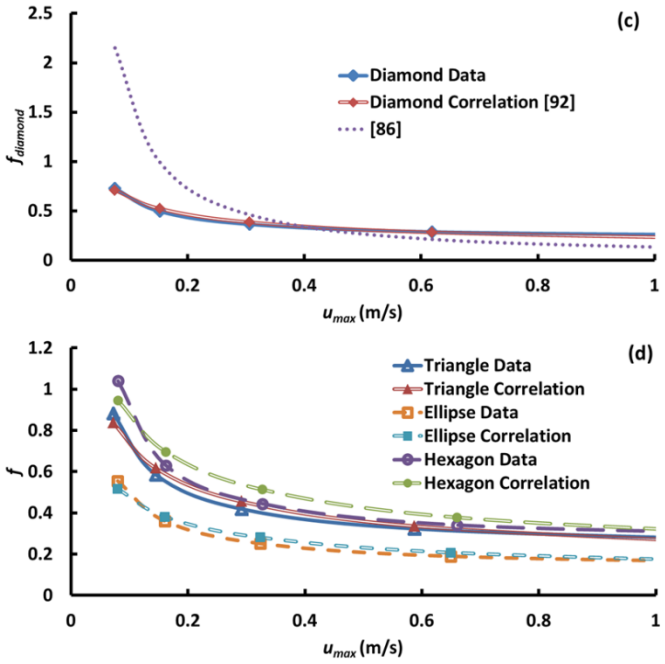

Figure 2.7: Pressure drop, Δp, versus maximum axial velocity, u_{max}, for numerical data compared to newly developed and other correlations: a) Using circular shaped pin fin; b) Using square shaped pin fin; c) Using diamond shaped pin fins; d) Using triangle, ellipse, and hexagonal shaped pin fins

2.4. Validation of Correlations

To validate the new correlations, experimental results taken from work completed by Liu et al. [101] for a heat sink containing 625 square micro pin fins of 445 x 445 μm^2 in a staggered array was solved with water used as the working fluid flowing with Re ranging from 60 to 800. The fins and channel have a height of 3 mm. The longitudal and transverse spacing of the fin measured 565.7 μm. The ambient fluid temperature is initally at room temperature and heat is applied to the bottom surface. The geometry of the fins fit the limits of the new equations developed and the Nusselt number, Nu_f, and pressure drop, Δp, across the finned

structure were calculated using new correlations and compared to the experimental data. This is shown in Figure 2.8. Based on the example, both correlations developed for Nu_f and f are similar to that of the value obtained in the experimental work within 15%. This proves that the new expression for the Nu_f can accurately predict the heat transfer through the channel with micro pin fins on the surface. These correlations obtained can provide suitable values for the pressure drop and the Nu_f across a staggered finned array.

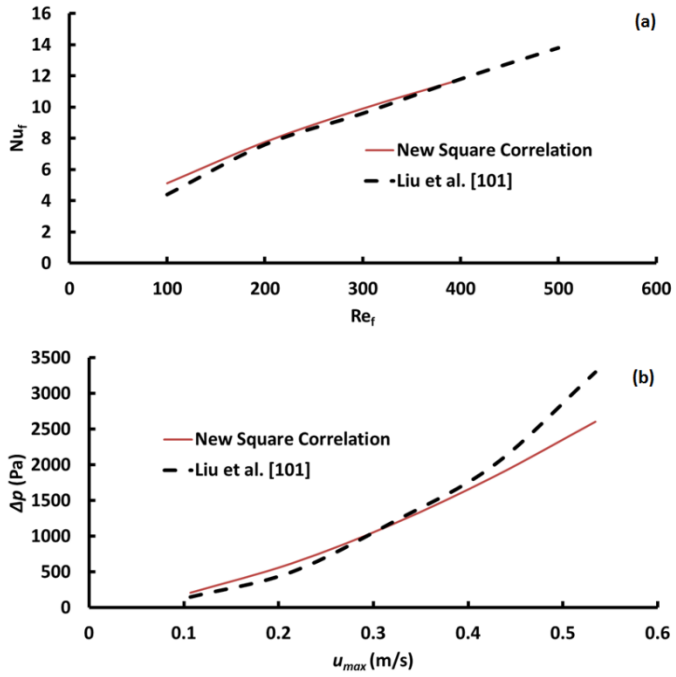

Figure 2.8: Numerical validation of the new correlations with the experimental data of Liu et al. [101]: a) Nusselt number, Nu_f, versus Reynolds number, Re_f; b) Pressure drop, Δp, versus maximum axial velocity, u_{max}

2.5. In Summary

An optimization study was completed in order to understand the effects of micro fins on the surface of a minichannel to obtain maximum thermal performance. From previous studies, use of microstructures on the surfaces of micro/minichannels has been effective with increased heat removal from a heated surface. Four parametric studies have been conducted in order to optimize the fins: 1) using different geometrical shaped fins – circle, square, triangle, ellipse, diamond, and hexagon placed on the bottom surface of a minichannel in a staggered formation, 2) varying fin to channel height ratio in a square pin fin geometry formation, 3) varying fin width and spacing, and 4) defining square pin fins as CNTs, silicon, copper, and aluminum. In addition to those studies, Nusselt number and Darcy friction factor correlations were then obtained to fit our data and compared to previous studies. This work was completed by varying inputted velocities and constant heat fluxes while keeping the fluid in the single phase, laminar flow regime. The following conclusions can be drawn from the results:

- Fin shapes yield Nu values within 37% of each other at high Re with the triangle fins as the highest and the circle and ellipse fins lower; however, the pressure drop values are greatly affected. The ellipse and circle fin portray the smallest pressure drop value because of its aerodynamic shape with the lowest Nu values larger than 45% when compared to the unfinned channel.

- With increasing fin height the Nu increases; however, the pressure drop also increases drastically. From the lowest tested fin height to channel ratio to the

highest, the difference in Nu is 44% and the pressure drop differential at higher Re is almost 7.4 kPa. Fin height to channel height ratio should be determined based on the maximum pressure drop allowed for the pump used.

- With decreasing fin width and spacing the Nu increases; however, the increase in pressure drop is significant. For fin width at 0.5 mm there was an increase in performance is 88% higher than that of the unfinned channel and about 38% higher Nu values to the larger fin width and spacing. Pressure drop increased significantly with a 15% increase to the unfinned channel.

- In keeping the fin width and the number of fins constant, the fins spacing was varied. The results showed that allowing for the maximum spacing, or the spacing equal to the fin width, the thermal performance is better by 6% with minimal pressure drop of about 5%.

- Fin material shows little effect on fin performance; however, fins with CNTs are not modeled as a porous media which is expected to increase the surface area that the fluid interacts with and can hasten nucleate boiling onset which could increase heat transfer performance significantly. Therefore the thermal performance for the CNT fins is under predicted.

- Empirical expressions for both Nu_f and f were provided and validated for all six shapes and compared to other existing correlations. The expressions were curve fit to the data obtained and when creating these expressions, the only value that varied between the different shapes was the constant.

More intensive studies need to be conducted in accurately modeling CNTs as the porous media. Triangular fins with larger fin height, smaller fin width, and spacing double the fin width maximizes the number of fins in each row and yields better performance. The digital revolution is upon us, but without significant gains in nano/micro/mini heat transfer technology, the new advancements will be unattainable. Chapter 3 experimentally examines the use of micro pin fins on the surface of a minichannel using both water and Al_2O_3/H_2O nanofluid as the working fluid.

Chapter 3

Effect of Al_2O_3/H_2O Nanofluid on MWNT Circular Fin Structures in a Minichannel

As described in the previous two chapters, minichannels and microchannels provide an effective way of cooling small surfaces because of their ability to dissipate high surface temperatures through convection. Nano-, micro-, and minichannels have a higher heat transfer surface area to fluid volume ratio than a conventional channel which enhances convection. The heat transfer coefficient increases as the channel's hydraulic diameter is reduced, enabling an excellent cooling apparatus. Although it has excellent cooling capabilities, these channels experience a high pressure drop across the channel. Several surface modifications proven to enhance the thermal performance even further includes varying the shape of the channel [112], oscillating the channels dimensions into a wavy channel

[113,114], an increased surface roughness [8,65], applying small cavities on the channel walls [7,10,11,66,67], and adding pin fins to increase surface area [7,75,79,80,86,91,92]. Applying defects to the surfaces of the channel can increase mixing of the flow, improve wettability of the surface, and initiate nucleate boiling sooner allowing more heat to be carried away from the heated surface [69].

Because of carbon nanotubes (CNTs) excellent physical and thermal properties, many researchers have grown them on the surfaces of microchannels to act as fins. Flow boiling analysis of CNTs coated microchannels and water as the working fluid was conducted by [115–117]. In all cases there was an improvement of the critical heat flux due to the increased nucleation cites provided by the CNTs. Others investigated single phase flow using MWNTs on the surfaces of microchannels. Mo et al. [21] applied different heat rates to a silicon base channel and kept the pressure drop across the device constant. This work obtained up to a 23% higher input power while keeping the temperature of the transistor below a silicon microchannel containing no CNTs. Jakobski et al. [89] also applied CNTs to a silicon microchannel and obtained an increase in thermal performance. Shenoy et al. [90] investigated the effects of water flowing past two devices- one of a fully coated carpet of MWNTs on the surface and another of circular MWNT micro pin fins in a staggered array - and compared them to a bare minichannel. The results further validated the enhancement of the thermal performance of MWNTs and was able to obtain a higher inputted heat flux for a finned channel vs. both the bare channel and the fully carpeted channel with only a slight pressure drop at a given temperature

and two different flow rates. CNT fins have shown to be effective in increasing microchannel thermal performance.

The working fluid predominantly used through heat exchanger studies is water; however, other fluids such as dielectrics and nanofluids are also used. Dielectric fluids have a low boiling point and increases wetting properties to provide improved heat transfer in single phase flow but they undergo dry out and reverse flow problems [118–120]. Nanofluids are made up of small nanosized particles usually no bigger than 100 nm in size suspended in a base fluid such as water, ethylene glycol, engine oil, or refrigerant. These added nanoparticles have been found to increase thermo-physical properties such as thermal conductivity, thermal diffusivity, viscosity, and convection heat transfer compared to their base fluids [121]. Previous studies have investigated the parameters that can influence the thermal performance of nanofluids, specifically Al_2O_3. Parameters such as particle size [122,123], concentration [30,122,124,125], and the effect of fluid properties [126–128] have all been examined. A review of the effects of these parameters for Al_2O_3/H_2O based nanofluids is given in [129]. As the nanoparticle diameter is reduced (< 5 nm), the effective thermal conductivity increases which significantly enhances the thermal conductivity. As particle diameter approaches the micron size, they do not remain suspended within the base fluid. These particles no longer have those chaotic, Brownian motion reducing the enhancement of the suspended particles. For flow boiling studies, increased concentration of nanoparticles provides enhanced critical heat flux and the wettability of the fluid is increased. This is mainly

due to the surface defects created by the sedimentation and agglomeration of the nanoparticles as it reaches higher temperatures [121]. With increased volume concentration more sedimentation is left on the surface of the channel which increases the surface roughness [130,131] and the heat transfer coefficient. When further investigating the volume concentration, it seems that viscosity is not affected for concentrations below 1%. However, for viscosity at higher volume concentrations, a large increase is observed when a fluid sample is heated beyond a critical temperature. When it is cooled before it reaches the critical point, the viscosity remains very similar of that to water. This is known as the hysteresis phenomenon among researchers. Nanofluids can leave sedimentation of particles, fouling, erosion, and may even clog the channel over time [35]. Based on the literature, the effects of nanofluids can increase the thermal performance of a base channel and is affected by particle size and concentration.

Nanofluids are still an enigma to the world today. Some say the effects of enhancement of nanofluids are caused by the Brownian motion of the nanoparticle and or thermophoresis or thermal diffusion of the system. Brownian motion is the random drifting of particles suspended in a fluid and thermal diffusion is the mass flux induced by a thermal gradient [132–135]. Others claim the main reason for their ability to remove a vast amount of heat is due to the surface deficiencies created at high temperatures due to particle deposition [121]. Added surface roughness shows as a promising reason for enhanced heat transfer. Few researchers have investigated the use of both nanofluids and mechanically induced surface

structures. Zhou [136] passed silver nanofluids of different volume concentrations suspended into a PVP solution through an array of drop shaped micro pin fins in a microchannel. About an 18% increase in performance was obtained compared to a base fluid with little difference in the pressure drop.

The chapter presents the work conducted by Tullius et al. [137,138]. In this paper, they consider two modes of enhancements - the use of micro pin fins and the use of nanofluids - to improve cooling to help understand if the main source of thermal enhancement in nanofluids is surface defects. A volume concentration of 0.01% of Al_2O_3 suspended in water flows through a minichannel at a rate of 80 mL/min with MWNTs grown on the bottom surface in a fully coated structure and a staggered array of circular micro pin fins. This is compared to a channel with no MWNTs. Because of sedimentation on the surface that occurs at higher temperatures, the experiments are conducted multiple times to understand the extended performance after nanoparticles collect on the channel surface for each device. Although two phase flows provide higher heat transfer when comparing to single phase flows and are ample for higher heat flux cases, this study focuses on the single phase flow and the nucleation phase of nanofluid through a minichannel coated with MWNTs on the surface.

3.1. Device Fabrication

Three devices were fabricated and used for this experiment - 1) no MWNTs on the surface, 2) fully covered MWNTs on the surface, and 3) a 6 x 12 staggered

array (6 rows and 12 columns) of circular fins made up of MWNTs. Figure 3.1 is the device fabrication of the channels and their dimensions. A 1 mm thick silicon wafer, pre-coated with 500 nm of silicon dioxide, is sliced into a 55 x 45 mm^2 rectangular plate. An octagonal hole is laser cut in the center of this piece where the widest and longest part of the channel is 25 mm and 35 mm, respectively. This silicon wafer piece is then bonded using thermal epoxy onto a 500 μm thick wafer of similar dimensions. To enclose the channel, a 1 mm thick Pyrex wafer with two drilled holes 1 mm in diameter and 31 mm apart at the center of the wafer is bonded also using thermal epoxy to the other side of the silicon wafer with the octagonal hole. Capillary tubing of 1 mm inner diameter is used then to form the inlet and outlet manifolds. This process is used for all the devices; however, for the channels with MWNTs, extra steps were taken. The MWNTs were grown using chemical vapor deposition at 775°C with a ferrocene catalyst and a xylene source with a mixture of argon and hydrogen as the carrier gas. MWNTs are a dense entangled network of tubes with a broad diameter distribution of 10 - 100 nm. For the fully covered MWNT device, nanotubes, 500 μm in height, were grown at the center of the silicon wafer in a rectangular area of 24 x 15 mm^2. The 6 x 12 MWNT fins were developed from a fully carpeted rectangular mesh and then laser cut to the desired fin formation. These circular micro fins are staggered in nature with a diameter of 1 mm and a height of 500 μm. Figure 3.2 shows an image of a section of these micro pin fins.

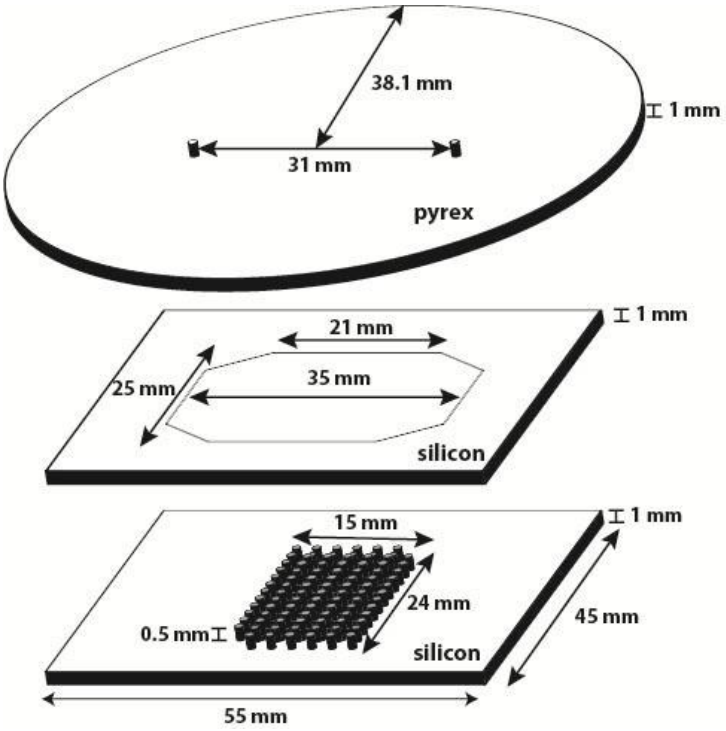

Figure 3.1: The minichannel assembly with appropriate dimensions

Figure 3.2: Image of some of the MWNT fins in a staggered array

3.2. Nanofluid Preparation

Sigma Aldrich's Al_2O_3 nanopowder was deposited into deionized water to make a volume concentration of 0.01% with particle diameters less than 50 nm. It was then placed in a sonicating water bath for 30 minutes. It was found that this

amount of time was adequate for the particles to be completely dispersed within the water and no residue was left on the glass beaker. It was made in 1.4 L increments until the desired amount of fluid was obtained. Because no surfactant was used to prolong the stability of the fluid, a second batch of nanofluid was made during the duration of the experimentation to ensure the integrity of the fluid had not deteriorated and thermal performance obtained throughout the experiment was accurate.

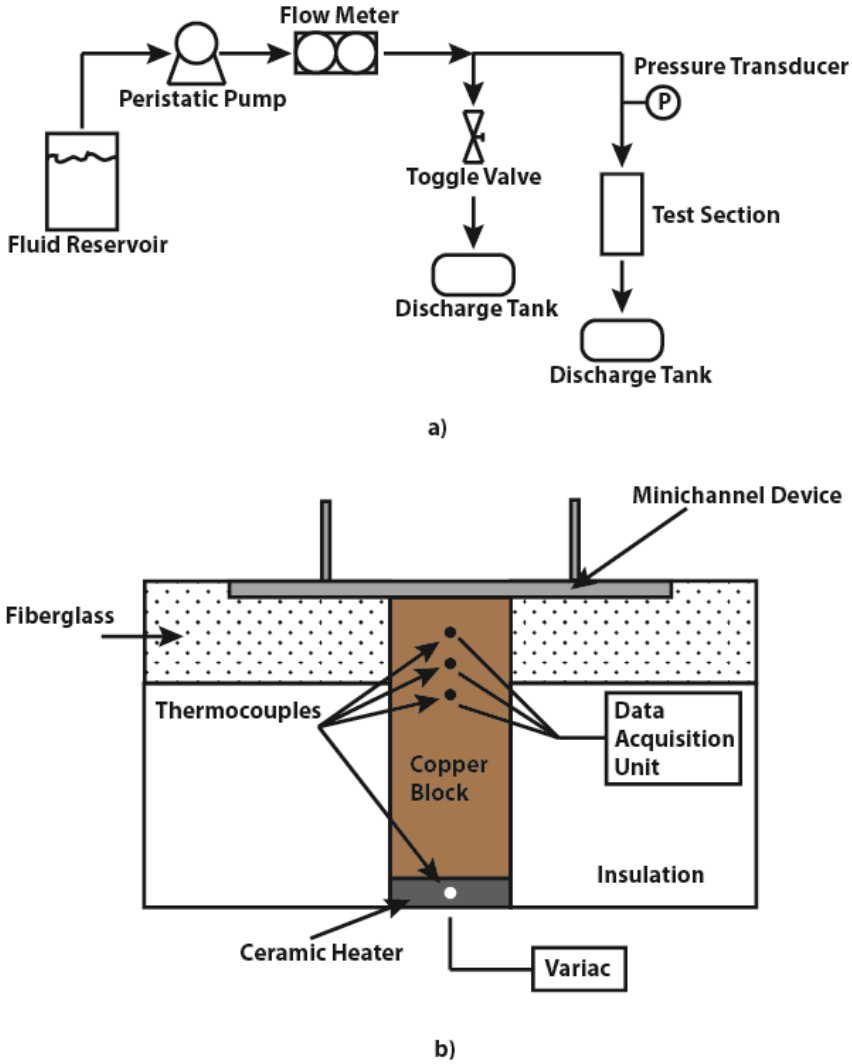

Figure 3.3: Schematics of open flow loop and testing device

3.3. Experimental Setup

The experimental setup is an open flow system in which Al_2O_3 nanofluid is driven with a peristaltic pump through a rotameter flow meter that measures the volumetric flow rate. The pump consists of a pump head and a drive to control the flow rate. The fluid then passes through the testing device and is finally collected into an open vessel. A toggle valve is added to the system to help relieve the pressure build up in the flow loop. A differential pressure transducer is also added to the setup to obtain the pressure reading across the system. Because this is an open looped system, one port of the transducer is connected to the inlet of the channel and the other is open to the atmosphere. Figure 3.3a shows the schematic of the flow loop for the system.

A profile of the testing device is shown in Figure 3.3b. The minichannel assembly is held by a fiberglass block. This fiber glass has a 55 x 45 mm^2 rectangular recess to anchor the device and in the middle of the recess is a 25 x 15 mm^2 rectangular hole to house a copper block. A ceramic heater controlled by a variac is placed on the bottom of the copper block to heat the system. The heat travels from the heater through the copper block and up into the bottom surface of the minichannel. A thin layer of thermal interface material is applied between the copper block and the silicon surface to achieve good thermal contact. In addition to the thermal interface material, in order to provide maximum thermal contact, mechanical clamping was used. The copper block is well insulated to prevent too much heat loss. Three holes are drilled into the copper block to house 30 gauge type

T thermocouples. Using a thermal epoxy, the thermocouples are secured to the copper block and are used to measure the heat flux applied to the device using Fourier's law of conduction shown in Equation 3.1,

$$q = k\frac{\Delta T}{\Delta x}\ , \tag{3.1}$$

where k is the thermal conductivity of the copper block, Δx is the distance between the thermocouples, and ΔT is the difference between the thermocouple temperatures. The reading from the top most thermocouple closest to the silicon surface is assumed to be the base temperature of the system. The temperature of the heater is monitored through an inbuilt thermocouple. The data is recorded using a measurement computing data acquisition unit (DAQ) and Lab View.

3.4. Data Reduction and Uncertainty

Uncertainties in measured quantities are 6% for the rotameter, 0.1 °C for the thermocouples, and 7% for the pressure transducer. Heat loss is determined using similar relations to Shenoy et al. work [90] based on computational modeling for a similar minichannel with no MWNTs at different flow rates. The heat loss relations are used to adjust the measured heat flux thus giving the heat flux applied to the base for the three different devices. The Kline and Mclintock method [139] is used to determine the uncertainty associated with the heat flux applied to the base. The heat flux had an uncertainty range of 3.6 - 17% where the uncertainties are higher at lower heat fluxes.

3.5. Experimental Validation

Before this experiment was conducted using nanofluid, it was performed using water and compared to the results obtained by Shenoy et al. [90]. This is to ensure that the DAQ adequately measured the temperature values of the system, and thorough contact between the copper block and the silicon surface was made. The results from the three channels- no MWNTs, fully coated MWNTs, and finned MWNTs - and the results from [90] are shown in Figure 3.4a. As shown in the figure, the results match verifying the experimental setup is correct and the thermocouples are accurately measuring the temperature and heat fluxes within the system.

To verify the energy balance within the experiment using Al_2O_3/H_2O nanofluid, the data was compared with the predicted results using the energy balance equation given in Equation 3.2. Figure 3.4b shows the measured and analytical fluid temperature rise.

$$Q = \rho_{nf} \dot{V} c_{p,nf} \left(T_{out} - T_{in} \right). \tag{3.2}$$

Q is the heat applied to the system, $\dot{V}$ is the volumetric flow rate, and T_{in} and T_{out} are the inlet and outlet temperature measured across the channel. The nanofluid density, ρ_{nf}, and specific heat of constant pressure, $c_{p,nf}$, were calculated based on Equations 3.3 and 3.4 taken from [140] where ϕ is the volumetric concentration of the particles in the nanofluid which in this case is $\phi = 0.01$.

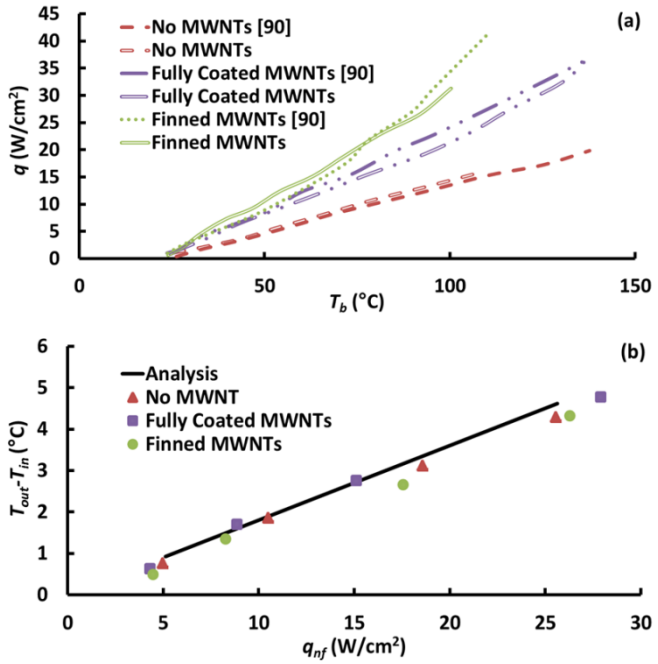

Figure 3.4: Validation: a) A comparison to [90] and this work using water as the working fluid; b) Comparison of the applied heat flux vs. the temperature difference at the inlet and outlet to the energy equation using Al_2O_3/H_2O nanofluid

$$\rho_{nf} = (1-\phi)\rho_{H_2O} + \phi\rho_{Al_2O_3} \tag{3.3}$$

$$(\rho c_p)_{nf} = (1-\phi)(\rho c_p)_{H_2O} + \phi(\rho c_p)_{Al_2O_3} \tag{3.4}$$

The fluid properties of water, Al_2O_3 particles, and Al_2O_3/H_2O nanofluid are given in Table 3.1. The effective thermal conductivity of the nanofluid is obtained by Maxwell's theory [141]

$$\frac{k_{nf}}{k_{H_2O}} = \frac{k_{Al_2O_3} + 2k_{H_2O} - 2\phi\left(k_{H_2O} - k_{Al_2O_3}\right)}{k_{Al_2O_3} + 2k_{H_2O} + \phi\left(k_{H_2O} - k_{Al_2O_3}\right)}. \tag{3.5}$$

The heat flux ranges considered were those that keep the fluid at single phase. For 80 mL/min, the measured water temperature rise and the predicted water temperature rise are reasonably close proving the validity of the heat loss calculations obtained by Shenoy et al. [90].

	k (W/mK)	c_p (J/kgK)	ρ (kg/m^3)
H2O	0.603	4182	998.2
Al2O3	40	765	3970
Al2O3/H2O Nanofluid (ϕ=0.01%)	0.620	4050.1	1027.9

Table 3.1: Thermo Physical Properties at 293 K

3.6. Results and Discussion

3.6.1. Pressure Drop Analysis

Table 3.2 shows the values of the pressure drop obtained in the nanofluid experiment and those using pure de-ionized water for each device as the fluid remains in the single phase regime flowing at 80 mL/min. The pressure drop measured within our system setup is the addition of pressure drops across the channel, Δp_{ch}, the norprene tubing, Δp_n, the inlet and outlet manifolds, Δp_m, and the pressure drop due to contraction, Δp_c, and expansion, Δp_e, as the water enters through different tubing sizes. Therefore the predicted pressure drop was determined by

$$\Delta p = \Delta p_{ch} + \Delta p_n + \Delta p_m + \Delta p_c + \Delta p_e . \qquad 3.6$$

The pressure drop due to contraction is the fluid as it flows from the larger norprene tubing into the inlet manifold tubing and the pressure drop due to expansion is the fluid as it flows from the outlet manifold into the norprene tubing.

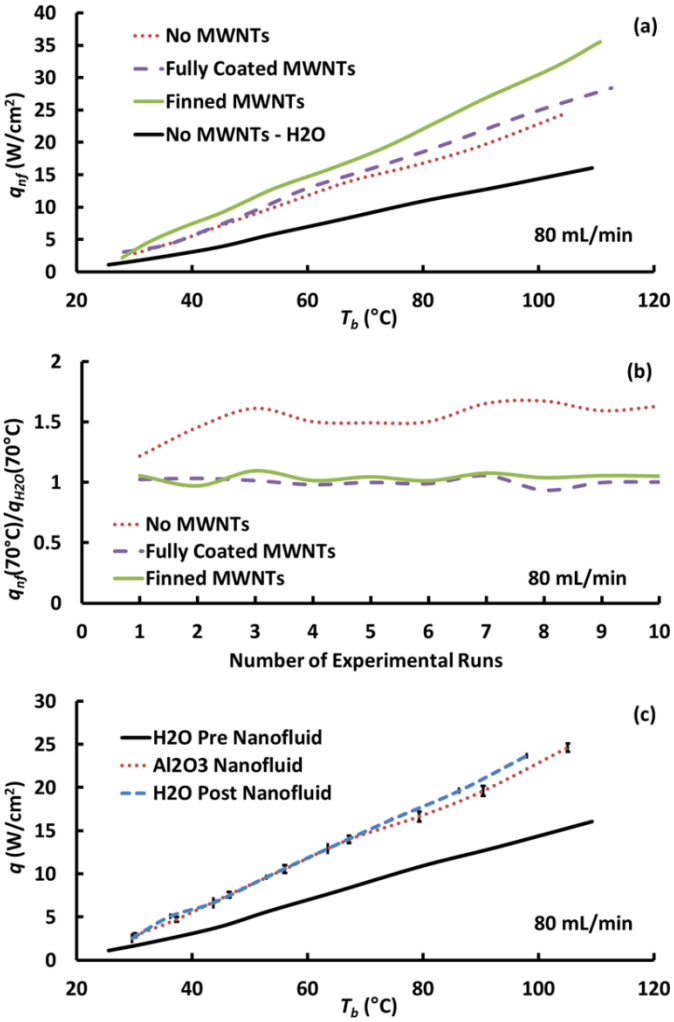

Figure 3.5: Experimental results: a) Heat flux applied at different silicon base temperatures using nanofluid; b) Performance curve of the number of trials conducted for each device; c) Heat flux applied to the base at different silicon base temperatures using both water and nanofluid (black solid line is base performance for experiment ran with the channel with no MWNTs and water)

The pressure drop obtained using the nanofluid for each channel show little to no increase with the addition of nanoparticles. This could be due to the low concentration added to the fluid only changing the properties slightly. Similar to the results for water, the fully covered MWNTs device caused higher pressure drops when compared to the no MWNTs and MWNT finned devices. This is due to the difference in hydraulic diameters created by the protruding MWNTs on the surface.

Device	Δp (kPa)	
	H_2O	Al_2O_3/H_2O Nanofluid
No MWNTs	7.9	8.05
Fully Coated MWNTs	9	9.4
Finned MWNTs	8.05	8.2

Table 3.2: Pressure Drop @ 80 mL/min

3.6.2. Heat Transfer Analysis

The experimental results of the heat flux applied to the minichannel base versus the silicon base temperature obtained for the three different devices are shown in Figure 3.5a. The graph shows the data for both the single and nucleation phases that the fluid partakes in for the given power inputs. For the same inlet velocity, the devices with the MWNTs perform better than the device with no MWNT in both regimes. Similar to the results by [90], for the finned device and the fully covered device, the surface area is much higher than the device with no MWNTs, therefore more heat is removed. The saturation temperature is achieved at higher heat fluxes before nucleation initiates. For a given base temperature of 70°C, the temperature at which visible boiling starts to occur, the no MWNT device has an increase of about 58% using 0.01% volume concentration of Al_2O_3 nanofluid with

respect to the same device using de-ionized water. The fully covered and finned MWNTs devices had increases of 84% and 136%, respectively, for the same base temperature compared to the channel with no MWNTs using de-ionized water. These values correspond to the curves in Figure 3.5a are presented in Table 3.3.

Device	q(W/cm^2)	% Increase
H_2O		
No MWNTs	8.4	---
Al_2O_3/H_2O Nanofluid		
No MWNTs	13.3	58
Fully Coated MWNTs	15.4	84
Finned MWNTs	19.8	136

Table 3.3: Heat Transfer Results for T=70°C

Due to sedimentation of nanoparticles at high temperatures on the channel surface, the performance of the nanofluid was investigated. Each channel was conducted 10 times and data was collected for the fluid rate of 80 mL/min. A ratio of the applied heat fluxes using nanofluid of a given device versus the applied heat flux when using water for the same device at a base temperature of 70°C was used to measure the performance. When the base temperature approached 70°C, nucleation initiated on the surface as observed during the experiment. This is shown in Figure 3.5b. A noticeable increase in performance was observed for the 2nd and 3rd trial in the channel with no MWNTs until its peak performance was obtained. The first experimental run had an increase of about 22% with respect to a channel using water only. The second experimental run enhanced further with a 46% increase with respect to the data using water. Only after the third run did it peak with no loss in performance in the remaining runs with a 58% increase with respect to the water data. A film of nanoparticles could be seen faintly on the surface of the silicon

channel where the heat was applied. This is believed to have occurred due to the increase in sedimentation on the surface creating nucleation sites and enhanced wettability. There was no distinct increase in performance with either channel containing MWNTs. These channels already had surface defects in the form of MWNTs, therefore, only a slight increase was observed probably due to the presence of the Brownian motion and nanoconvection that the nanoparticles partake in. Figure 3.6 shows scanning electron microscope (SEM) images of channel surface for all three channels at different magnifications. Figure 3.6a shows the Al_2O_3 particles on the silicon surfaces. Figure 3.6b shows the nanoparticle agglomeration on the entangled network of MWNTs. Figure 3.6c shows a lower magnification of the Al_2O_3 deposited on both the silicon surface and the MWNT fin.

After all the experiments with nanofluids were completed, the base channel without MWNTs was tested using just deionized water. This was conducted to show that the surface structure had changed enough to achieve improved performance. From these results shown in Figure 3.5c, the data for the fluid using water after the deposits of nanoparticles on the surface were similar to the data obtained using nanofluid. This further confirms that at for Al_2O_3/H_2O nanofluid at a concentration of 0.01%, the major contribution for removing heat is the increased surface roughness with minimal influence on Brownian motion and thermal diffusion that the suspended nanoparticles partake in within the base fluid.

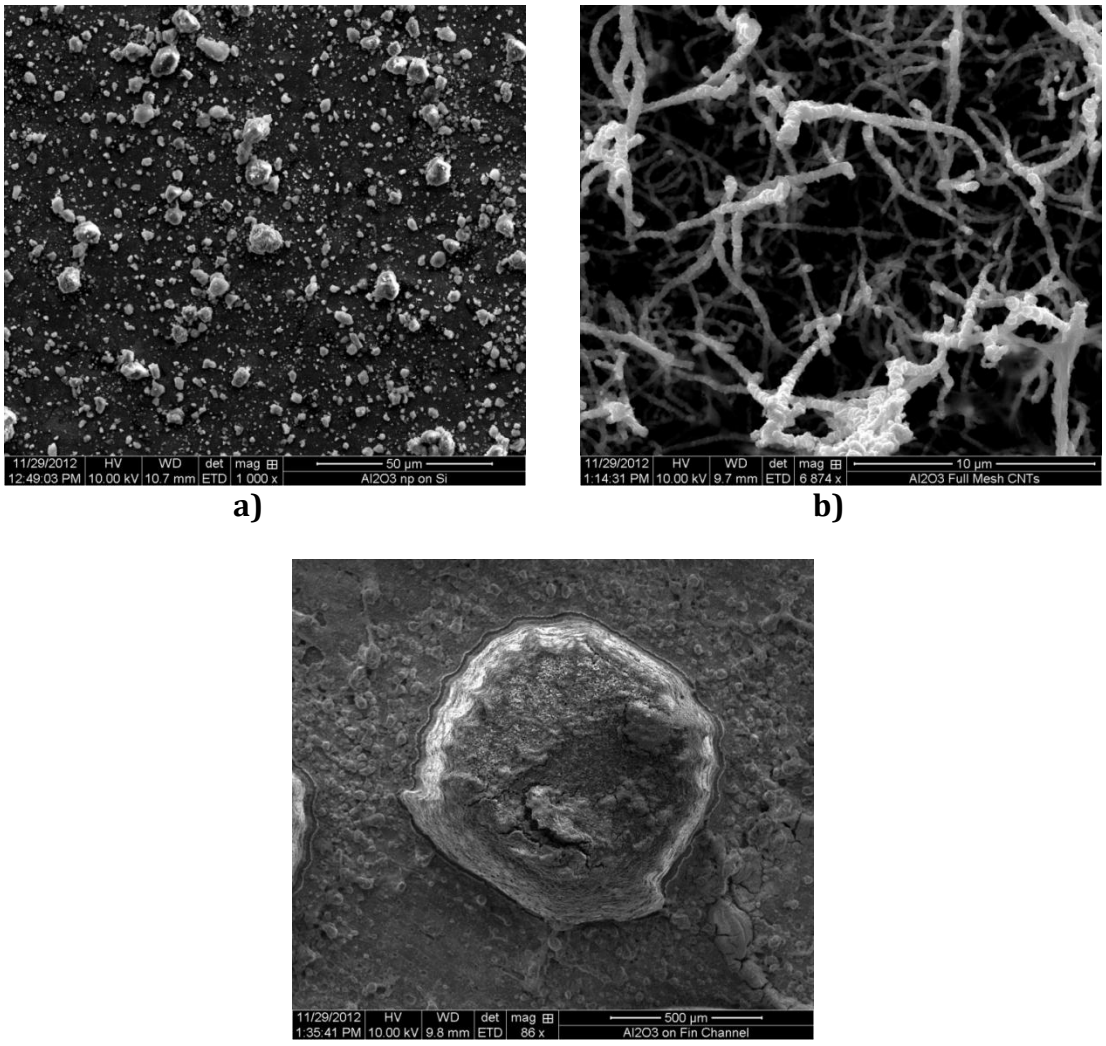

Figure 3.6: SEM images: a) Al_2O_3 particle sedimentation on the silicon surface of the channel with No MWNTs; b) Al_2O_3 agglomeration on the MWNT entangled network (Fully coated channel); c) Particle agglomeration on the silicon surface and the MWNT fin.

This study verifies that the major enhancement, when using nanofluids to cool heated surfaces, is the surface defects that are deposited on the surface. As stated by other researchers [121], these particles create imperfections on the surface causing an increased wettability. The channels which already contain

engineered structures increase the surface area and wettability and the thermal performance is not significantly improved.

3.7. In Summary

An experimental study was conducted to determine the heat removal ability of MWNTs grown in a silicon minichannel with Al_2O_3/H_2O nanofluid of volume concentration of 0.01% as the cooling medium. It was observed that the presence of MWNTs resulted in enhanced heat removal from the silicon base for a given volumetric flow rate. In the single phase regime, for the channel with no MWNTs, there was a 58% increase in the amount of heat flux that can be applied for a given temperature using nanofluids when compared to just using water as the base fluid. Using a fully covered MWNTs device, there was an 84% increase in the amount of heat flux applied and for the finned device there was 136% increase. The pressure drop with the coated MWNTs increased significantly to an unsmoothed channel; however, the addition of nanoparticles had no significant effect. When conducting this experiment multiple times, there was little to no increase in performance for the devices with MWNTs using nanofluid when compared to the base fluid of de-ionize water. For the no MWNT device, there was a significant performance enhancement for the first three runs until it peaked. This is due to the surface imperfections created by the sedimentation of the Al_2O_3 nanoparticles creating nucleation sites and increasing wettability of the surface. This study shows that one of the major contributions in removing heat while using a nanofluid is due to the

increased surface roughness. Brownian motion and thermal diffusion may have also contributed to the increase performance; however, it is not as significant as the change of surface structure.

This experiment is only tested for a volume concentration of 0.01% of Al_2O_3 nanoparticles suspended in water. In the future it should be tested for multiple concentrations of different kinds of nanoparticles submerged in various base fluids. It may also be interesting if the material of the fins react differently for different nanoparticle materials. In Chapter 4, using the lattice Boltzmann method (LBM), this setup is solved analytically. The LBM is based on microscopic models and mesoscopic kinetic equations and can accurately model nanofluids and finned structures.

Chapter 4

Modeling a Microchannel with Particle Suspensions using the Lattice Boltzmann Method

Based on the work conducted in the previous chapters, microchannels have proven to be adequate cooling devices that can remove large amounts of heat from small surfaces. The additions of surface extrusions and the use of different fluids are among the few components that can be changed in order to improve that cooling mechanism. Numerically modeling minichannel flow has proven to be less costly than experiments. Therefore, this chapter utilizes the lattice Boltzmann method (LBM) to model a microchannel with a heated surface and suspended solid particles in the fluid. Then using the relations for an ideal fin, results were obtained to account for surface roughness.

Few researchers have accurately implemented channel flow with increased surface roughness using the LBM [142–147]. Many other researchers have numerically investigated the suspension of solid particles within a fluid using the LBM [148–154]. To model the solid particles within the flow, they are modeled as "virtual liquid." The solid particles are treated as part of the fluid with additional forces because nanoparticles behave differently than the pure liquid. The forces that act in each particle is expressed as a vector sum and added to the momentum equation.

Few researchers have investigated the use of both nanofluids and mechanically induced surface structures. Zhou [136] passed silver nanofluids of different volume concentrations suspended into a PVP solution through an array of drop shaped micro pin fins in a microchannel. About an 18% increase in performance was obtained compared to a base fluid with little difference in the pressure drop. Tullius and Bayazitoglu [137,138] experimentally tested Al_2O_3 nanofluid flowing through a minichannel with multi-walled carbon nanotubes on the surface. They have found that combining both nanofluids and carbon nanotube fin structures provide only minor enhancement in thermal performance.

This chapter uses the LBM to simulate a two dimensional pressure driven flow through a minichannel. Particle suspensions were added to the fluid to model nanoparticles. Then assuming increased surface roughness was small fins, the relations for an ideal fin was used to obtain the improved results when applying surface roughness. This work is done in order to understand the flow characteristics

of nanoparticles within a fluid. The results shows that the forces the solid particles undergo do not contribute to as much enhanced thermal performance that the appearance of surface roughness creates.

4.1. Lattice Boltzmann Method (LBM)

The LBM is used to accurately model particle suspensions flowing through a minichannel. This method portrays a fluid as an ensemble of many particles interacting locally at the nodes in a lattice through streaming and collisions. This discrete microscopic model can easily recover the conservation laws of the continuum fluid dynamics and thus allows the calculation of the macroscopic variables such as density and velocity. This method acts as a special finite difference scheme for the kinetic equations. The LBM can adequately solve fluid flow applications for interfacial dynamics and complex boundaries and is suitable for all flow regimes [58]. This method is a simplified version of the Boltzmann equations which takes into account the streaming and collision of particles by the use of a particle distribution function. This function denotes the mass density contributed by the set of particles having the discrete velocity, $\vec{e}$. The equations to portray the fluid and energy flow are:

$$\underbrace{f(\vec{x},t) = f(\vec{x}+\vec{e}\Delta t, t+\Delta t)}_{\text{Streaming}} + \underbrace{\frac{f(\vec{x},t) - f^{eq}(\vec{x},t)}{\tau}}_{\text{Collision}} \qquad 4.1$$

$$\underbrace{g(\vec{x},t) = g(\vec{x}+\vec{e}\Delta t, t+\Delta t)}_{\text{Streaming}} + \underbrace{\frac{g(\vec{x},t) - g^{eq}(\vec{x},t)}{\tau_T}}_{\text{Collision}}. \quad 4.2$$

The parameters f and g are the particle distribution function for density and energy, respectively, τ and τ_T are the density and energy relaxation time, Δt is the time step, and $\vec{e}$ is the discrete particle velocity. The collision term depends on the nature of the molecular collisions and is very complex. Therefore, to estimate the collision term, the most common method, the Bhantengar-Gross-Krook (BGK), which is a linear approximation of the particle collision subject to a non-dimensional relaxation parameter, is used [155]. The relaxation time measures the amount of time the particles reach equilibrium. For this approximation, each component of the distribution function plateaus toward an equilibrium state with the same constant relaxation time, τ, making the Prandtl number, Pr, and the kinematic viscosity, ν, also fixed. For stability purposes, the value for τ ranges between 0.5-1 [156]. The parameters f^{eq} and g^{eq} are the equilibrium distribution for both density and energy, respectively. The local equilibrium function is derived from Maxwell's equations and can be defined by

$$f^{eq} = \frac{\rho}{(2\pi RT)^{D/2}} \exp\left[-\frac{(\vec{e}-\vec{u})^2}{2RT}\right] \quad 4.3$$

where ρ is the density, R is the gas constant, T is the temperature, D is the dimension, and $\vec{u}$ is the macroscopic velocity [157]. The lattice speed of sound, c_s,

is related to the gas constant and temperature by $c_s^2 = RT$. Similarly to the density equilibrium particle distribution function, the energy equilibrium distribution function is derived. For this paper, a two dimensional nine velocity lattice structure (2DQ9) was used which yields the density and energy equilibrium distribution functions to be

$$f_i^{eq} = \rho w_i \left[1 + \frac{3}{c^2} \vec{e} \cdot \vec{u} + \frac{9}{2c^4} (\vec{e} \cdot \vec{u})^2 - \frac{3}{2c^2} \vec{u} \cdot \vec{u} \right] \tag{4.4}$$

$$g_i^{eq} = \rho w_i \left[1 + \frac{3}{c^2} \vec{e} \cdot \vec{u} + \frac{9}{2c^4} (\vec{e} \cdot \vec{u})^2 - \frac{3}{2c^2} \vec{u} \cdot \vec{u} \right] \tag{4.5}$$

where w_i is the weighting factor, and c is the lattice speed [58,157]. For the 2DQ9 system the weighting factors and discrete velocities are given below. Figure 4.1 shows the streaming of the lattice structures and its lattice spacing.

$$w_i = \begin{cases} 4/9, & i = 0; \\ 1/9, & i = 1,2,3,4; \\ 1/36, & i = 5,6,7,8; \end{cases} \tag{4.6}$$

$$e_i = \begin{cases} (0,0), & i = 0; \\ (\pm 1,0)c, (0,\pm 1)c, & i = 1,2,3,4; \\ (\pm 1,\pm 1), & i = 5,6,7,8; \end{cases} \tag{4.7}$$

c is the lattice velocity in terms of the lattice spacing along the x and y axis and the time step, $c = \Delta x / \Delta t$. For simplicity, $\Delta x = \Delta y = \Delta t = 1$. The lattice velocity is related to the lattice speed of sound by $3c_s^2 = c^2$.

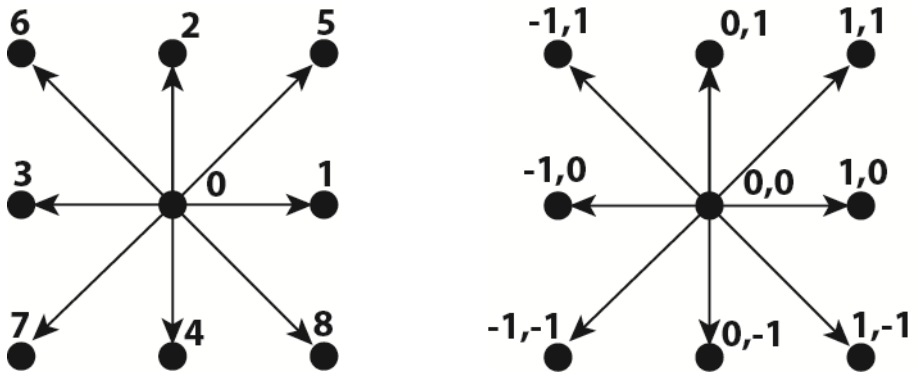

Figure 4.1: Lattice a) structure and b) coordinates for a D2Q9 LBM model

The macroscopic properties: density, velocity, and temperature, can be obtained directly from the particle distribution function equations using Equations 4.8-4.10. The density is the summation of the particle distribution function and the velocity is the summation of the distribution function multiplied by the lattice velocity over the density. Temperature is the summation of the energy particle distribution function multiplied by the lattice velocity over the density.

$$\rho_i = \sum_{i=0}^{N} f_i \tag{4.8}$$

$$u = \frac{1}{\rho} \sum_{i=0}^{N} f_i e_i \tag{4.9}$$

$$T = \frac{1}{\rho} \sum_{i=0}^{N} g_i e_i \tag{4.10}$$

The Shan-Chen multiphase model is used to incorporate additional external forces such as the body force driven by pressure [143,158]. This interparticle potential model mimics microscopic interaction forces between the fluid and solid

components. Using an equilibrium velocity that includes the additional forces, the collision operator is modified. This new equilibrium velocity is substituted into the equilibrium distribution function equations, Equations 4.4 and 4.5.

$$\bar{u} = \frac{1}{\rho}\sum_{i=0}^{N} f_i \bar{e}_i + \tau F_{Total}\frac{1}{\rho} \qquad 4.11$$

F_{Total} is the summation of external forces. One external force is the body force, F_{body}, due to the pressure difference in the x-direction. This new velocity is used to calculate the equilibrium distribution function. The body force can be found by

$$F_{body,i} = m \cdot a = m \cdot \frac{1}{\rho}\frac{\Delta p}{L} \qquad 4.12$$

Δp is the pressure drop across the channel, m is the mass of the fluid, and Δx is the length of the channel. Because the fluid is single phase in nature, intermolecular forces such as adhesive and cohesive forces and surface wettability effects not included in this program; however, they could easily be implemented to the summation of forces.

4.2. Particle Suspensions

To model the particle suspensions in the LBM program, they are taken as "virtual nodes" or "virtual fluids." The solid particles are treated as part of the fluid with additional forces because nanoparticles behave differently than the pure liquid. The forces that act in each particle is summed and added to the momentum

equation given in Equation 4.11. The particle moves to a new location due to the motion of the solid particles created by the extra forces and fluid is taking its place. When this happens, the additional forces acting on the particle at those nodes must be subtracted from the now fluid node. The forces considered for each particle is the gravity and buoyancy force, drag force, and Brownian motion [149,152]. For the gravity, F_g, and the buoyancy force, F_B, the expression is

$$F_g - F_B = -grav\left(\rho_f - \rho_p\right)V \tag{4.13}$$

where $grav$ is gravity, ρ_f and ρ_p are the density of the fluid and particle, respectively, and V is the volume of the particle. This force is added in the y-direction. For the drag force on each solid particle, F_D, the expression is

$$F_D = -\frac{1}{2} C_D A \rho_f \Delta u^2 . \tag{4.14}$$

C_D is the drag coefficient, A is the reference area, and Δu is the fluid velocity relative to the particle. This force is applied in the opposite direction of the fluid flow. The Brownian motion is the random movement of the particle. Therefore in this program, for each particle, a force is randomly applied in different directions. The expression is given below.

$$F_{Brown} = C_B \frac{k_B T}{r} \tag{4.15}$$

C_B is a coefficient of an integer of either -1, 0, or 1, k_B is the Boltzmann constant, T is the absolute temperature of the fluid, and r is the diameter of the particle. A schematic of the forces acting on the solid particles is given in Figure 4.2. The total forces added to the solid particles are the summation of $F_G - F_B$, F_D, F_{Brown} along with the body force, F_{body}, due to the pressure.

$$F_{Total,particle} = F_{body} + \left(F_g - F_B\right) + F_D + F_{Brown} \tag{4.16}$$

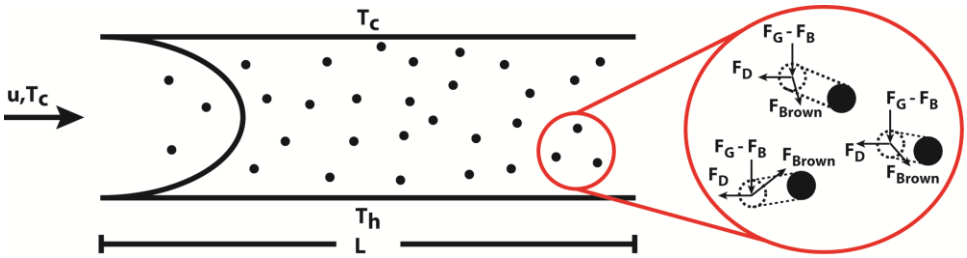

Figure 4.2: Schematic of forces acting on the particles

4.3. Boundary Conditions

4.3.1. Inlet/Outlet

The computations is set to run a pressure driven flow boundary condition at the inlet and outlet that was developed by Zou and He [159]. At the inlet and outlet you can initiate a pressure or a velocity and compute the unknown values. Using the macroscopic equations for density and velocity, the unknown distribution functions can be found using the known values. For this 2DQ9 model, at the inlet, the unknowns f_1, f_5, f_8, and either u or ρ can be determined with the other known values and the macroscopic equations for density and velocity. Using the system of

equations you can determine the 4 unknowns with 4 equations. The derivation of the equations for the inlet is below and the unknowns for the outlet are found similarly. Figure 4.3 shows the schematic for both the inlet and outlet boundary conditions where the dotted lines represent the unknowns at the respective section.

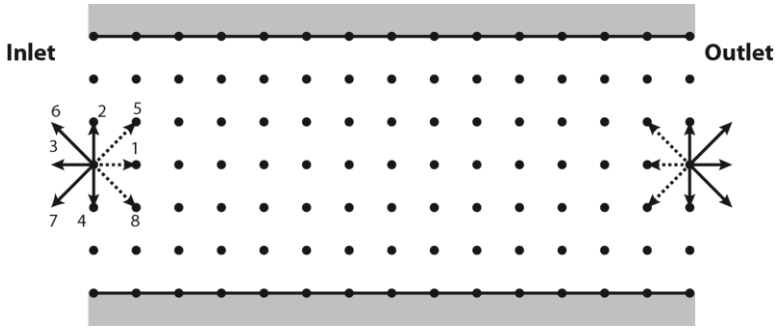

Figure 4.3: Lattice boundary conditions for the inlet and outlet (solid lines represent known values and dashed lines are unknown)

To derive the inlet boundary conditions for a pressure driven flow, the macroscopic property equations for density and velocity are used. The unknowns for the inlet are f_1, f_5, f_8, and ρ for our system as seen in the Figure 4.3. The expressions for the unknowns are derived by the following.

$$\rho = \sum_{i=0}^{8} f_i \tag{4.17}$$

$$f_1 + f_5 + f_8 = \rho - \left(f_0 + f_2 + f_3 + f_4 + f_6 + f_7 \right) \tag{4.18}$$

$$u = \frac{1}{\rho} \sum_{i=0}^{8} f_i e_i \tag{4.19}$$

$$f_5 = f_7 - \frac{1}{2}\left(f_2 - f_4 \right) + \rho u_x + \rho u_y \tag{4.20}$$

$$f_8 = f_6 + \frac{1}{2}\left(f_2 - f_4\right) + \rho u_x - \rho u_y \tag{4.21}$$

where $u_y = 0$ at the inlet. And from the bounceback theory, described in the next section, f_1 can be obtained by

$$f_1 = f_3 + f_1^{eq} - f_3^{eq} \tag{4.22}$$

Plugging in the equilibrium distribution function from Equation 4.4 with the appropriate weights the equation for f_1 simplifies to:

$$f_1 = f_3 + 2/3\,\rho u_x \tag{4.23}$$

By substituting the equations for f_1, f_5, and f_8 into Equation 4.18, the equation for density can be obtained by:

$$\rho = \left(f_0 + f_2 + f_4 + 2\left(f_3 + f_6 + f_7\right)\right) \Big/ \left(1 - u_x\right) \tag{4.24}$$

The outlet boundary conditions are found in a similar manner for the unknowns f_3, f_6, f_7, and u_x. The initial velocity condition, $u(y)$, for the pressure driven flow was given as a parabolic flow

$$u(y) = \frac{4u_{\max}}{\left(y_{top} - y_{bottom}\right)^2}\left(y - y_{bottom}\right)\left(y_{top} - y\right) \tag{4.25}$$

A constant inlet temperature is applied to the program and is run until the system reaches steady state. The temperature profile is then captured based on the energy distribution function.

4.3.1. Walls

The correct boundary conditions on the walls are essential for determining the flow characteristics at the boundary. The boundary condition that has been chosen for this model is the bounceback boundary condition. This no-slip boundary conditions can be used for all boundary conditions and is easily implemented. The concept of these methods is that the incident distribution functions are reflected back into the domain. This method is developed by Ziegler [160] and is mainly used for small Knudsen numbers (Kn). The bounceback method is defined by

$$f_i(x,t) = f_{opp(i)}(x,t) \tag{4.26}$$

where

$$\begin{aligned} f_2(x,t) &= f_4(x,t) \\ f_4(x,t) &= f_2(x,t) \\ f_5(x,t) &= f_7(x,t) \\ f_6(x,t) &= f_8(x,t) \\ f_7(x,t) &= f_5(x,t) \\ f_8(x,t) &= f_6(x,t) \end{aligned} \tag{4.27}$$

The mass and momentum is conserved in this method. On average, at the boundary, the velocity is zero because any particle entering the sites is reflected

with the same velocity in the opposite direction. In this bounceback condition, the collision process does not occur at the boundary. This is also portrayed more clearly in Figure 4.4. The dashed lines are the reflected distribution functions and the solid lines are the incident distribution functions. The colors coordinate with the respective incident and reflected distribution function. Similar to the density distribution function, the bounceback boundary condition can be applied for the energy distribution function.

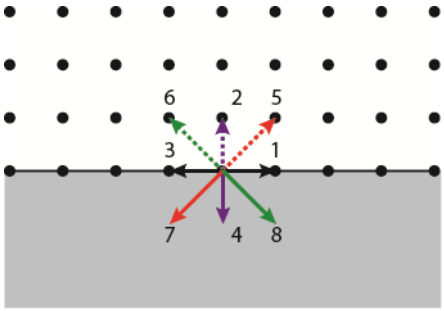

Figure 4.4: Bounceback boundary condition schematic (solid lines represent incident rays and dashed lines are reflected). The colors coordinate with each other.

4.4. Mathematical Algorithm of the LBM

The nature of the program is to understand the characteristics of the flow and heat transfer for a two dimensional model of a minichannel with nanoparticles suspended in a base fluid. The algorithm of the FORTRAN 90 code is below:

i. Construct lattice structure image labeling inlet/outlet, and walls
ii. Initiate physical properties including density and energy particle distribution function
iii. Start time dependent flow loop

iv. Apply boundary conditions to walls and inlet/outlet
v. Compute macroscopic properties based on the initial conditions
vi. Compute forces on fluid and solid particles
vii. Compute density and energy particle distribution function
viii. Calculate the collision
ix. Stream the distribution function
x. Reconstruct solid particles in image based on the lattice distance caused by the applied forces – the additional forces added to the solid particles need to be subtracted from where the nanoparticles once stood
xi. If the max time step has not been met, go back to step iii. Otherwise end flow loop

The program is designed to manually input whether there is nanoparticles, and within the fluid and at what volume concentration. This is easily applied to be able to compare the addition of different volume concentrations of solid particle suspension.

4.5. Physical Units to Lattice Units

Input variables in the LBM are in terms of lattice units and are easily converted into physical units and vice versa. For a time step, $\Delta t = 1\,\mathrm{ls}$, and grid spacing, $\Delta x = \Delta y = 1\,\mathrm{lu}$, the parameters are converted directly to lattice units, lu, form physical units. This section will outline how this conversion is achieved before and after the program is compiled and ran. Let the number of nodes in the y-

direction, which accounts for the height of the channel to be N_y. The height of the channel is $N_y - 1$ lu. The relation between the physical grid spacing and the lattice grid spacing is given as a ratio.

$$\frac{\Delta x_{phys}}{\Delta x_{lu}} = \frac{\text{Length of physical units}}{\text{Length of lattic units}} = \frac{2H}{N_y - 1} \text{ m/lu} \tag{4.28}$$

The kinematic viscosity in terms of lattice units is calculated in terms of the relaxation time and for $\Delta t = 1$ ls and $c_s = c/\sqrt{3} = 1/\sqrt{3}$ by

$$\upsilon_{lu} = \left(\tau - \frac{1}{2}\right) c_s{}^2 \Delta t \text{ lu}^2/\text{ls} \tag{4.29}$$

and the thermal diffusivity is given by

$$\alpha_{lu} = \left(\tau_T - \frac{1}{2}\right) c_s{}^2 \Delta t \text{ lu}^2/\text{ls}. \tag{4.30}$$

The Prantl number (Pr) is obtained by

$$\text{Pr} = \frac{(\tau - 0.5)}{(\tau_T - 0.5)}. \tag{4.31}$$

The equation of state can easily define the pressure with

$$p = \rho c_s{}^2. \tag{4.32}$$

Going back to physical units, the Reynolds number (Re) for the flow through the channel is given as

$$\mathrm{Re}_{phys} = \frac{2H \times u_{phys}}{\upsilon_{phys}}, \tag{4.33}$$

where $2H$ is the hydraulic diameter of the channel, u_{phys} is the initial velocity of the fluid, and υ_{phys} is the kinematic viscosity of the fluid. The relationship between the viscosity in physical and lattice units is given by

$$\upsilon_{lu} = \upsilon_{phys} \frac{\Delta t_{phys}}{\Delta x_{phys}^{\ 2}} \ \mathrm{lu}^2/\mathrm{ls} \tag{4.34}$$

Rearranging and solving for Δt_{phys}, the equation becomes

$$\Delta t_{phys} = \upsilon_{lu} \frac{\Delta x_{phys}^{\ 2}}{\upsilon_{phys}} \ \mathrm{s/ls} \tag{4.35}$$

The inlet velocity converted to lattice units is given by

$$u_{lu} = u_{phys} \frac{\Delta t_{phys}}{\Delta x_{phys}} \ \mathrm{lu/ls} \tag{4.36}$$

To verify the conversion is correct, you can use the Re in terms of lattice units where $\mathrm{Re}_{lu} = \mathrm{Re}_{phys}$.

$$\mathrm{Re}_{lu} = \frac{u_{lu}\left(N_y - 1\right)}{\upsilon_{lu}^{\ 2}} = \mathrm{Re}_{phys} = \frac{u_{phys} 2H}{\upsilon_{phys}^{\ 2}}. \tag{4.37}$$

To scale the density from lattice to physical units the relation is in terms of a reference density, ρ_{ref}.

$$\rho_{phys} = \rho_{lu}\rho_{ref} \tag{4.38}$$

The temperature variation in lattice units is given a value between 0-1 where 0 represents the lowest temperature and 1 is the highest. To scale up the temperature, the difference in physical units, ΔT, is multiplied by the lattice units temperature and added to the reference temperature T_c.

$$T_{phys} = T_{lu}\Delta T + T_C \quad K \tag{4.39}$$

To ensure incompressibility of the fluid the Mach number, Ma, needs to be below 1. A value beyond this number creates a bigger dependence on pressure and density. Ma is defined as the lattice velocity, u_{lu}, over the lattice speed of sound.

$$Ma = \frac{u_{lu}}{c_s} \ll 1 \tag{4.40}$$

The units are converted before and after the program are compiled and ran with similar relations as stated above.

4.6. Model Parameters and Validation

The 2D model of flow between two parallel plates is modeled using fluid properties given in Table 4.1. Both the physical and lattice properties are given where the conversions between the physical and lattice units can be obtained by the equations given in Section 4.5. The model is pressure driven with a velocity profile given by Equation 4.25. There is a temperature difference between the bottom, T_H,

and top, T_C, walls where $T_H = 320K$ and $T_C = 300K$. The initial temperature given to the fluid is T_C. A lattice structure of 251 x 1251 was used for this model. The lattice structure size is determined to ensure adequate transfer of flow and thermal properties for suspended particles to the fluid with a channel in the mirco region. This means that when particles are added to the system, they are represented in the lattice as 1 lu in diameter. One lattice structure represents a cluster of nanoparticles roughly 200 nm in diameter. An optimal relaxation time was found to be $\tau = 0.75$. Properties for Al_2O_3 particles were modeled for volume concentrations, ϕ, of 0.001-0.0075%. The heat transfer results are given in terms of Nu and Re.

Properties	Lattice Units	Physical Units
	Fluid	
Re	100-600	
ρ	3 lm/lu^3	997 kg/m^3
2H	250 lu	50 μm
L	1250 lu	250 μm
	Particle	
ρ	12 lm/lu^3	4000 kg/m^3
ϕ	0.001-0.0075%	

Table 4.1:Model Physical and Lattice Properties

In order to validate this model, the above properties and a Re = 500 is used. No additional body force applied to the model in this validation. Figure 4.5a below compares the results of the analytical solution given in Equation 4.25 to the data obtained from the LBM model. From the figure you can see that the results match the analytical solution therefore validating the program. Figure 4.5b shows the temperature profile obtained from the LBM model. These results are compared to

an analytical solution of the temperature profile at the thermal boundary layer described below. For a dimensionless temperature, $\theta(x,y)$ and using a parabolic velocity profile, the temperature profile is

$$\theta(x,y) = 2\left(\frac{y}{\delta_t}\right) - \left(\frac{y}{\delta_t}\right)^2 . \qquad 4.41$$

δ_t is the thermal boundary layer thickness defined as

$$\delta_t(x) = 5.085\frac{x}{\mathrm{Pr}^{1/3}\,\mathrm{Re}_x^{1/2}} \qquad 4.42$$

where the Re_x is based on the length of the channel in the x-direction, $\mathrm{Re}_x = \frac{u\,x}{\nu}$. The non-dimensional temperature is defined in terms of the bulk temperature, T_∞, the wall temperature, T_w, and the temperature distribution, $T(x,y)$ [161].

$$\theta(x,y) = \frac{T(x,y) - T_w}{T_\infty - T_w} \qquad 4.43$$

From Figure 4.5b the non-dimensional temperature profiles are similar.

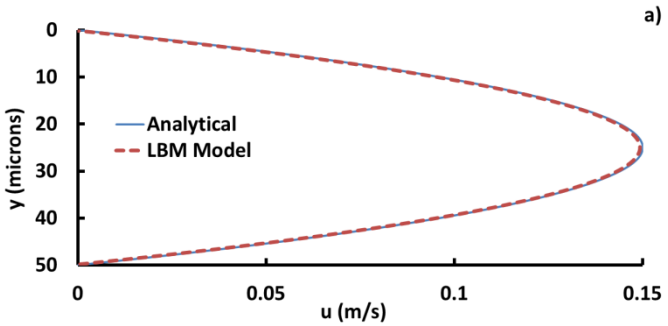

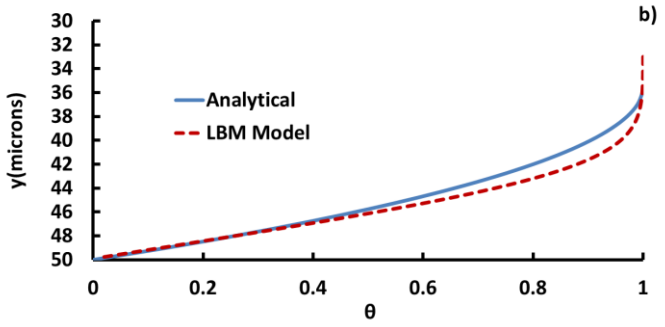

Figure 4.5:Validation: a) Velocity profile to an analytical solution; b) Temperature profile to analytical solution

4.7. Simulations Results

This work was completed in reaction to the results provided by Tullius and Bayazitoglu [138] which found that a significant contribution when using nanofluid is due to the sedimentation of solid particles found on the channel surface providing increased wettability. In order to isolate the increased performance for nanofluid, the LBM equation is used to model first nanoparticle suspension in a base fluid through two parallel plates. Then treating the surface roughness as finned structures, with the fins acting as an ideal fin, i.e. the fin efficiency equals unity, was taken into account to obtain results for increase surface roughness.

In order to evaluate the local heat transfer characteristics at the surface the results are given in terms of the local Nusselt number (Nu) vs Reynolds number (Re). The local Nu is defined using

$$Nu = \frac{hL}{k} \qquad 4.44$$

where L is the channel length subjected to heat or the flow length, h is the heat transfer coefficient, and k is the thermal conductivity of the fluid. Fourier's equations for conduction, Equation 4.45, and convection, Equation 4.46, are used to solve for a local h, Equation 4.47, then an average h, Equation 4.48, was computed across the channel [161].

$$q = k \left. \frac{\partial T(x,y)}{\partial y} \right|_{y=0} \tag{4.45}$$

$$q = h(x)\left(T_\infty - T_w\right) \tag{4.46}$$

$$h(x) = k \left. \frac{\partial T(x,y)}{\partial y} \right|_{y=0} \left(\frac{1}{T_\infty - T_w} \right) \tag{4.47}$$

$$\bar{h} = \frac{1}{L} \int_0^L h(x)\, dx \tag{4.48}$$

The parameter q is the wall heat flux. Then using Equation 4.44 and the average $\bar{h}$, the average Nu was obtained.

The LBM results for a basic channel with different solid particle conentrations is given in Figure 4.7. It shows that, like the literature[30,122,124,125], with increasing volume concentration there is an enhanced thermal performance through the minichannel. There was roughly a 1%, 5% and 7% increase for a volume concentration of 0.001, 0.005, and 0.0075, respectively.

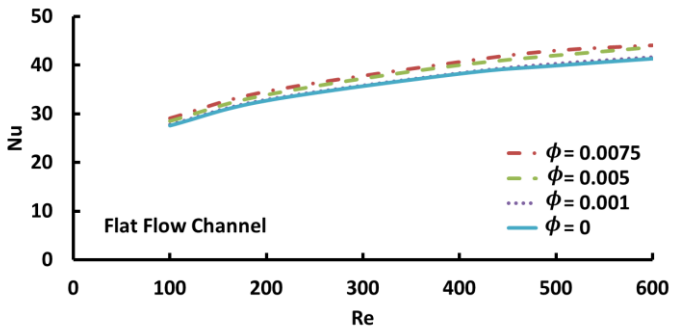

Figure 4.6: LBM data for suspended particles in a 2-D flow between parallel plates

A roughened surface is treated as many small rectangular fins. Although this fin geometry is not a practical portrayal of increased surface roughness, it is considered as a close approximation. Figure 4.7shows the roughened channel.

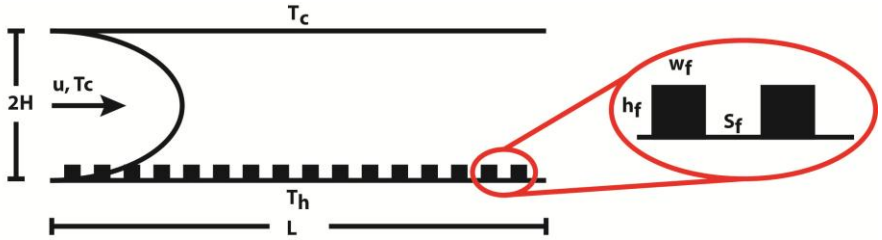

Figure 4.7: Profile of channel with roughened surface

An approximation of the roughened surface was obtained using the equations for an ideal fin, Q_{ideal}, where the heat transfer through the fin, Q_{fin}, is

$$Q_{fin} = \eta Q_{ideal} = \eta a_f h \theta_o \qquad 4.49$$

The parameter η is the fin efficiency, a_f is the surface area of the fin, h is the heat transfer coefficient, and θ_o is the temperature distribution where $\theta_o = T_W - T_\infty$. An ideal fin assumes that the entire fin surface remains at a base temperature of T_H. When the fins are considered ideal, then the fin efficiency becomes $\eta = 1$. The fin

effectiveness can be determined based on the ration of heat transfer through the fin and heat transfer of the surface without fins yielding the following equation.

$$\varepsilon_f = \frac{Q_{fin}}{Q_{nofin}} = \frac{Q_{ideal}}{Q_{nofin}} \tag{4.50}$$

where

$$Q_{nofin} = a_o h \theta_o . \tag{4.51}$$

a_o is the surface area of the base [161]. The heat transfer is assumed to be constant, therefore, the fin effectiveness becomes the ratio of the surface areas times the efficiency.

$$\varepsilon_f = \frac{\eta a_f h \theta_o}{a_o h \theta_o} = \frac{\eta a_f}{a_o} = \frac{a_f}{a_o} \tag{4.52}$$

Using this ratio, new results for surface roughness can be obtained. The roughened surface is measured by a ratio of the fin height, h_f, to the channel height, $2H$, or the relative roughness, ε. The roughness is given in terms of a percentage between 0.8-3.6%. The roughness height is kept below 2 μm high to ensure practical calculations.

$$\varepsilon = \frac{h_f}{2H} \times 100 \tag{4.53}$$

Figure 4.8 shows the results after incorporating ideal fin approximations on the surface of the microchannel as increased surface roughness. All the results are

relative to a channel with no surface roughness approximations and no suspended solid particles. Figure 4.8a shows that with increasing relative roughness increases the Nu values through the channel improving the thermal performance. With a relative roughness of about 4%, the thermal performance increases about 59%. With suspended particles in the base fluid, there was a thermal enhancement of 60%, 64%, 67% for volume concentration of 0.001, 0.005, and 0.0075, respectively, at the same relative roughness. This is shown in Figure 4.8b. Figure 4.8c shows the results from the previous figures on the same graph to get a better perspective of the enhanced performance for relative roughness of 0% and 3.6%. This work verifies that addition of surface roughness can increase the thermal performance more significantly than the addition of suspended particles in a base fluid.

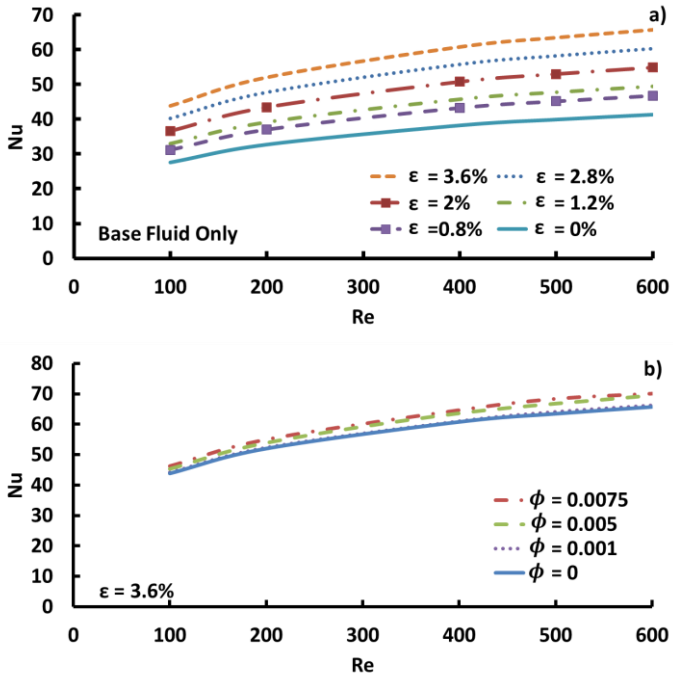

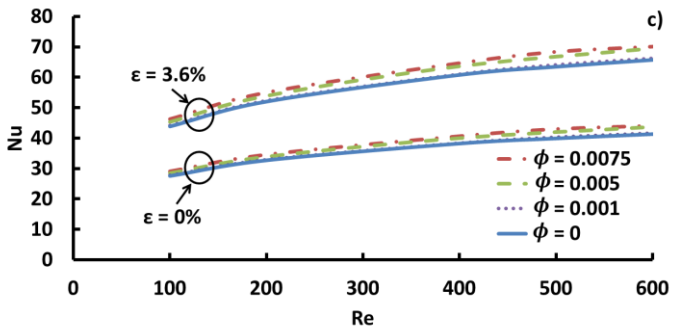

Figure 4.8: Microchannel results when accounting for increased surface roughness when using : a) Base fluid only; b) Relative roughness of 3.6% for different particle concentrations; c) Both relative roughness at 0 and 3.6% for all particle concentrations

4.8. In Summary

A numerical simulation of a 2 dimensional flow between parallel plates with both suspended nanoparticles was modeled using the LBM. Then using an approximation of an ideal fin the surface roughness results were obtained. It was found that with increased volume concentration increases the thermal performance. With increased fin height, the thermal performance also increased. With a surface roughness of about 2 μm (i.e. $\varepsilon = 3.6\%$) the thermal performance increased more significantly than the addition of solid particles ($\phi = 0.0075$). Therefore, changing the structure of the surface is more effective than the addition of solid particles in the base fluid at low concentrations and Re. The addition of surface roughness can provide a more significant contribution in removing heat similar to the findings in Tullius and Bayazitoglu [138] found in their experimental work. This work did have limitations and should be further improved to capture higher flow rates, higher nanoparticle volume concentrations, and different solid particles properties. Future

work might include considering slip boundary conditions, and a multiple relaxation time to improve the stability and accuracy of the program.

Chapter 5

Conclusion

My dissertation describes a series of projects inclined to enhance a small heat exchanger, known as a microchannel, in order to improve the cooling of microelectronic devices. It is found that by modifying the walls of microchannels, can significantly improve the thermal performance in devices; however, it comes with a price- increases pressure drop.

An extensive review work regarding microchannel cooling was given in Chapter 1. Then a numerical project using computational fluid dynamics investigated the effects of cooling for different fin configurations placed on the bottom of a heated surface in a minichannel. Empirical correlations describing the Nusselt number and the Darcy friction factor were obtained and compared to recent studies. Triangular fins with larger fin height, smaller fin width, and spacing double the fin width maximizes the number of fins in each row and yields better thermal

performance. In Chapter 3, an experimental investigation of a microchannel using both water and Al_2O_3/H_2O nanofluid with MWNTs as the protruding surface structures is discussed. It was observed that the sedimentation of Al_2O_3 nanoparticles on a channel surface with no MWNTs increases the surface roughness and the thermal performance. Finally, using the lattice Boltzmann method, a two dimensional channel with suspended particles is modeled in order to get an accurate characterization of the fluid/particle motion in nanofluid. Using the analysis based on an ideal fin, approximate results for nanofluids with increase surface roughness was obtained. The results confirmed the conclusions obtained in the experimental work discussed in Chapter 3 where changing the fin structures.

Microchannels have proven to be effective cooling systems and understanding how to achieve the maximum performance is vital for the innovation of electronics.

References

[1] Narayanaswamy R., Chandratilleke T. T., and Foong A. J. L., 2008, "Laminar Convective Heat Transfer in a Microchannel with Internal Fins," Proceedings of the Sixth International ASME Conference on Nanochannels, Microchannels and Minichannels ICNMM2008-62044, pp. 1–5.

[2] Kordás K., Tóth G., Moilanen P., Kumpumäki M., Vähäkangas J., Uusimäki A., Vajtai R., and Ajayan P. M., 2007, "Chip Cooling with Integrated Carbon Nanotube Microfin Architectures," Applied Physics Letters, **90**(12), p. 123105.

[3] Mo Z., Anderson J., and Liu J., 2004, "Integrating Nano Carbontubes with Microchannel Cooler," Proceeding of the Sixth IEEE CPMT Conference HDP04, pp. 373–376.

[4] Zhong X., Fan Y., Liu J., Zhang Y., Wang T., and Cheng Z., 2007, "A Study of CFD Simulation for On-chip Cooling with 2D CNT Micro-Fin Array," Proc International Symposium on High Density packaging and Microsystem Integration HDP 07, pp. 1–6.

[5] Zhong X., Wang T., Liu J., Zhang Y., and Cheng Z., 2006, "Computational Fluid Dynamics Simulation for On-chip Cooling with Carbon Nanotube Micro-fin Architectures," 2006 International Conference on Electronic Materials and Packaging, pp. 1–6.

[6] Dix J., Jokar A., and Martinsen R., 2008, "A Microchannel Heat Exchanger for Electronics Cooling Applications," Proceedings of the Sixth International ASME Conference on Nanochannels, Microchannels and Minichannels ICNMM2008-62351, pp. 23–24.

[7] Lee P., and Teo C., 2008, "Heat Transfer Enhancement in Microchannels Incorporating Slanted Grooves," Proceedings of Micro/Nanoscale Heat Transfer International Conference MNHT2008-52374, (65), pp. 1–5.

[8] Shokouhmand H., Aghvami M., and Afshin M. J., 2008, "Pressure Drop and Heat Transfer of Fully Developed, Laminar Flow in Rough, Rectangular Microchannels," Proceedings of the Sixth International ASME Conference on Nanochannels, Microchannels and Minichannels ICNMM2008-62042, **2**, pp. 1–5.

[9] Truong B., Hu L., and Buongiorno J., 2008, "Surface Modifications using Nanofluids for Nucleate Boiling Heat Transfer and CHF Enhancements," Proceedings of the Sixth International ASME Conference on Nanochannels, Microchannels and Minichannels ICNMM2008-62085, pp. 1–7.

[10] Solovitz S. A., 2008, "Computational Study of Grooved Microchannel Enhancements," Proceedings of the Sixth International ASME Conference on Nanochannels, Microchannels and Minichannels ICNMM2008-62128, pp. 1–8.

[11] Baghernezhad N., and Abouali O., 2008, "Numerical Ivestigation of Single Phase Heat Transfer Enhancement in a Microchannel with Grooved Surfaces," Proceedings of the Sixth International ASME Conference on Nanochannels, Microchannels and Minichannels ICNMM2008-62262, pp. 1–8.

[12] Vanapalli S., Brake H. J. M. Ter, Jansen H. V, Burger J. F., Holland H. J., Veenstra T. T., and Elwenspoek M. C., 2007, "Pressure Drop of Laminar Gas Flows in a Microchannel Containing Various Pillar Matrices," Journal of Micromechanics and Microengineering, **17**(7), pp. 1381–1386.

[13] Lee Y.-J., Lee P.-S., and Chou S.-K., 2009, "Enhanced Microchannel Heat Sinks using Oblique Fins," Proceedings of IPACK2009.

[14] Morris J. S., 2008, Nanopackaging: Nanotechnologies and Electronics Packaging, Springer, Portland.

[15] Ekstrand L., Mol Z., Zhang Y., and Liu J., 2005, "Modelling of Carbon Nanotubes as Heat Sink Fins in Microchannels for Microelectronics Cooling," Polytronic 2005 - 5th International Conference on Polymers and Adhesives in Microelectronics and Photonics, pp. 185–187.

[16] Iii W. A. G., Che J., and Ca T., 2000, "Thermal Conductivity of Carbon Nanotubes," Nanotechnology, **11**, pp. 65–69.

[17] Kuo C.-H., and Huang H.-M., 2008, "Measurements on the Thermal Conductivity of Epoxy/Carbon - Nanotube Composite," Proceedings of Micro/Nanoscale Heat Transfer International Conference MNHT2008-52189, (1998), pp. 1–6.

[18] Harris P. J. ., 2009, Carbon Nanotube Science: Synthesis, Properties and Applications, Cambridge University Press.

[19] Treacy M. M. J., Ebbesen T. W., and Gibson J. M., 1996, "Exceptionally High Young's Modulus Observed for Individual Carbon Nanotubes," Nature, **381**(6584), pp. 678–680.

[20] Jorio A., Dresselhaus M. S., and Dresselhaus G., 2008, Carbon Nanotubes: Advanced Topics in the Synthesis, Structure, Properties and Applications, Springer, New York.

[21] Mo Z., Morjan R., Anderson J., Campbell E. E. B., Liu J., and Road Y. C., 2005, "Integrated Nanotube Microcooler for Microelectronics Applications," Electronics Components and Technology Conference, pp. 51–54.

[22] Wright B., Thomas D., Hong H., Groven L., Puszynski J., Duke E., Ye X., and Jin S., 2007, "Magnetic Field Enhanced Thermal Conductivity in Heat Transfer Nanofluids Containing Ni Coated Single Wall Carbon Nanotubes," Applied Physics Letters, **91**(17), p. 173116.

[23] Lukes J. R., and Zhong H., 2007, "Thermal Conductivity of Individual Single-Wall Carbon Nanotubes," Journal of Heat Transfer, **129**(6), p. 705.

[24] Shiomi J., and Maruyama S., 2011, "Molecular Dynamics Simulations of Diffusive-Ballistic Heat Conduction in Carbon Nanotubes," MRS Proceedings, **1022**, pp. 1–6.

[25] Yao Z., Wang J.-S., Li B., and Liu G.-R., 2004, "Thermal Conduction of Carbon Nanotubes using Molecular Dynamics," Physical Review B, **71**(8), p. 15.

[26] Maruyama S., 2003, "A Molecular Dynamics Simulation of Heat Conduction of a Finite Length Single-Walled Carbon Nanotube," Nanoscale and Microscale Thermophysical Engineering, **7**(1), pp. 41–50.

[27] Bock H. P. J. De, Varanasi K., Chamarthy P., Deng T., Kulkarni A., Rush B. M., Russ B. A., Weaver S. E., and Gerner F. M., 2008, "Experimental Investigation of Micro/Nano Heat Pipe Wick Structures," Proceedings of IMECE2008 Proceedings of the ASME International Mechanical Engineering Congress and Exposition IMECE2008-67288, pp. 1–6.

[28] Pasupuleti T., and Kandlikar S. G., 2009, "Cooling of Microelectronic Devices Packaged in a Single Chip Module using Single Phase Refrigerant R-123," Proceedings of the ASME 2009 7th International Conference on Nanochannels, Microchannels and Minichannels ICNMM2009-82262, pp. 1–5.

[29] Golubovic M., Hettiarachchi H. D. M., and Worek W. M., 2008, "Nanofluids and Critical Heat Flux," Proceedings of Micro/Nanoscale Heat Transfer International Conference MNHT2008-52360, pp. 1–10.

[30] Kim S. J., Mckrell T., Buongiorno J., and Hu L., 2008, "Experimental Study of Flow Crictical Heat Flux in Low Concentration Water-Based Nanofluids," MNHT2008-52321, pp. 1–5.

[31] Buongiorno J., Hu L., and Bang I. C., 2007, "Towards an Explanation of the Mechanism of Boiling Critical Heat Flux," Proceedings of the Fifth International Conference on Nanochannels, Microchannels and Minichannels ICNMM2007-30156, pp. 1–7.

[32] Xie H., Chen L., Li Y., and Yu W., 2008, "Thermal Transport Properties of Nanofluids Containing Carbon Nanotubes," Proceedings of the Sixth International ASME Conference on Nanochannels, Microchannels and Minichannels ICNMM2008-62210, **477**(1-2), pp. 1–5.

[33] Shokouhmand H., Ghazvini M., and Shabanian J., 2008, "Analysis of Microchannel Heat Sink Performance using Nanofluids in Turbulent and Laminar Flow Regimes and its Simulation using Artificial Neural Network," 10th International Conference on Computer Modelling Simulation, pp. 623–628.

[34] Kabelac S., and Anoop K. B., 2008, "Experimental Convective Heat Transfer with Nanofluids," Proceedings of the Sixth International ASME Conference on Nanochannels, Microchannels and Minichannels ICNMM2008-62099, pp. 1–7.

[35] Murshed S. M. S., Milanova D., and Kumar R., 2009, "An Experimental Study of Surface Tension-Dependent Pool Boiling Characteristics of Carbon Nanotubes-Nanofluids," Proceedings of the ASME 2009 7th International Conference on Nanochannels, Microchannels and Minichannels ICNMM2009-82204, pp. 1–6.

[36] Chen C., and Ding C.-Y., 2009, "Heat Transfer Characteristics and Cooling Performance of Microchannel Heat Sinks with Nanofluids," Proceedings of the ASME 2009 7th International Conference on Nanochannels, Microchannels and Minichannels ICNMM2009-82079.

[37] Yu W., Xie H., Li Y., and Chen L., 2009, "The Thermal Transport Properties of Ethylene Glycol Based MGO Nanofluids," Proceedings of the ASME 2009 7th International Conference on Nanochannels, Microchannels and Minichannels ICNMM2009-82032, pp. 1–5.

[38] Das S. K., Choi S. U., Yu W., and Pradeep T., 2007, Nanofluids: Science and Technology, Wiley Interscience.

[39] Witharana S., Buonjiorno J., Chen H., Ding Y., and Et Al., 2009, "A Benchmark Study on the Thermal Conductivity of Nanofluids," Journal of Applied Physics, **106**(9), p. 094312.

[40] Wong K. V, and Castillo M. J., 2010, "Heat Transfer Mechanisms and Clustering in Nanofluids," Advances in Mechanical Engineering, pp. 1–10.

[41] Tou K. W., Xu G. P., and Tso C. P., 2001, "Liquid Cooling of Electronic Devices by Single-Phase Convection; Frank P. Incropera," Experimental Heat Transfer, **44**(2), pp. 1637–1638.

[42] Yu C. K., Lu D. C., and Cheng T. C., 2006, "Pool Boiling Heat Transfer on Artificial Micro-Cavity Surfaces in Dielectric Fluid FC-72," Journal of Micromechanics and Microengineering, **16**(10), p. 2092.

[43] Jones B. J., McHale J. P., and Garimella S. V., 2009, "The Influence of Surface Roughness on Nucleate Pool Boiling Heat Transfer," Journal of Heat Transfer, **131**(12), p. 121009.

[44] Kamali R., and Kharazmi A., 2011, "Molecular Dynamics Simulation of Surface Roughness Effects on Nanoscale Flows," International Journal of Thermal Sciences, **50**(3), pp. 226–232.

[45] Sadeghi A., Asgarshamsi A., and Saidi M. H., 2009, "Analysis of Laminar Flow in the Entrance Region of Parallel Plate Microchannels for Slip Flow,"

Proceedings of the ASME 2009 7th International Conference on Nanochannels, Microchannels and Minichannels ICNMM2009-82012, pp. 1–8.

[46] Bayazitoglu Y., Tunc G., Wilson K., and Tjahjono I., 2005, "Convective Heat Transfer for Single-Phase Gases in Microchannel Slip Flow: Analytical Solutions," Microscale Heat Transfer Fundamentals and Applications, pp. 125–148.

[47] Darbandi M., and Setayeshgar A., 2009, "Flow Past Confined Nano Cylinder in Microscale Channels," Proceedings of the ASME 2009 7th International Conference on Nanochannels, Microchannels and Minichannels ICNMM2009-82222, pp. 1–8.

[48] Sadeghi A., Asgarshamsi A., and Saidi M. H., 2009, "Laminar Forced Convection in Annular Microchannels with Slip Flow Regime," Proceedings of the ASME 2009 7th International Conference on Nanochannels, Microchannels and Minichannels ICNMM2009-82013, pp. 1–9.

[49] O'Hare L., and Reese J. M., 2007, "Numerical Models of Gas Flow and Heat Transfer in Microscale Channels: Capturing Rarefaction Behaviour using a Constitutive," Proceedings of the Fifth International Conference on Nanochannels, Microchannels and Minichannels ICNMM2007-30097.

[50] Icnmm P., and Dulikravich G. S., 2007, "Lattice Boltzmann Method for Steady Gas Flows in Microchannels," Proceedings of the Fifth International

Conference on Nanochannels, Microchannels and Minichannels ICNMM2007-30060.

[51] Bayazitoglu Y., and Kakac S., 2005, Flow Regimes in Microchannel Single Phase Gaseous Fluid Flow, Kluwer Academic Publisher Flow.

[52] Guzman A. M., Diaz A. J., Sanhueza L. E., and Escobar R. A., 2008, "Flow Characteristics of Rarified Gases in Micro-Grooved Channels by the Lattice-Boltzmann Method," Proceedings of Micro/Nanoscale Heat Transfer International Conference MNHT2008-52051, pp. 1–10.

[53] Harley J. C., Huang Y., Bau H. H., and Zemel J. N., 1995, "Gas Flow in Microchannels," Journal of Fluid Mechanics, **284**, pp. 257–274.

[54] Araki T., Kim M. S., Iwai H., and Suzuki K., 2002, "An Experimental Investigation of Gaseous Flow Characteristics in Microchannels," Microscale Thermophysical Engineering, **6**(2), pp. 117–130.

[55] Arkilic E. B., Schmidt M. A., and Breuer K. S., 1997, "Gaseous Slip Flow in Long Microchannels," Journal Of Microelectromechanical Systems, **6**(2), pp. 167–178.

[56] De A. K., 2008, "Numerical Modeling of Microscale Mixing using Lattice Boltzmann Method," Virginia Polytechnic Institute and State University.

[57] A.Wolf-Gladrow D., 2005, Lattice-Gas Cellular Automata and Lattice Boltzmann Models - An Introduction, Springer, New York.

[58] Chen S., and Doolen G. D., 1998, "Lattice Boltzmann Method for Fluid Flows," Annual Review of Fluid Mechanics, **30**(1), pp. 329–364.

[59] Ansumali S., Karlin I. V, Arcidiacono S., Abbas A., and Prasianakis N. I., 2007, "Hydrodynamics Beyond Navier-Stokes: Exact Solution to the Lattice Boltzmann Hierarchy," Physical Review Letters, **98**(12), p. 124502.

[60] Zhang Y. H., Gu X. J., Barber R. W., and Emerson D. R., 2007, "Modelling Thermal Flow in a Transition Regime using a Lattice Boltzmann Approach," Europhysics Letters, **77**(3), p. 30003.

[61] Shirani E., and Jafari S., 2007, "Application of LBM in Simulation of Flow in Simple Micro-Geometries and Micro Porous Media," Physical Review, pp. 34–42.

[62] Shibahara M., Inoue K., and Kobayashi K., 2008, "A Molecular Dynamics Study on Effects of Nanostructural Clearances at an Interface on Thermal Resistance," Proceedings of Micro/Nanoscale Heat Transfer International Conference MNHT2008-52276, pp. 1–7.

[63] Kharazmi A., and Kamali R., 2009, "Molecular Dynamic Simulation of Surface Roughness Effects on Nanoscale," Proceedings of the ASME 2009 7th

International Conference on Nanochannels, Microchannels and Minichannels ICNMM2009-82187, pp. 1–6.

[64] Schneider N. M., Srivastava R. R., and Kandlikar S. G., 2009, "Numerical Simulation of Single Phase Liquid Flow in Narrow Rectangular Channels with Structured Roughness Walls," Proceedings of the ASME 2009 7th International Conference on Nanochannels, Microchannels and Minichannels ICNMM2009-82255, pp. 1–7.

[65] Wu H., 2003, "An Experimental Study of Convective Heat Transfer in Silicon Microchannels with Different Surface Conditions," International Journal of Heat and Mass Transfer, **46**(14), pp. 2547–2556.

[66] Mahmood G. I., and Ligrani P. M., 2002, "Heat Transfer in a Dimpled Channel: Combined Influences of Aspect Ratio, Temperature Ratio, Reynolds Number, and Flow Structure," International Journal of Heat and Mass Transfer, **45**(10), pp. 2011–2020.

[67] Ligrani P. M., Mahmood G. I., Harrison J. L., Clayton C. M., and Nelson D. L., 2001, "Flow Structure and Local Nusselt Number Variations in a Channel with Dimples and Protrusions on Opposite Walls," International Journal of Heat and Mass Transfer, **44**(23), pp. 4413–4425.

[68] Naphon P., and Khonseur O., 2009, "Study on the Convective Heat Transfer and Pressure Drop in the Micro-Channel Heat Sink," International Communications in Heat and Mass Transfer, **36**(1), pp. 39–44.

[69] Tullius J. F., Vajtai R., and Bayazitoglu Y., 2011, "A Review of Cooling in Microchannels," Heat Transfer Engineering, **32**(7-8), pp. 527–541.

[70] Steinke M. E., and Kandlikar S. G., 2004, "Single-Phase Heat Transfer Enhancement Techniques in Microchannel and Minichannel Flows," ASME 2nd International Conference on Microchannels and Minichannels, pp. 141–148.

[71] Lee Y., Lee P., and Chou S., 2010, "Experimental Investigation of Silicon-Based Oblique Finned Microchannel Heat Sinks," Proceedings of the 14th International Heat Transfer Conference IHTC14-23413, pp. 1–9.

[72] John T. J., and Mathew B., 2009, "Characteristic Study on the Optimization of Pin-Fin Micro Heat Sink," Proceedings of the ASME 2009 International Mechanical Engineering Congress & Exposition IMECE2009-11816, pp. 1–8.

[73] John T. J., Mathew B., and Hegab H., 2010, "Parametric Study on the Combined Thermal and Hydraulic Performance of Single Phase Micro Pin-Fin Heat Sinks Part I: Square and Circle Geometries," International Journal of Thermal Sciences, **49**(11), pp. 2177–2190.

[74] Peles Y., Kosar A., Mishra C., Kuo C., and Schneider B., 2005, "Forced Convective Heat Transfer Across a Pin Fin Micro Heat Sink," International Journal of Heat and Mass Transfer, **48**(17), pp. 3615–3627.

[75] Selvarasu N. K. C., Tafti D. K., and Blackwell N. E., 2010, "Effect of Pin Density on Heat-Mass Transfer and Fluid Flow at Low Reynolds Numbers in Minichannels," Journal of Heat Transfer, **132**(6), p. 061702.

[76] Shafeie H., Abouali O., and Jafarpur K., 2010, "Numerical Investigation of Heat Transfer Enhancement in a Microchannel with Offset Micro Pin-Fins," Proceedings of the ASME FEDSM-ICNMM2010-30647, pp. 1–6.

[77] Koz M., Ozdemir M. R., and Koşar A., 2011, "Parametric Study on the Effect of End Walls on Heat Transfer and Fluid Flow Across a Micro Pin-Fin," International Journal of Thermal Sciences, **50**(6), pp. 1073–1084.

[78] Koz M., and Kosar A., 2010, "Parameter Optimization of a Micro Heat Sink with Circular Pin-Fins," Proceedings of the ASME 2010 3rd Joint US-European Fluids Engineering Summer Meeting and 8th International Conference on Nanochannels, Microchannels, and Minichannels, FEDSM-ICNMM2012-30473.

[79] Reyes M., Arias J. R., Velazquez A., and Vega J. M., 2011, "Experimental Study of Heat Transfer and Pressure Drop in Micro-Channel Based Heat Sinks with Tip Clearance," Applied Thermal Engineering, **31**(5), pp. 887–893.

[80] Min J. Y., Jang S. P., and Kim S. J., 2004, "Effect of Tip Clearance on the Cooling Performance of a Microchannel Heat Sink," International Journal of Heat and Mass Transfer, **47**(5), pp. 1099–1103.

[81] Prasher R. S., Dirner J., Chang J.-Y., Myers A., Chau D., He D., and Prstic S., 2007, "Nusselt Number and Friction Factor of Staggered Arrays of Low Aspect Ratio Micropin-Fins Under Cross Flow for Water as Fluid," Journal of Heat Transfer, **129**(2), p. 141.

[82] Qu W., and Siu-Ho A., 2008, "Liquid Single-Phase Flow in an Array of Micro-Pin-Fins—Part I: Heat Transfer Characteristics," Journal of Heat Transfer, **130**(12), p. 122402.

[83] Qu W., and Siu-Ho A., 2008, "Liquid Single-Phase Flow in an Array of Micro-Pin-Fins—Part II: Pressure Drop Characteristics," Journal of Heat Transfer, **130**(12), p. 124501.

[84] Siu-Ho A., Qu W., and Pfefferkorn F., 2007, "Experimental Study of Pressure Drop and Heat Transfer in a Single-Phase Micropin-Fin Heat Sink," Journal of Electronic Packaging, **129**(4), p. 479.

[85] Mita J. R., Qu W., Kobayashi M. H., and Pfefferkorn F. E., 2011, "Experimental Study and Numerical Analysis of Water Single-Phase Pressure Drop Across an Array of Circular Micro-Pin-Fins," Proceedings of the ASME/JSME 2011 8th Thermal Engineering Joint Confer March 13-17, 2011, Honolulu, Hawaii, USA

Proceedings of the ASME/JSME 2011 8 th Thermal Engineering Joint Conference AJTEC2011-44583, pp. 1–9.

[86] Koşar A., Mishra C., and Peles Y., 2005, "Laminar Flow Across a Bank of Low Aspect Ratio Micro Pin Fins," Journal of Fluids Engineering, **127**(3), p. 419.

[87] Koşar A., Schneider B., and Peles Y., 2011, "Hydrodynamic Characteristics of Crossflow over MEMS-Based Pillars," Journal of Fluids Engineering, **133**(8), p. 081201.

[88] Bayazitoglu Y., and Tullius J. F., 2009, "Nanocarpets Decorating the Walls of Microchannels," Proceedings of the ASME 2009 7th International Conference on Nanochannels, Microchannels and Minichannels ICNMM2009-82125, pp. 1–8.

[89] Jakaboski B. E., Joshi Y. K., and Rightley M., 2004, "Forced Convection in a Microchannel Heat Sink using Carbon Nanotubes for Heat Transfer Enhancement," Heat Transfer Engineering, **2**, pp. 227–233.

[90] Shenoy S., Tullius J. F., and Bayazitoglu Y., 2011, "Minichannels with Carbon Nanotube Structured Surfaces for Cooling Applications," International Journal of Heat and Mass Transfer, **54**(25-26), pp. 5379–5385.

[91] Tullius J. F., Tullius T. K., and Bayazitoglu Y., 2011, "Optimization of Microstructured Fins in Minichannels," Proceedings of the ASME 2012

Thermal and Materials Nanoscience and Nanotechnology, Antalya, Turkey, TMNN 2011-068.

[92] Tullius J. F., Tullius T. K., and Bayazitoglu Y., 2012, "Optimization of Short Micro Pin Fins in Minichannels," International Journal of Heat and Mass Transfer, **55**(15-16), pp. 3921–3932.

[93] Zukauskas A., 1972, "Heat Transfer from Tubes in Crossflow," Advances in Heat Transfer, **8**, pp. 93–160.

[94] Hwang T. H., and Yao S. C., 1986, "Crossflow Heat Transfer in Tube Bundles at Low Reynolds Numbers," Journal of Heat Transfer, **108**(3), pp. 697–700.

[95] Khan W. A., Culham J. R., and Yovanovich M. M., 2001, "Optimization of Pin-Fin Heat Sinks using Entropy Generation Minimization," IEEE Transactions on Components and Packaging Technologies, **24**(2), pp. 159–165.

[96] Kosar A., and Peles Y., 2006, "Convective Flow of Refrigerant (R-123) Across a Bank of Micro Pin Fins," International Journal of Heat and Mass Transfer, **49**, pp. 3142–3155.

[97] Metzger D. E., Shepard W. B., and Haley S. W., 1986, "Row Resolved Heat Transfer Variations in Pin-Fin Arrays Including Effects of Non-Uniform Arrays and Flow Convergence," Proceedings of ASME International Gas Turbine Conference and Exhibit.

[98] Moores K. a., and Joshi Y. K., 2003, "Effect of Tip Clearance on the Thermal and Hydrodynamic Performance of a Shrouded Pin Fin Array," Journal of Heat Transfer, **125**(6), p. 999.

[99] Short B. E., Raad P. E., and Price D. C., 2002, "Performance of Pin Fin Cast Aluminum Coldwalls, Part II: Colburn j-Factor Correlations," Journal of Thermo-physics Heat Transfer, **16**(3), pp. 397–403.

[100] Whitaker S., 1972, "Forced Convection Heat Transfer Correlations for Flow in Pipes, Past Flat Plates, Single Cylinders, Single Spheres, and for Flow in Packed Beds and Tube Bundles," AIChE Journal, **18**(2), pp. 361–371.

[101] Liu M., Liu D., Xu S., and Chen Y., 2011, "Experimental Study on Liquid Flow and Heat Transfer in Micro Square Pin Fin Heat Sink," International Journal of Heat and Mass Transfer, **54**(25-26), pp. 5602–5611.

[102] Siu-Ho A. M., Qu W., and Pfefferkorn F., 2007, "Hydrodynamic and Thermal Characteristics of Single-Phase and Two-Phase Micro-Pin-Fin Heat Sinks," Proceedings of ASME International Mechanical Engineering Congress and Exposition Conference, **IMECE2007**.

[103] Short B. E., Raad P. E., and Price D. C., 2002, "Performance of Pin Fin Cast Aluminum Coldwalls, Part I: Friction Factor Correlations," Journal of Thermo-phys. Heat Transfer, **16**(3), pp. 389–396.

[104] Armstrong J., and Winstanley D., 1988, "A Review of Staggered Array Pin Fin Heat Transfer for Turbine Cooling Applications," J. Turbomach, **110**, pp. 94–103.

[105] Chilton T. H., and Generaux R. P., 1933, "Pressure Drop Across Tube Banks," Trans. Am. Inst. Chem. Eng., **29**, pp. 161–173.

[106] Gaddis E. S., and Gnielski V., 1985, "Pressure Drop in Horizontal Cross Flow Across Tube Bundles," Int. Chem. Eng., **29**, pp. 161–173.

[107] Gunther A. Y., and Shaw W. A., 1945, "A General Correlation of Friction Factors for Various Types of Surfaces in Cross Flow," ASME Mech Eng., **67**, pp. 643–660.

[108] Kast W., 1974, "Druckverlust bei der Stromung quer zu Rohrbundeln (Pressure Drop in Cross Flow across Tube Bundles)," VDI-Warmeatlas, **Section Ld**.

[109] Moores K. A., Kim J., and Joshi Y. K., 2009, "Heat Transfer and Fluid Flow in Shrouded Pin Fin Arrays with and without Tip Clearance," International Journal of Heat and Mass Transfer, **52**(25-26), pp. 5978–5989.

[110] Konishi C. A., Qu W., and Pfefferkorn F. E., 2009, "Experimental Study of Water Liquid-Vapor Two-Phase Pressure Drop Across an Array of Staggered Micropin-Fins," Journal of Electronic Packaging, **131**(2).

[111] Konishi C. A., Hwu R., Qu W., and Pfefferkorn F. E., 2010, "Experimental Study and Numerical Analysis of Water Single-Phase," Proceedings of the 14th International Heat Transfer Conference IHTC14-23171, pp. 1–9.

[112] Gunnasegaran P., Mohammed H. a., Shuaib N. H., and Saidur R., 2010, "The Effect of Geometrical Parameters on Heat Transfer Characteristics of Microchannels Heat Sink with Different Shapes," International Communications in Heat and Mass Transfer, **37**(8), pp. 1078–1086.

[113] Mohammed H. a., Gunnasegaran P., and Shuaib N. H., 2011, "Influence of Channel Shape on the Thermal and Hydraulic Performance of Microchannel Heat Sink," International Communications in Heat and Mass Transfer, **38**(4), pp. 474–480.

[114] Mohammed H. a., Gunnasegaran P., and Shuaib N. H., 2011, "Numerical Simulation of Heat Transfer Enhancement in Wavy Microchannel Heat Sink," International Communications in Heat and Mass Transfer, **38**(1), pp. 63–68.

[115] Singh N., Sathyamurthy V., Peterson W., Arendt J., and Banerjee D., 2010, "Flow Boiling Enhancement on a Horizontal Heater using Carbon Nanotube Coatings," International Journal of Heat and Fluid Flow, **31**(2), pp. 201–207.

[116] Khanikar V., Mudawar I., and Fisher T. S., 2009, "Flow Boiling in a Micro-Channel Coated with Carbon Nanotubes," Transactions on Components and Packaging Technologies, **32**(3), pp. 639–649.

[117] Khanikar V., Mudawar I., and Fisher T., 2009, "Effects of Carbon Nanotube Coating on Flow Boiling in a Micro-Channel," International Journal of Heat and Mass Transfer, **52**, pp. 3805–3817.

[118] Chen T., and Garimella S. V., 2011, "Local Heat Transfer Distribution and Effect of Instabilities During Flow Boiling in a Silicon Microchannel Heat Sink," International Journal of Heat and Mass Transfer, **54**(15-16), pp. 3179–3190.

[119] Yuan M., Wei J., Xue Y., and Fang J., 2009, "Subcooled Flow Boiling Heat Transfer of FC-72 from Silicon Chips Fabricated with Micro-Pin-Fins," International Journal of Thermal Sciences, **48**(7), pp. 1416–1422.

[120] Yang K. S., Jeng Y. R., Huang C. M., and Wang C. C., 2011, "Heat Transfer and Flow Pattern Characteristics for HFE-7100 within Microchannel Heat Sinks," Heat Transfer Engineering, **32**(7-8), pp. 697–704.

[121] Ahn H. S., and Kim M. H., 2012, "A Review on Critical Heat Flux Enhancement with Nanofluids and Surface Modification," Journal of Heat Transfer, **134**(2), p. 024001.

[122] Hung T.-C., Yan W.-M., Wang X.-D., and Chang C.-Y., 2012, "Heat Transfer Enhancement in Microchannel Heat Sinks using Nanofluids," International Journal of Heat and Mass Transfer, **55**, pp. 2559–2570.

[123] Pil Jang S., and Choi S. U. S., 2007, "Effects of Various Parameters on Nanofluid Thermal Conductivity," Journal of Heat Transfer, **129**(5), pp. 617–623.

[124] Heris S. Z., Esfahany M. N., and Etemad S. G., 2007, "Experimental Investigation of Convective Heat Transfer of Al2O3/Water Nanofluid in Circular Tube," International Journal of Heat and Fluid Flow, **28**(2), pp. 203–210.

[125] Vaziee P., and Abouali O., 2008, "Numerical Study of Forced Convection of Nanofluid in a Microchannel," Proceedings of the Sixth International ASME Conference on Nanochannels, Microchannels and Minichannels ICNMM2008-62306, pp. 1–7.

[126] Nguyen C., Desgranges F., Galanis N., Roy G., Mare T., Boucher S., and Anguemintsa H., 2008, "Viscosity Data for Al2O3–Water Nanofluid—Hysteresis: Is Heat Transfer Enhancement using Nanofluids Reliable?," International Journal of Thermal Sciences, **47**(2), pp. 103–111.

[127] Nguyen C., Desgranges F., Roy G., Galanis N., Mare T., Boucher S., and Anguemintsa H., 2007, "Temperature and Particle-Size Dependent Viscosity Data for Water-Based Nanofluids – Hysteresis Phenomenon," International Journal of Heat and Fluid Flow, **28**(6), pp. 1492–1506.

[128] Zhu D. S., Wu S. Y., and Wang N., 2010, "Surface Tension and Viscosity of Aluminum Oxide Nanofluids," Proceedings of American Institute of Physics, **1207**(1), p. 460.

[129] Sridhara V., and Satapathy L. N., 2011, "Al2O3-Based Nanofluids: A Review.," Nanoscale research letters, **6**(1), p. 456.

[130] Golubovic M. N., Madhawa Hettiarachchi H. D., Worek W. M., and Minkowycz W. J., 2009, "Nanofluids and Critical Heat Flux, Experimental and Analytical Study," Applied Thermal Engineering, **29**(7), pp. 1281–1288.

[131] Sajith V., Madhusoodanan M. R., and Sobhan C. B., 2008, "An Experimental Investigation of the Boiling Performance of Water-Based Nanofluids," MNHT2008-52216, pp. 1–7.

[132] Fattahi E., Farhadi M., Sedighi K., and Nemati H., 2012, "Lattice Boltzmann Simulation of Natural Convection Heat Transfer in Nanofluids," International Journal of Thermal Sciences, **52**, pp. 137–144.

[133] Haddad Z., Abu-Nada E., Oztop H. F., and Mataoui A., 2012, "Natural Convection in Nanofluids: Are the Thermophoresis and Brownian Motion Effects Significant in Nanofluid Heat Transfer Enhancement?," International Journal of Thermal Sciences, **57**, pp. 152–162.

[134] Suresh S., Venkitaraj K. P., Selvakumar P., and Chandrasekar M., 2012, "A Comparison of Thermal Characteristics of Al2O3/Water and CuO/Water Nanofluids in Transition Flow through a Straight Circular Duct Fitted with Helical Screw Tape Inserts," Experimental Thermal and Fluid Science, **39**, pp. 37–44.

[135] Mohammeda H. A., Bhaskarana G., Shuaiba N. H., and Saidur R., 2011, "Heat Transfer and Fluid Flow Characteristics in Microchannels Heat Exchanger using Nanofluids: A Review," Renewable and Sustainable Energy Reviews, **15**, pp. 1502–1512.

[136] Zhou M., Xia G., Chai L., Li J., and Zhou L., 2012, "Analysis of Flow and Heat Transfer Characteristics of Micro-Pin Fin Heat Sink using Silver Nanofluids," Science China Technological Sciences, **55**(1), pp. 155–162.

[137] Tullius J. F., and Bayazitoglu Y., 2012, "Minichannels Cooling using MWNT Fin Structures and Al2O3 Nanofluid," Proceedings of the ASME 2012 International Mechanical Engineering Congress & Exposition, Houston, TX, IMECE2012-89925, pp. 1–2.

[138] Tullius J. F., and Bayazitoglu Y., 2013, "Effect of Al2O3/H2O Nanofluid on MWNT Circular Fin Structures in a Minichannel," International Journal of Heat and Mass Transfer, **60**, pp. 523–530.

[139] Kline S. J., and McClintock F. A., 1953, "Describing Uncertainties in Single-Sample Experiments," Mechanical Engineering, **75**(1), pp. 3–8.

[140] Mohammed H. A., Gunnasegaran P., and Shuaib N. H., 2010, "Heat Transfer in Rectangular Microchannels Heat Sink Using Nanofluids," International Communications in Heat and Mass Transfer, **37**(10), pp. 1496–1503.

[141] Maxwell J. C., 1954, A Treatise on Electricity and Magnetism, Oxford: Clarendon Press, New York.

[142] Chai Z., Guo Z., Zheng L., and Shi B., 2008, "Lattice Boltzmann Simulation of Surface Roughness Effect on Gaseous Flow in a Microchannel," Journal of Applied Physics, **104**(1).

[143] Zhang R., Di Q., Wang X., and Gu C., 2010, "Numerical Study of Wall Wettabilities and Topography on Drag Reduction Effect in Micro-channel Flow by Lattice Boltzmann Method," Journal of Hydrodynamics, Ser. B, **22**(3), pp. 366–372.

[144] Zhou P., Guo D., Kang R., and Jin Z., 2012, "Analysis of Laminar Flow Over a Non-Conventional Random Rough Surface Based on Lattice Boltzmann Method," Journal of Tribology, **134**(1), pp. 12201–12207.

[145] Liu Y., Cui J., Jiang Y. X., and Li W. Z., 2011, "A Numerical Study on Heat Transfer Performance of Microchannels with Different Surface Microstructures," Applied Thermal Engineering, **31**(5), pp. 921–931.

[146] Zhang C., Chen Y., Deng Z., and Shi M., 2012, "Role of rough surface topography on gas slip flow in microchannels," Physical Review E, **86**(1), p. 16319.

[147] Ding L., Shi W., and Luo H., 2011, "Numerical Simulation of Viscous Flow Over Non-Smooth Surfaces," Computers & Mathematics with Applications, **61**(12), pp. 3703–3710.

[148] Ladd A. J. C., and Verberg R., 2001, "Lattice-Boltzmann Simulations of Particle-Fluid Suspensions," Journal of Statistical Physics, **104**(September), pp. 1191–1251.

[149] Xuan Y., and Yao Z., 2004, "Lattice Boltzmann model for nanofluids," Heat and Mass Transfer, **41**(3), pp. 199–205.

[150] Joshi A. S., and Sun Y., 2009, "Multiphase Lattice Boltzmann Method for Particle Suspensions," Physical Review E - Statistical, Nonlinear and Soft Matter Physics, **79**.

[151] Derksen J. J., 2007, "The Lattice-Boltzmann Method for Multiphase Fluid Flow Simulations and Euler-Lagrange Large-Eddy Simulations," Evolution.

[152] Guo Y., Qin D., Shen S., and Bennacer R., 2012, "Nanofluid Multi-Phase Convective Heat Transfer in Closed Domain: Simulation with Lattice Boltzmann Method," International Communications in Heat and Mass Transfer, **39**(3), pp. 350–354.

[153] Ding E.-J., and Aidun C. K., 2003, "Extension of the Lattice-Boltzmann Method for Direct Simulation of Suspended Particles Near Contact," Journal of Statistical Physics, **112**(314), pp. 685–708.

[154] Kosinski P., Kosinska A., and Hoffmann A. C., 2009, "Simulation of Solid Particles Behaviour in a Driven Cavity Flow," Powder Technology, **191**(3), pp. 327–339.

[155] Bhatnagar P. L., Gross E. P., and Krook M., 1954, "A Model for Collision Processes in Gases. I. Small Amplitude Processes in Charged and Neutral One-Component Systems," Physical Review, **94**(3), pp. 511–525.

[156] Sterling J. D., and Chen S., 1996, "Stability Analysis of Lattice Boltzmann Methods," Journal of Computational Physics, **123**, pp. 196–206.

[157] Daniel Heubes, 2010, "Lattice Boltzmann Method in Theory and in Application to Coupled Problems."

[158] Huang H., Krafczyk M., and Lu X., 2011, "Forcing Term in Single-Phase and Shan-Chen-Type Multiphase Lattice Boltzmann Models," Physical Review E, **84**(4), p. 046710.

[159] Zou Q., and He X., 1997, "On Pressure and Velocity Flow Boundary Conditions and Bounceback for the Lattice Boltzmann BGK Model," Physics of Fluids, **9**(6), pp. 1591–1598.

[160] Ziegler D. P., 1993, "Boundary Conditions for Lattice Boltzmann Simulations," Journal of Statistical Physics, **71**(5-6), pp. 1171–1177.

[161] Bayazitoglu Y., and Ozisik N., 2012, A Textbook for Heat Transfer Fundamentals, Begell House, Inc., New York.